

# **Synthesis and Characterization of Biocompatible Inorganic/Organic Nanocomposites Material for Sensor Applications**

**THESIS**

**Submitted to the Delhi Technological University**

**For the award of the degree of**

**DOCTOR OF PHILOSOPHY**

*By*

**SUJEET KUMAR MISHRA**



**Department of Applied Chemistry and Polymer Technology,  
Delhi Technological University,  
Bawana Road, Delhi-110042**

**JULY 2014**

# **Synthesis and Characterization of Biocompatible Inorganic/Organic Nanocomposites Material for Sensor Applications**

by

**SUJEET KUMAR MISHRA**

Department of Applied Chemistry and Polymer Technology

Submitted  
in fulfilment of the requirements of the degree of Doctor of Philosophy  
to the



**Delhi Technological University,  
Bawana Road, Delhi-110042**

**JULY 2014**

## **CERTIFICATE**

This is to certify that the thesis titled “**Synthesis and Characterization of Biocompatible Inorganic/Organic Nanocomposites Material for Sensor Applications**” submitted to the Delhi Technological University, Delhi, in fulfilment of the requirements for the award of the degree of Doctor of Philosophy embodies the original research work carried out by Mr. Sujeet Kumar Mishra under our supervision. This work has not been submitted in part or full for any degree or diploma of this or any other University.

**Prof. D Kumar**  
(Supervisor)  
Head of the Department,  
Applied Chemistry & Polymer Technology,  
Delhi Technological University,  
Bawana Road,  
New Delhi-110042

**Dr. Rajesh**  
(Co-Supervisor)  
Principal Scientist,  
Polymer and Soft Materials Section,  
CSIR-National Physical Laboratory,  
Dr. K.S. Krishnan Marg,  
New Delhi-110012

***DEDICATED TO  
MY PARENTS & MENTORS***

---



## Acknowledgements

I wish to express profound sense of gratitude to my honored supervisors Prof. D. Kumar, Head, Department of Applied Chemistry, Delhi Technological University, New Delhi and Dr. Rajesh, Principal Scientist, CSIR-National Physical Laboratory, New Delhi for their constant inspiration to me at every stage of my research. Without their serious involvement, thoughtfulness and patience, it would have been difficult for me to complete this thesis in time. It was an invaluable experience to work with them and to learn so many things from them. It has been a great pleasure and I really cherished working with them. They made me realize that apart from knowing my subject and hard work I need passion and imagination to invent and discover.

I must express my earnest gratitude to Dr. A.M. Biradar, Head, Material Physics and Engineering, CSIR-National Physical Laboratory for his interest and encouragement at various stages of the work.

I am deeply indebted to Professor P.B. Sharma, Vice Chancellor, Delhi Technological University and Prof. R. C. Budhani, Director, CSIR-National Physical Laboratory, New Delhi, for providing necessary facilities.

I am very much grateful to the Council of Scientific and Industrial Research, New Delhi for providing me financial assistance in the form of junior and senior research fellowship to carry out my PhD work.

I thank Dr. Avanish K. Srivastava for his invaluable help in the HRTEM characterization of many samples and Dr. Nahar Singh for his valuable and timely help throughout my research work.

I would like to thank all Laboratory and Office Staff members and colleagues of DTU and NPL for their support and cooperation. I thank my senior Dr. Tarushee Ahuja and my colleagues Ms. Nidhi Puri, Ms. Shobita Singhal, Ms. Sudha, Ms. Ritu, Ms. Sarita Nair, Mr. Tilak Joshi and Mr. Achu Chandran for many valuable conversations on academic and nonacademic matters. I also thank Mr. Vinod Tanwar, Mr. Vikash Sharma and Mr. Mange Ram for their friendly support.

Many thanks are due to my parents and my brothers for their love, support and unabated faith in me, which kept me going through this work.

Finally, I am thankful to God for His blessings without which this endeavor was never possible.

**(Sujeet K. Mishra)**

## *Abstract*

---

According to WHO report 2011, cardiovascular diseases (CVD) have been considered as the leading cause of death around the world which includes coronary heart disease, cerebrovascular disease, raised blood pressure, peripheral artery disease, rheumatic heart disease, congenital heart disease and heart failure. The symptoms typically associated with heart attacks and angina includes chest pain, pressure, shortness of breath, and/or nausea but they may also be seen with non-heart related conditions. Since the treatment for each previous condition differs, and most of them require urgent measures, it is necessary that physicians are provided with additional information in a short time basis, enabling them to carry out quick and accurate diagnosis. So far for diagnosis, prognosis, monitoring, and risk stratification of suspected heart attack patients with symptoms of acute myocardial infarction (AMI), cardiac biomarkers have been employed. Different laboratorial detection methods are used for the estimation of cardiac biomarkers that include sandwich immunoassay with secondary labeled antibodies, enzyme linked immunosorbent assay (ELISA) and fluorescence. However, they require laboratory equipments with proper instrument, multi-step processing of samples, and well-trained personnel, leading to considerable time consuming and expense to the overall detection. Therefore, there is a growing demand for a range of rapid and low cost device for the detection of CVD.

Biosensors can play an important role in this regard, without having to rely on hospital visits, where expensive and time consuming laboratory tests are recommended.

Among the different types of biosensors available, the biosensors based on electrochemical impedance spectroscopy (EIS) have emerged as the most commonly used biosensors as they have been found to overcome most of the disadvantages, which inhibits the use of other types of biosensors. EIS is a powerful method to analyze the complex electrical resistance of a system and is sensitive to surface phenomena and changes of bulk properties. Thus, in the field of biosensing, it is particularly suited for the detection of binding events and is sensitive to changes in interfacial impedance upon bio-recognition events occurring at the electrode/electrolyte interface.

The basic characteristics of electrochemical biosensors are associated with their capability to detect a specific biomolecule with high specificity and sensitivity. Also, these characteristics are dictated by a better correlation between the biological component and the transducing element. Important advances in these aspects have been achieved with the utilization of several kinds of nanomaterials to improve electrochemical signal of bio-recognition events occurring at the electrode/electrolyte interface.

The present thesis is an attempt towards the synthesis and characterization of biocompatible nanoparticles, i.e., ZnS/Pt and their nanocomposites with organic conducting polymer and inorganic graphene/silane materials for bio-sensing applications, especially for the quantitative detection of cardiac biomarkers e.g. myoglobin and C-reactive protein. The main objective behind the utilization of these nanomaterials is to combine the high power of detection with preservation of the structural integrity of the biomolecules, for the development of biosensors with improved properties such as



sensitivity and limit of detection. The chapter wise brief description of the thesis work is herein given below:

**Chapter 1, Part I** of the thesis highlights some of the basic general information and features of the biosensor, the role of various nanomaterials in biosensing and a brief introduction about the cardiac biomarkers. In the subsequent **Part II** of the **chapter 1**, the theory and applications of various characterization techniques such as X-ray Diffraction (XRD), Fourier Transform Infrared (FTIR) Spectroscopy, Scanning Electron Microscopy (SEM), Transmission Electron Microscopy (TEM), Atomic Force Microscopy (AFM), Cyclic Voltammetry and EIS which has been used in the present work have been discussed. In brief, motivation behind the present work has been highlighted in this chapter.

**Chapter 2** describes a facile in-situ electrochemical synthesis of mercaptopropionic acid functionalized zinc sulfide nanoparticles, ZnS(MPA), intercalated conducting polypyrrole (PPy) nanocomposite film, deposited over an indium-tin-oxide coated glass plate (ITO-glass). The cardiac protein antibody, C-reactive protein, (Ab- $\alpha$ CRP), has been covalently immobilized on the ZnS(MPA)-PPy nanocomposite film using carbodiimide coupling reaction. The chapter demonstrates the utility of combining the two types of advanced materials with complementary properties, organic conducting polymers (PPy) and inorganic nanoparticles (ZnS), to construct a bioelectrode. The nanocomposite film was characterized by TEM, AFM and electrochemical techniques. The chapter also delineates the effect of the film thickness

on electrical and sensing properties of the polymer nanocomposite film towards the detection and quantification of the protein antigen (Ag- $\alpha$ CRP).

In **Chapter 3**, the conducting metal Pt nanoparticles has been used to prepare a Pt(MPA)-PPy nanocomposite film based bioelectrode for the quantitative detection of  $\alpha$ CRP. This has been done to analyze the effect of the synergistic behavior of metal nanoparticles (Pt) and electrically conducting polymers (PPy) over the sensitivity of the bioelectrode. The microstructural characteristics of the Pt(MPA)-PPy nanocomposite film were studied using XRD, FTIR, TEM and AFM techniques. The interfacial surface electron transport study of the bioelectrode towards protein antigen, Ag- $\alpha$ CRP, was carried out by EIS. The rationale behind using the 3-dimensional metal Pt(MPA) nanoparticles is that these nanoparticles not only helps in preserving the native protein conformation and reducing the steric hindrance for better probe orientation and accessibility of the biomolecules to the analytes but also facilitated the improved charge shuttling throughout the material.

In **chapters 4 and 5**, self assembled monolayer (SAM) of 3-aminopropyl triethoxysilane (APTES) was used to covalently attach the different nanoparticles, i.e., ZnS or Pt for the fabrication of the bioelectrodes. APTES forms a SAM of molecular thickness through the self organization of molecules in an ordered manner on ITO-glass surface. The stability, uniform surface structure and relative ease of formation makes the SAM more suitable for bio-sensing applications.

**Chapter 4** contains the details of the fabrication and characterization of ZnS(MPA)NPs-APTES based bioelectrode for the impedimetric detection of cardiac

protein myoglobin (cMb). This bioelectrode was characterized using AFM, contact angle measurements, cyclic voltammetry and EIS. The values of EIS experimental data so obtained revealed that the charge transfer resistance ( $R_{ct}$ ) increases considerably with no significant change in double layer capacitance ( $C_{dl}$ ) after immunoreaction with protein antigen myoglobin, Ag-cMb, in the low frequency region.

**Chapter 5** deals with a covalent biomolecular immobilization of 3-dimensional carboxyl functionalized Pt nanoparticles, Pt(MPA), covalently attached over a silane modified ITO-glass plate via carbodiimide coupling reaction, acting as a bioelectrode for the quantitative detection of cMb. Both the microstructural and electrochemical characteristics of the bioelectrode were extensively characterized by AFM, TEM, XRD, Energy-dispersive X-ray spectroscopy (EDX), and EIS techniques. The work demonstrates a detail EIS characteristic of a bioelectrode based on functionalized Pt-NPs for the investigation of bioaffinity interaction towards the detection of prognostic cardiac marker, cMb.

**Chapter 6** deals with the bio-functionalization of ZnS nanoparticles anchored over the electrochemically reduced graphene oxide sheets through a cross linker, 1-pyrenemethylamine hydrochloride, by carbodiimide reaction, for the construction of a bioelectrode. The bioelectrode was characterized by SEM, HRTEM, EDX and EIS spectroscopy. A detail electrochemical immunosensing studies has been carried out on the bioelectrode towards the detection of target Ag-cMb. The optimal fitted equivalent circuit model that matches the impedance response has been studied to delineate the biocompatibility, sensitivity and selectivity of the bioelectrode. The impedimetric

sensing performance of the bioelectrode with ZnS-RGO nanocomposite has been compared with that of native RGO sheets without ZnS nanoparticles, to highlight the contribution of the ZnS nanoparticles in the overall enhanced immunosensing performance.

Finally, **Chapter 7** contains the concluding remarks or inferences drawn from the entire research work presented in this thesis and its future prospective. It discusses the insights that have been gathered during the course of the thesis work.

# CONTENTS

---

<b>Acknowledgements</b>	i
<b>Abstract</b>	iii
<b>List of figures</b>	xiii
<b>List of tables</b>	xix
<b>1 Part I: An Overview and General Introduction</b>	
1.1 Biosensors	1
1.2 Basic concept of biosensor	2
1.3 Classification of biosensors	5
1.3.1 Classification based on biorecognition element	5
1.3.2 Classification based on the transduction method	8
1.4 Role of nanomaterials and nanocomposites in biosensors	13
1.4.1 Biocompatible Nanomaterials and Nanocomposites	14
1.5 Cardiac Biomarkers	21
1.5.1 Cardiovascular disease	21
1.5.2 Cardiac biomarkers and their application	22
<b>Part II: Characterization Techniques</b>	
1.6 X-ray Diffraction	29
1.7 Fourier Transform Infrared Spectroscopy	32
1.8 Scanning Electron Microscopy	37
1.9 Transmission Electron Microscopy	39
1.10 Atomic Force Microscopy	43
1.11 Cyclic Voltammetry	45
1.12 Electrochemical impedance spectroscopy	48
1.13 References	52
<b>2 Protein functionalized ZnS(MPA)-PPy nanocomposite film based bioelectrode</b>	
2.1 Introduction	63
2.2 Experimental	67
2.2.1 Reagents	67

2.2.2	Equipments	68
2.2.3	Synthesis of ZnS(MPA) nanoparticles	68
2.2.4	Preparation of the bioelectrode	69
2.3	Results & Discussion	70
2.3.1	Microstructural Characterization	70
2.3.2	Electrochemical characterization of the bioelectrode	74
2.3.3	Electrochemical impedance response to protein antigen	79
2.4	Conclusion	82
2.5	References	83
<b>3</b>	<b>Protein functionalized Pt(MPA)-PPy nanocomposite film based bioelectrode</b>	
3.1	Introduction	86
3.2	Experimental	88
3.2.1	Reagents	88
3.2.2	Equipments	89
3.2.3	Preparation of bioelectrode	89
3.3	Results and Discussion	91
3.3.1	Micro structural characterization	91
3.3.2	Electrochemical characterization of the bioelectrode	96
3.3.3	Electrochemical impedance response to protein antigen	102
3.4	Conclusions	108
3.5	References	110
<b>4</b>	<b>Protein functionalized ZnS nanoparticles-Silane composite based bioelectrode</b>	
4.1	Introduction	114
4.2	Experimental	116
4.2.1	Reagents	116
4.2.2	Equipments	116
4.2.3	Microstructural characterization of ZnS(MPA) nanoparticles	117
4.2.4	Preparation of bioelectrode	118

4.3	Results and Discussion	119
4.3.1	Contact angle measurement	119
4.3.2	Microstructural characterization	121
4.3.3	Electrochemical characterization of the bioelectrode	122
4.3.4	Surface coverage and nature of the bioelectrode	127
4.3.4	Electrochemical impedance response to protein antigen	128
4.4	Conclusions	132
4.5	References	134
<b>5</b>	<b>Protein functionalized Pt nanoparticles-Silane composite based bioelectrode</b>	
5.1	Introduction	137
5.2	Experimental	138
5.2.1	Reagents	138
5.2.2	Equipments	139
5.2.3	Synthesis of functionalized Pt nanoparticles	139
5.2.4	Preparation of bioelectrode	140
5.3	Results and Discussion	142
5.3.1	Contact angle measurement	142
5.3.2	Microstructural characterization	143
5.3.3	Electrochemical characterization of the bioelectrode	149
5.3.4	Surface coverage and the nature of the bioelectrode	152
5.3.5	Electrochemical impedance response to protein antigen	154
5.4	Conclusions	159
5.5	References	161
<b>6</b>	<b>Protein functionalized ZnS nanoparticles-Reduced graphene oxide based bioelectrode</b>	
6.1	Introduction	164
6.2	Experimental	167
6.2.1	Reagents	167
6.2.2	Equipments	167

6.2.3	Fabrication of the bioelectrode	167
6.3	Results and Discussions	170
6.3.1	Contact angle measurement	170
6.3.2	Microstructural characterization	172
6.3.3	Electrochemical characterization of bioelectrode	176
6.3.4	Electrochemical impedance response to protein antigen	183
6.4	Conclusion	189
6.5	References	190
<b>7</b>	<b>CONCLUSIONS AND FUTURE PERSPECTIVE</b>	<b>193</b>
	<b>List of Publications</b>	<b>199</b>



## LIST OF FIGURES

---

- Fig. 1.1:** Schematic representation of a biosensor
- Fig. 1.2:** Mechanism of electrochemical polymerization of Polypyrrole
- Fig. 1.3:** Ribbon structure of Myoglobin
- Fig. 1.4:** Ribbon structure of Troponin
- Fig. 1.5:** Ribbon Structure of Human C-reactive protein
- Fig. 1.6:** (a) A schematic layout of XRD (b) X-ray Powder Diffractometer
- Fig. 1.7:** A graphical representation of the electromagnetic spectrum
- Fig. 1.8:** Absorption bands corresponding to various regions of IR
- Fig. 1.9:** A simple layout of an FTIR instrument
- Fig. 1.10:** A schematic layout of SEM
- Fig. 1.11:** A schematic layout of TEM
- Fig. 1.12:** Block diagram of AFM
- Fig. 1.13:** (a) A cyclic voltammetry potential waveform with switching potentials  
(b) A typical cyclic voltammogram showing reduction and oxidation peak
- Fig. 1.14:** Randles equivalent circuit
- Fig. 1.15:** (a) Nyquist plot; (b) Bode plot
- Fig. 2.1:** Current analytical techniques used to quantify CRP samples
- Fig. 2.2:** Scheme showing the stepwise fabrication of the immunosensor
- Fig. 2.3:** AFM images of (a) PPy/ITO-glass, (b) ZnS(MPA)-PPy/ITO-glass and  
(c) Ab- $\alpha$ CRP/ZnS(MPA)-PPy/ITO-glass.

- Fig. 2.4:** XRD pattern of (a) ZnS(MPA), (b) pure PPy and (c) ZnS(MPA)-PPy; Inset: TEM image of ZnS(MPA)-PPy film electrochemically grown on a copper grid.
- Fig. 2.5:** FTIR spectra of PPy film and ZnS(MPA)-PPy nanocomposite film.
- Fig. 2.6:** Cyclic voltammograms of: PPy/ITO-glass; ZnS(MPA)-PPy/ITO-glass and Ab- $\alpha$ CRP/ZnS(MPA)-PPy/ITO-glass in PBS (pH 7.4) with 0.1 M KCl solution containing 2 mM  $[\text{Fe}(\text{CN})_6]^{3-}/[\text{Fe}(\text{CN})_6]^{4-}$ ; scan rate 50 mV/s.
- Fig. 2.7:** Nyquist diagrams for PPy/ITO-glass, ZnS(MPA)-PPy/ITO-glass and Ab- $\alpha$ CRP/ZnS(MPA)-PPy/ITO-glass bioelectrodes with different film thickness prepared at 250 and 1000  $\text{mC cm}^{-2}$  injected charge densities; inset: Bode plots of the corresponding bioelectrodes
- Fig. 2.8:** Nyquist plot of the bioelectrode prepared at 250  $\text{mC cm}^{-2}$  injected charge density before and after incubating with different concentrations of Ag- $\alpha$ CRP in PBS (pH 7.4) with 0.1 M KCl solution containing 2mM  $[\text{Fe}(\text{CN})_6]^{3-/4-}$  inset: Bode plots of the corresponding immunoreaction
- Fig. 2.9:** Concentration dependent calibration curve of the bioelectrodes; the error bars represent the standard deviation from three separate experiments
- Fig. 3.1:** Schematic representation of the stepwise fabrication of the bioelectrode
- Fig. 3.2:** XRD Pattern of pristine PPy and Pt(MPA)NPs-PPy composite
- Fig. 3.3:** FTIR spectra of PPy and Pt(MPA)-PPy showing additional peaks and shift in peak positions
- Fig. 3.4:** HRTEM image of (a) distribution of nanoparticles and (b) Gaussian size-distribution curve of the nanoparticles

- Fig. 3.5:** HRTEM image showing (a) distribution of Pt- nanoparticles in a PPy-matrix, and (b) atomic scale images of Pt-nanoparticles in the PPy matrix; Inset: SAEDP of nanocomposite
- Fig. 3.6:** AFM images of (a) PPy/ITO-glass, (b) Pt(MPA)NPs-PPy/ITO-glass and (c) Ab- $\alpha$ CRP/Pt(MPA)NPs-PPy/ITO-glass plate
- Fig. 3.7:** (a) Nyquist plots obtained for pristine PPy-ITO glass, Pt(MPA)NPs-PPy/ITO-glass, Pt-PPy/ITO-glass and Ab- $\alpha$ CRP/Pt(MPA)NPs-PPy/ITO-glass in PBS (pH 7.4, 0.1M KCl) containing 2mM  $[\text{Fe}(\text{CN})_6]^{3-/4-}$  and (b) Corresponding bode plots
- Fig. 3.8:** CV of bioelectrode as a function of scan rate in PBS (pH 7.4, 0.1M KCl) containing 2mM  $[\text{Fe}(\text{CN})_6]^{3-/4-}$ . Inset: plot of redox peak current vs  $v^{1/2}$
- Fig. 3.9:** (a) Faradaic impedance spectra of the Ab- $\alpha$ CRP/Pt(MPA)-PPy/ITO-glass bioelectrode before and after incubating with different concentrations of Ag- $\alpha$ CRP in PBS (pH 7.4) with 0.1 M KCl solution containing 2 mM  $[\text{Fe}(\text{CN})_6]^{3-/4-}$  (b) Corresponding bode plots
- Fig. 3.10:** Concentration dependent calibration curve of bioelectrode; the error bars represent the standard deviation from three separate experiments
- Fig. 4.1:** XRD pattern of the ZnS(MPA) nanoparticles; Inset: TEM micrograph of the ZnS(MPA) nanoparticles
- Fig. 4.2:** Schematic representation of the stepwise fabrication of the bioelectrode
- Fig. 4.3:** Contact angle measurement images of the (a) ITO-glass plate; (b) APTES/ITO-glass; (c)ZnS(MPA)/APTES/ITO-glass; (d)Ab-Mb/ZnS(MPA)/APTES/ITO-glass
- Fig. 4.4:** (a) 3D AFM image of the APTES/ITO-glass; (b) 3D AFM image of the ZnS(MPA)/APTES/ITO-glass; (c) and (d) 2D and 3D AFM images of

the magnified ZnS(MPA)/APTES/ITO-glass; (e) and (f) 2D and 3D AFM images of the Ab-Mb/ZnS(MPA)/APTES/ITO-glass

**Fig. 4.5:** CV of the bare ITO-glass; APTES/ITO-glass; ZnS(MPA)/APTES/ITO-glass; Ab-Mb/ZnS(MPA)/APTES/ITO-glass and Ab-Mb(BSA)/ZnS(MPA)/APTES/ITO-glass in PBS (pH 7.4, 0.1 M KCl) containing 2 mM  $[\text{Fe}(\text{CN})_6]^{3-/4-}$ ; 3rd cycle of CV is shown

**Fig. 4.6:** (a) Nyquist plots obtained on the bare ITO-glass, APTES/ITO-glass, ZnS(MPA)/APTES/ITO-glass and Ab-Mb(BSA)/ZnS(MPA)/APTES/ITO-glass in PBS (pH 7.4) containing 2 mM  $[\text{Fe}(\text{CN})_6]^{3-/4-}$  (b) Corresponding Bode plots

**Fig. 4.7:** CV of bioelectrode as a function of scan rate in PBS (pH 7.4) containing 2mM  $[\text{Fe}(\text{CN})_6]^{3-/4-}$ ; Inset: plot of redox peak current vs  $v^{1/2}$

**Fig. 4.8:** (a) Nyquist plots obtained on bioelectrode for control and different concentration of Ag-Mb in PBS (pH 7.4); (b) Corresponding bode plots

**Fig. 4.9:** Concentration dependent calibration curve of the bioelectrode; the error bars represent the standard deviation from three separate experiments

**Fig. 5.1:** Schematic representation of stepwise fabrication of the bioelectrode

**Fig. 5.2:** Contact angle measurement images of (a) ITO coated glass plate; (b) APTES/ITO-glass; (c) Pt(MPA)/APTES/ITO-glass and (d) Ab-cMb/Pt(MPA) /APTES /ITO-glass

**Fig. 5.3:** XRD Pattern of Pt nanoparticles

**Fig. 5.4:** HRTEM micrographs showing (a) distribution of nanoparticles (b) atomic scale images of different particles (c) Gaussian size-distribution curve of the nanoparticles obtained from figs. (a) and (b). X-axis: 1.5 nm to 8.5 nm (size of particles) and Y-axis: 0 to 20 (no. of particles)

**Fig. 5.5:** EDX spectra of Pt (MPA) nanoparticles on ITO-glass ; Inset:

corresponding SEM area at the magnification of 50 KX

- Fig. 5.6:** FTIR spectra of (a) APTES/ITO-glass (b) Pt(MPA)/APTES/ITO-glass and (c) Ab-cMb/ Pt(MPA)/ APTES/ITO-glass
- Fig. 5.7:** AFM images of (a) APTES/ITO-glass (b) Pt(MPA)/APTES/ITO-glass and (c) Ab-cMb/Pt(MPA)/APTES/ITO-glass
- Fig. 5.8:** (a) Nyquist plots obtained for bare ITO glass plate; APTES/ITO-glass; Pt(MPA)/APTES/ITO-glass; Pt/APTES/ITO-glass and Ab-cMb(BSA)/Pt(MPA)/APTES/ITO-glass in PBS containing 2mM  $[\text{Fe}(\text{CN})_6]^{3-/4-}$ ; (b) Corresponding bode plots
- Fig. 5.9:** CV of bioelectrode as a function of scan rate in PBS containing 2mM  $[\text{Fe}(\text{CN})_6]^{3-/4-}$ ; Inset: plot of redox peak current vs  $v^{1/2}$ .
- Fig. 5.10:** (a) Faradaic impedance spectra of the bioelectrode before and after incubating with different concentration of Ag-cMb in PBS containing 2 mM  $[\text{Fe}(\text{CN})_6]^{3-/4-}$ , (b) Corresponding bode plots.
- Fig. 5.11:** Concentration dependent calibration curve of the bioelectrode; the error bars represent the standard deviation from three separate experiments
- Fig. 6.1:** Electrochemical reduction of GO/APTES/ITO-glass surface in a deaerated solution of 0.5 M KCl, at a scan rate of  $50 \text{ mV s}^{-1}$
- Fig. 6.2:** Schematic representation of the stepwise fabrication of the bioelectrode
- Fig. 6.3:** Contact angle measurement images of (a) ITO coated glass plate; (b) APTES/ITO-glass; (c) GO/APTES/ITO-glass; (d) RGO/APTES/ITO-glass; (e) ZnS(MPA)-RGO/APTES/ITO-glass; (f) Ab-cMb/ZnS(MPA)-RGO/APTES/ITO-glass
- Fig. 6.4:** SEM images of (a) RGO/APTES/ITO-glass at the magnification of 5 KX and (b) ZnS(MPA)-RGO/APTES/ITO-glass at the magnification of 20 KX

- Fig. 6.5:** (a) HRTEM image showing the nano-sheets of GO. Insets: (A) atomic scale image of GO and (B) corresponding selected area electron diffraction pattern; (b) Composite of nano-sheets of GO with nano-particles of ZnS. Inset: corresponding selected area electron diffraction pattern from GO and ZnS and (c) atomic scale image revealing inter-planar spacing of both GO and ZnS
- Fig. 6.6:** HRTEM image and corresponding EDX chemical measurements showing; (a) composite microstructure of nano-sheets of GO with nano-particles of ZnS, (b) corresponding EDX spectrum with X-axis: 0 to 10 keV and Y-axis: Intensity in arbitrary unit, (c) elemental map of C, (d) elemental map of Zn, (e) elemental map of S and (f) overlapped elemental maps of C, Zn and S
- Fig. 6.7:** (a) Nyquist plots obtained for bare ITO glass; APTES/ITO; GO/APTES/ITO; RGO/APTES/ITO; ZnS(MPA)-RGO/APTES/ITO; and Ab-cMb(BSA)/ZnS(MPA)-RGO/APTES/ITO in PBS containing 2 mM  $[\text{Fe}(\text{CN})_6]^{3-/4-}$ , (b) Corresponding bode plots
- Fig. 6.8:** CV of bioelectrode as a function of scan rate in PBS (pH 7.4, 0.1M KCl) containing 2mM  $[\text{Fe}(\text{CN})_6]^{3-/4-}$ ; Inset: plot of redox peak current vs  $v^{1/2}$
- Fig. 6.9:** (a) Faradaic impedance spectra of the bioelectrode before and after incubation with different concentration of Ag-Mb in PBS (pH 7.4) with 0.1 M KCl solution containing 2 mM  $[\text{Fe}(\text{CN})_6]^{3-/4-}$ , (b) Corresponding bode plots
- Fig. 6.10:** Concentration dependent calibration curve for Ab-cMb/ZnS(MPA)-RGO/APTES/ITO and Ab-cMb(BSA)/RGO/APTES/ITO bioelectrode; error bars represent the standard deviation from three separate experiments

## LIST OF TABLES

---

- Table 1.1:** Summary of prominent clinically utilized cardiac biomarkers for the diagnosis of various forms of CVD
- Table 2.1:** Electron charge transfer properties of bare and modified polymer-composite electrodes before and after protein Ag- $\alpha$ CRP immobilization.
- Table 3.1:** EIS parameters at various stages of surface modification of the electrodes
- Table 3.2:** EIS characteristic parameters of the bioelectrode upon immunoreaction
- Table 3.3:** Comparison of analytical performance of electrochemical sensors for Ag-  $\alpha$ CRP
- Table 4.1:** CV & EIS parameters at various stages of surface modifications of the electrode
- Table 4.2:** EIS characteristic parameters of the bioelectrode upon immunoreaction
- Table 5.1:** EIS parameters at various stages of surface modification of the electrodes
- Table 5.2:** EIS characteristic parameters upon immunoreactions with different concentrations of protein, Ag-cMb
- Table 5.3:** Analytical performance of some electrode systems for Mb detection
- Table 6.1:** CV and EIS characteristics parameters at various stages of electrode fabrication
- Table 6.2:** EIS characteristics parameters of the bioelectrode on immunoreaction with different concentration of target Ag-cMb

## Part I: An Overview and General Introduction

---

### 1.1 Biosensors

Since the dawn of time, mankind has been performing bioanalysis using the sensory nerve cells of their nose to detect scents or the enzymatic reactions in their tongue to taste a variety of foods. Although the canaries used in coal mines could qualify as the first biosensors, the feasibility of biosensing was first demonstrated by Leland C. Clark in the mid-1960s [1], when he measured glucose concentration in solution using what has since become known as the Clark oxygen electrode. Since then, hundreds of biosensors have been developed around the world and over 200 research papers about biosensors have been published each year over the past decade [2]. Over the years, scientists have developed new means of chemical analysis using bioreceptors from biological organisms that often has the high selectivity of biological recognition systems. These biorecognition elements along with different transduction methods have helped to create the rapidly expanding field of bioanalysis and related technology known as biosensors.

According to IUPAC the term biosensors refers to ‘*A device that uses specific biochemical reactions mediated by isolated enzymes, immuno systems, tissues, organelles or whole cells to detect chemical compounds usually by electrical, thermal or optical signals*’ [3]. The rapid development in molecular biology and biomolecular engineering has expanded the list of possible biorecognition elements such as, whole-



cells, cell organelles, tissues, enzymes, antibodies, nucleic acids and proteins. These biological recognition elements in conjunction with a physicochemical transduction mechanism (electrochemical, optical, electrical, piezoelectric, thermal and magnetic) make possible to recognize and quantify specific molecules in a complex solution with high specificity and sensitivity. The advances in signal transduction and data analysis research with accelerated technological breakthroughs related to electronics, informatics, data mining and computer technologies, have lead to the development of more reliable, low cost, portable and easy to use biosensors. The combination of biorecognition molecule and the transducer is often a critical step in biosensor development and can be performed by membrane entrapment, physical adsorption, matrix entrapment, or covalent binding among others.

Biosensors represent a rapidly expanding field having publications of tens of thousands of papers in this area. According to a new market report published by Transparency Market Research in 2011, the global biosensors market was valued at USD 9.9 billion and it is expected to reach a market of USD 18.9 billion by 2018 [4]. Scientists from across the fields of science have contributed to the development of reliable and robust biosensing devices for applications in the fields of medical/clinical analysis [5, 6], veterinary [7], agriculture [8], food quality [9], environmental analysis [10] and bioterrorism prevention [11].

## **1.2 Basic concept of biosensor**

As demonstrated in Fig. 1.1, a biosensor mainly consists of two elements in spatial proximity:

1. The *sensitive biological element* i.e., a biological material (e.g., tissue, microorganisms, organelles, cell receptors, enzymes, antibodies, nucleic acids etc.), a biologically derived material or biomimic which can be created and modified by biological engineering.
2. The *transducer element* which is able to convert the recognition event into a measurable signal (optical, piezoelectric, electrochemical, thermometric, or magnetic).

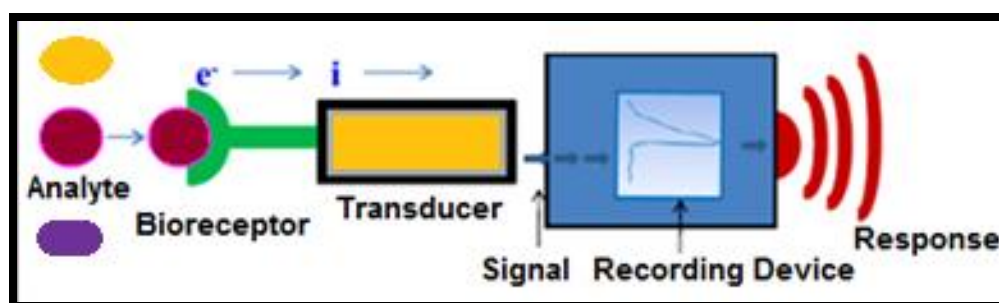


**Fig. 1.1:** Schematic representation of a biosensor

The method of immobilization of bioreceptors is a critical factor in the construction of a biosensor and can greatly affect its performance. There are mainly four different methods to combine bioelements with that of sensor elements namely: membrane entrapment, physical adsorption, covalent binding and electrochemical immobilization. In the membrane entrapment scheme, a semipermeable membrane attached to the biosensor, separates the analyte and the bioelement. The physical adsorption scheme is dependent on a combination of van der Waals forces, hydrophobic forces, hydrogen bonds and ionic forces to attach the biomaterial to the surface of the transducer. In electrochemical immobilization the biomolecules are entrapped in the layers of electrochemically synthesized polymers. While, in the case of the covalent

bonding, the sensor surface is treated as a reactive group to which the biological materials can bind chemically. Generally, covalent immobilization is preferred over physical adsorption to avoid leaching of the bioreceptor elements from the substrate matrix. Covalent binding of bioelements has a number of advantages that include high binding strength, specific orientation of molecules and improved stability.

Molecular recognition processes in biosensors are governed by the interplay of non-covalent interactions of comparable strengths such as ionic binding, van der Waals interactions, formation of hydrogen bonds and hydrophobicity between the residues of the biomolecules which lead to the formation of a complex where the two biomolecules form a mutual interface consisting of one or more patches on their surfaces. The selectivity of biomolecular recognition is thus only achieved if a large number of functional groups of the two molecules contribute co-operatively to a sufficient number of corresponding non-covalent bonds. This mutual effect between the biomolecules is often called complementarity in the literature. Antibodies are complex biological molecules made up of hundreds of individual amino acids arranged in a highly ordered sequence and exhibit very specific binding capabilities for specific structures. The antigens binds specifically to the antibody in a manner analogous to a lock and key fit, where only a specific geometrical configurations of a unique key enables it to open a lock [12]. This unique property of antibodies is the key to their usefulness in immunosensors where only the specific analyte of interest, the antigen, fits into the antibody binding site.

### **1.3 Classification of biosensors**

Biosensors can be classified into various groups either by the type of transducer employed or the kind of bio-recognition element utilized.

#### *1.3.1 Classification based on biorecognition element*

The key to specificity for biosensor involves bioreceptors that are responsible for binding the analyte of interest to the sensor for the measurement. The biomolecules that are most relevantly used for the biosensor fabrication has been discussed below.

##### *1.3.1.1 Enzyme based biosensors*

Enzymes are folded polypeptides (polymers of amino acids) which catalyze chemical reactions without being used up in the conversion of substrates to products producing a detectable signal in a biorecognition process. Enzymes are the most widely used recognition element due to their unique specificity and sensitivity [13]. However, the major disadvantage of this type of biosensor is that the purification of enzymes is costly and time-consuming. In addition, the in vitro operating environment can result in reduced enzyme activity. Also, there are a limited number of substrates for which enzymes have been evolved.

##### *1.3.1.2 Antibody based biosensors*

Antibodies (Ab) are proteins that show outstanding selectivity. They are produced by  $\beta$ -lymphocytes in response to antigenic structures which are substances foreign to the organism. Immunosensors are Ab-based affinity biosensors where the detection of an

analyte, an antigen (Ag) or hapten, is brought about by its binding to a region of an Ab [14]. Antibodies are usually immobilized on the surface of the transducer by covalent attachment via conjugation of amino, carboxyl, aldehyde, or sulfhydryl groups. The surface of the transducer must be previously functionalized with an amino, carboxyl, hydroxyl, or other group. The electrochemical transducer responds to the binding event between Ab-Ag and converts the electrical response to an output that can be amplified, stored and displayed. Complementary regions of the Ab (paratope) bind to an Ag (epitope) with high specificity and affinity [15].

Immunosensors are well known for both quantitative and qualitative applications due to their extremely low detection limits and can be used to detect trace levels (ppb, ppt) of bacteria, viruses, drugs, hormones, pesticides, and numerous other chemicals. Various examples of immunosensor applications include monitoring food safety [16-18], detecting environmental pollutants such as herbicides and pesticides in water and soil [19], detecting biomedical substances [20] and monitoring for biowarfare agents such as toxins, bacteria, viruses, and spores [21, 22].

#### *1.3.1.3 Whole-Cells based biosensors*

In whole cell based biosensors, we have cells or engineered bacteria acting as a sensing element that specifically recognizes species of interest [23]. This type of biosensor utilizes transduction signals performed by the production of an easily quantifiable marker protein. An existing regulatory system in the bacterial cell is used in most cases, to drive the expression of a specific reporter gene, such as bacterial green fluorescent protein, beta-galactosidase and others [24]. The advantage of whole cells biosensors is that their

response is obtainable within several minutes or hours in comparison to bioassays which normally require several days or a week. However, their selectivity is generally low because of the involvement of several reaction pathways.

#### *1.3.1.4 DNA based biosensors*

Biosensors based on DNA gain their high sensitivity and selectivity from the very strong base pair affinity between complementary sections of lined up nucleotide strands. For the known sequence of bases in DNA molecule the complementary sequence, called a probe, is synthesized and employed to detect specific sequences of DNA. Electrochemical detection of the formation of a DNA duplex, called hybridization event, is based on the electrochemical signals due to labeling of the target or the probe with covalently bound electroactive species (e.g. nanoparticles), or changes in various electrochemically detectable DNA properties related to changes in the DNA structure resulting from the hybridization step [25]. DNA-based biosensors have been used for the determination of drug in blood serum matrix [26], detection of the DNA damage and antioxidants protecting DNA from its damage [27, 28] and voltammetric determination of 1-aminopyrene and 1-hydroxypyrene [29].

#### *1.3.1.5 Aptamer based biosensors*

Aptamers can be defined as *in vitro* selected single-stranded functional oligonucleotides that can fold into distinct three-dimensional conformations and are capable of binding strongly and selectively to a target molecule. Aptamers exhibit many advantages as recognition elements in biosensing when compared to traditional antibodies. They are

small in size, chemically stable and cost effective. More importantly, aptamers offer remarkable flexibility and convenience in the design of their structures, which has led to the development of novel biosensors that have exhibited high sensitivity and selectivity. Therefore, production, miniaturization, integration and automation of biosensors can be accomplished more easily with aptamers than with antibodies [30, 31].

### *1.3.2 Classification based on the transduction method*

#### *1.3.2.1 Electrochemical biosensors*

Most biosensors use electrochemical detection for the transducer because of the low cost, ease of use, portability, and simplicity of construction [32,33]. Electrochemical biosensors combine the sensitivity, as indicated by low detection limits of electrochemical transducers, with the high specificity of biological recognition processes [34,35]. The reaction being monitored electrochemically typically generates a measurable current (amperometry), a measurable charge accumulation or potential (potentiometry) or alters the conductive properties of the medium between electrodes (conductometry). These three signal-transduction mechanisms are briefly discussed below.

##### *1.3.2.1.1 Potentiometric*

Potentiometric sensors are based on measuring the potential of an electrochemical cell while drawing negligible current. This type of sensor uses an electrochemical cell with two electrodes (working and reference) to measure the potential across a membrane that selectively reacts with the charged ion of interest [36]. The main advantage of such

device is the wide concentration range for which ions can be detected, generally between  $10^{-6}$  M to  $10^{-1}$  M. Their continuous measurement capability is also an interesting possibility for environmental applications. The main disadvantage of this type of sensors is that the limit of detection for some samples can be high and the selectivity can be poor. Generally the potentiometric sensors can be based on the ion-selective electrodes [37], the metal-oxide sensitive field effect transistor [38], the ion-sensitive field effect transistor [39], the enzyme field effect transistor [40] and the light addressable potentiometric sensor [41].

#### *1.3.2.1.2 Amperometric*

In amperometry, changes in current generated by the electrochemical oxidation or reduction of an electro active species are monitored directly with time while a constant potential is maintained at the working electrode with respect to a reference electrode [42]. It is usually performed by maintaining a constant potential at a Pt, Au or C based working electrode or an array of electrodes with respect to a reference electrode, which may also serve as the auxiliary electrode, if currents are low ( $10^{-9}$  to  $10^{-6}$  A). The resulting current is directly correlated to the bulk concentration of the electroactive species or its production or consumption rate within the adjacent biocatalytic layer. As biocatalytic reaction rates are often chosen to be first-order dependent on the bulk analyte concentration, such steady-state currents are usually proportional to the bulk analyte concentration. The main advantages of this class of transducer are the low cost and high degree of reproducibility. Limitations for amperometric measurements include the necessity of electrode pretreatment for obtaining reproducible surface, electrode

---



geometry effect on sensor response and permanent data correction due to the effect of background solution as a result of interference with nonspecific elements present in the solution.

#### *1.3.2.1.3 Impedimetric*

Electrochemical biosensors using impedance spectroscopy, to detect analytes have recently gained popularity among the biosensor community [43-47]. Electrochemical impedance spectroscopy (EIS) was first described by Lorenz and Schulze in 1975. Impedance is the measure of the hindered flow of ions through solutions, interfaces and coatings. EIS measures the impedance ( $Z$ ) of a system as a function of frequency of an applied perturbation which is normally an applied AC voltage of small amplitude (typically 5–10 mV peak-to-peak). The response of this applied periodic small amplitude ac signal is a current that differs in amplitude and phase (phase difference,  $\phi$ ) with the applied voltage. The consequent analysis of the system response provides information regarding the electrical behavior of the interface and interaction occurring on it. The time dependent signal  $Z(t)$  is converted into a frequency dependent signal  $Z(\omega)$  by a Laplace transformation, whereby the impedance becomes a complex number and can be calculated as follows (Eqn. 1.1).

$$Z(\omega) = E / I = E_0 \cos(\omega t) / I_0 \cos(\omega t + \phi) \quad (1.1)$$

where,  $\omega$  = frequency of the applied potential,  $\phi$  = phase angle,  $E$  = alternating voltage,  $E_0$  = amplitude of the alternating voltage,  $I$  = alternating current and  $I_0$  = amplitude of the alternating current.

EIS is an easily applicable sensitive technique to get information about the adsorption behavior and the interactions of biomolecules with the electrode surface in short measurement duration [48-50]. Electrochemical processes can be modeled by an equivalent circuit and various parameters reflecting certain properties of the interface can be determined (the detailed description has been provided in section 1.12). It can be used to monitor immunological binding events such as Ab-Ag binding on an electrode surface, where the small changes in impedance are proportional to the concentration of the measured species, Ag. Electrochemical immunosensors has attracted numerous interests due to its inherent benefits over the other transduction schemes, such as a high sensitivity, ease of use, a possible automation and integration in compact analytical devices, mostly cheap and relatively simple technology of its production.

#### *1.3.2.2 Optical biosensors*

Various optical properties, such as light absorption, fluorescence, chemiluminescence, reflectance, Raman scattering, and refractive index have been exploited as transduction mechanisms for the development of optical biosensors [51,52]. However, surface plasmon resonance (SPR) has recently been used as the basis for the optical signal transduction for the biosensor development [53]. In SPR the binding of soluble target-molecules to the surface immobilized ligands changes the refractive index of the medium near the surface which can be monitored in real time to measure accurately the amount of bound analyte, its affinity for the receptor and the association-dissociation kinetics of the interaction. An extremely wide range of molecules can be analyzed, from targets with low-molecular weight to complex molecules and even whole cells, with interaction

affinities from millimolar to picomolar concentrations. Advantages of SPR technique involve real time detection and reproducible measurements for the binding reactions of chemical compounds. This feature allows kinetic evaluation of affinity interactions, typically between antibodies and antigens. The main drawback of optical biosensors is the high cost of the apparatus.

### *1.3.2.3 Piezoelectric & thermometric biosensors*

Piezoelectric biosensors are based on the coupling of the bioelement with a piezoelectric component which is usually a quartz-crystal coated with gold electrodes [54-56]. Piezoelectric biosensors operate on the principle of generation of electric dipoles on subjecting an anisotropic natural crystal to mechanical stress. Many types of materials such as quartz, tourmaline, lithium niobate or tantalate, oriented zinc oxide or aluminium nitride exhibit the piezoelectric effect. These crystals can be made to vibrate at a specific frequency with the application of an electrical signal of that frequency. The frequency of oscillation is dependent on the electrical frequency applied to the crystal as well as the crystal's mass. With the increase in the mass due to binding of molecules, the oscillating frequency of the crystal is changed and the resulting change can be measured electrically and finally used to determine the additional mass (both positive and negative one) of the crystal.

Calorimetric (thermometric) biosensors are constructed by immobilization of biomolecules onto temperature sensors. When the analyte comes in contact with the biocomponent, the reaction heat which is proportional to the analyte concentration is measured. The total heat produced or absorbed is proportional to the molar enthalpy and

the total number of molecules in the reaction. The measurement of the temperature is via a thermistor, and such devices are called as enzyme thermistors [57]. Calorimetric biosensors were used for food, cosmetics, pharmaceutical and other component analysis [58-61].

#### **1.4 Role of nanomaterials and nanocomposites in biosensors**

Although, nanomaterials and nanotechnology are new fields of science and technology but there has been a lot of research globally in these areas since a few years ago. Nanotechnology is related to manipulating and synthesizing materials at the atomic and molecular levels. With the reduction in size novel electrical, mechanical, chemical, catalytic and optical properties can be introduced in various materials which can help in developing new generation sensors that can achieve high performance. Due to their exceptional properties nanomaterials have become primary focus in the field of sensors. In the past decade many researchers were engaged in the synthesis of new nano objects and exploitation of their extraordinary properties in the field of sensor design [62, 63]. The application of nanomaterials such as nanoparticles and nanocomposites in the field of biosensors has recently attracted much interest. This can be attributed to their use as immobilization matrix for the desired bioreceptors on a transducer surface as well as their high electron conduction that may result in faster and stable biosensing devices.

The use of nanomaterials such as nanoparticles, nanowire, nanoneedle, nanosheet, nanotube, nanorod, nanobelt, etc has led to the development of ultrasensitive electrochemical biosensors due to their unique properties such as high surface area to

volume ratio, favorable electronic properties and electro catalytic activity as well as good biocompatibility. In electrochemical reactions these nanomaterials can be used to achieve direct wiring of biomolecules to electrode surface and to amplify signal of biorecognition event [64, 65]. The resulting electrochemical nanobiosensors have been applied in areas of health care diagnostics and detection of infectious organisms. The use of nanoscale materials for electrochemical biosensing have seen explosive growth in the past decade, since the report for low potential detection of NADH using carbon nanotube (CNT)-modified electrodes by Wang and co-workers [66] and the first use of gold nanoparticles as labels for electrochemical immunosensors by Limoges and co-workers [67]. Hundreds of research articles using nanomaterials for electrochemical bioassays have since been published and this continues to show an increasing tendency. There are dozens of reviews available which partly deal with use of nanomaterials for electrochemical nanobiosensors [68-75]. The recent development of advanced tools for characterizing materials at the nano or sub nanoscale has provided scientists with new insights for understanding and improving existing devices and clues for ways to design new nanostructured materials to make better sensors.

#### *1.4.1 Biocompatible Nanomaterials and Nanocomposites*

##### *1.4.1.1 Nanomaterials*

Nanoscience and nanotechnology has led to the development of materials and structures having dimensions up to billionth of a meter (nanometer), which has helped in the extension of various fields of science such as physics, chemistry, biology, engineering

and technology into previously unapproached infinitesimal length scales [76-79]. Recently, in the last few years nanostructures such as buckytubes, silicon nanorods and semiconductor quantum dots have emerged as particularly interesting classes of nanomaterials. Whitesides [80] in his paper has discussed the reasons for the fascination and growth of this inter/multidisciplinary research.

Among nanomaterials we can find structured components having at least one dimension, two dimensions or three dimensions in the nanoscale region, i.e., less than 100nm. Materials having only one dimension in the nanoscale are layers such as thin films or surface coatings, while those having two dimensions in nanoscale include nanowires and nanotubes. Materials that are nanoscale in three dimensions are particles for example colloids and quantum dots. The different characteristics of the nanomaterials that distinguish them from bulk materials include large fraction of surface atoms, high surface energy and spatial confinement. These nanomaterials have reduced number of imperfections that do not exist in the corresponding bulk materials. A unique characteristic of nanoparticle surfaces is that they bear a high fraction of edge like and corner like curved regions [81] which have more coordinatively unsaturated atoms, i.e. dangling bonds, than flat surfaces. This large fraction of less coordinated surface, corner and edge-atoms in a nanoparticle can affect its chemical reactivity and surface bonding properties. The basic composition of nanocomponents can be either organic (dendrimers, polymers, etc.), inorganic (metals, metal oxides, metal hydroxides, etc.), carbon (carbon nanotubes, graphene, fullerene etc.) or a combination of these materials. The use of nanomaterials provides several advantages. The very first advantage of nanomaterials

which promotes the attainment of miniaturization is their small size due to which it can be packed very closely together. Second, nanomaterials possess large specific surface areas due to their small dimensions leading to accelerating interactions between them and the environment in which they are located. This high surface area to volume ratio of the nanomaterials results in enhancement of the participation of surface atoms in the physical and chemical properties of the nanomaterials. As a result of the changes that occur in particles with a decrease of particle size, nanomaterials can have extremely high biological and chemical reactivity. For example, catalytically active nanomaterials accelerate chemical or biochemical reactions by tens of thousands and even a million times.

#### *1.4.1.2 Conducting Polymers*

Since the discovery in 1977 by three Noble laureates Alan J Heeger, Alan G MacDiarmid and Hideki Shirakawa [82] that conjugated polymers can be made to conduct electricity through doping, a tremendous amount of research has been carried out in the field of conducting polymers. These conducting polymers are of great scientific and technological importance because of their unique electrical, electronic, magnetic and optical properties. Electrical conductivity can be achieved in the conducting polymer film by doping of anionic or cationic species in the polymer film via oxidation (p-doping) or reduction (n-doping). Prior to doping, polymer is an insulator but subsequent doping injects free charge carriers (electrons and holes) along the polymeric  $\pi$ -backbone. This leads to rearrangement of alternative single and double bonds that takes care of mobility of charges all along the polymeric backbone and also among the

adjacent chains. A thin film of conducting polymer having both high conductivity and fine structure in nanoscale is a suitable component for the fabrication of sensors. The overall sensing mechanism in conducting polymer based sensors is based on changes in the physical, chemical or mechanical properties of the polymer when it is exposed to the analyte or probe. Conducting polymers with organized molecular structures on metal substrates can function as a three-dimensional matrix for the immobilization of biomolecules such as enzymes and can also preserve the activity for long duration. This property of biocompatibility of conducting polymers has provided opportunities for the researchers to investigate the development of conducting polymer based biosensors.

Conducting polymers can be prepared via chemical or electrochemical polymerization [83-85]. The latter is generally preferred because it provides a better control of film thickness and morphology in comparison to chemical oxidation. In electro polymerization conducting polymer films are generally deposited onto a supporting electrode surface by anodic oxidation of the corresponding monomer in the presence of an electrolyte solution which acts as a dopant. The different electrochemical techniques that can be employed for electropolymerization are potentiostatic (constant potential), galvanostatic (constant current) and potentiodynamic (potential scanning, *i.e.*, cyclic voltammetry) methods. The electropolymerization is generally achieved by potentiostatic or galvanostatic methods. These techniques are easier to describe quantitatively and have been therefore commonly utilized to investigate the nucleation mechanism and the macroscopic growth. Potentiodynamic techniques such as cyclic voltammetry has been mainly used to obtain qualitative information about the redox processes involved in the



early stages of the polymerization reaction and to examine the electrochemical behavior of the polymer film after electrodeposition [86].

#### *1.4.1.2.1 Polypyrrole*

Among the numerous conducting polymers prepared till date, polypyrrole is by far the most extensively studied. The reasons for this intense focus on polypyrrole certainly lie in the fact that the monomer (pyrrole) is easily oxidized, water soluble and commercially available. Hence, polypyrrole presents several advantages including environmental stability, good redox properties and the ability to give high electrical conductivities [87]. As a result of its good intrinsic properties, polypyrrole has proven promising for several applications including batteries [88], supercapacitors [89], electrochemical biosensors [90], gas sensors [91], solar cells [92], textiles and fibers [93] and drug delivery systems [94]. The intrinsic properties of polypyrrole are highly dependent on electro polymerization conditions. Therefore, understanding the different steps, i.e. the mechanism involved in the polymer electrodeposition can help in achieving a better control over the chemical and physical properties of polypyrrole films.

The electrochemical polymerization of pyrrole is illustrated in Fig. 1.2. The first step involved in the electropolymerization of pyrrole monomer is the formation of pyrrole radical cation as a result of initial oxidation at electrode surface. It is followed by dimerization and deprotonation. The dimer so formed gets reoxidized easily than the monomer to allow further coupling reaction to proceed. The polymer is electrochemically ionized to a conducting state and the overall electrical neutrality is maintained by incorporation of the counter ion from the supporting electrolyte. Since

pyrrole has a relatively low oxidation potential, electropolymerization can be carried out in aqueous electrolytes. The anode where oxidation of monomer takes place can be made of a variety of materials including platinum, gold, glassy carbon, and indium–tin oxide (ITO) coated glass.

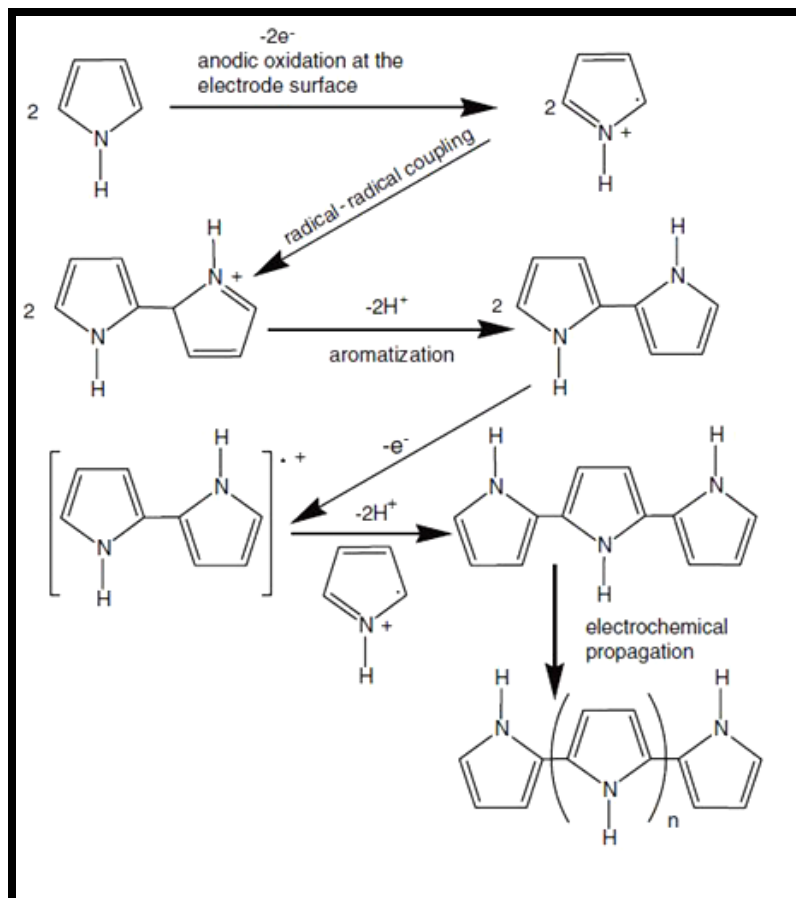


**Fig. 1.2:** Mechanism of electrochemical polymerization of Polypyrrole

#### 1.4.1.3 Nanocomposites

Recent developments in nanoparticle synthesis provided a plethora of nanomaterials whose application can be fully realized when they are mixed with conventional

polymers, metal oxides, or metals, resulting in a special class of hybrid materials known as nanocomposites [95]. Nanocomposites, i.e. composite materials with one or more nanostructured components contain hierarchically structured nanoparticles with single particle precision. These nanocomposites can not only be fabricated with different nanomaterials but also with various biomolecules and polymers to possess unique hybrid and synergistic properties characteristics of neither the incorporated component nor the host matrix. This may pave the path for the generation of nano devices to meet the demands of future technologies. Typically, nanocomposites can be classified as inorganic-inorganic nanocomposites (inorganic filler in an inorganic matrix), organic-organic nanocomposites (organic filler in organic matrix) and hybrid materials (i.e. organic in inorganic or inorganic in organic matrix).

Incorporation of nanoparticles in conducting polymer yields size dependent properties with unique electrochemical, electronic, optical and catalytic properties [95]. For example, the incorporation of gold nanoparticles in a polymer matrix significantly improves electronic conductivity, porous structure, and electrochemical stability, especially in a neutral solution. This synergy based enhancement renders this type of nanocomposites an excellent candidate for energy storage systems, chemical and biological sensors and electronic devices and could provide a universal and economic approach for an advanced functional material. In biosensors, by incorporating metal nanoparticles in a conducting polymer matrix, a porous composite is formed which ensure easy and fast exchange of substrate ions into the sensing units leading to efficient and highly sensitive electrical or electrochemical detection of various target molecules

such as DNA, RNA, proteins, polypeptides, antibodies and antigens based on molecular interactions. The immobilization of sensing units is achieved at nano dimensions and with an advanced surface area, so that the sensor possesses better stability and more effective identification potential.

## **1.5 Cardiac Biomarkers**

### *1.5.1 Cardiovascular disease*

Cardiovascular disease (CVD) is one of the most prevalent medical conditions of modern times and is one of the greatest causes of adult mortality in both developing and developed countries [96]. According to the reports of the World Health Organization (WHO), an estimated 17.5 million (30%) of all global deaths in 2005 are linked to CVD and it has been estimated that by 2015, CVD will be the leading cause of death in the developing countries [97]. CVD related conditions are also responsible for massive burden on healthcare services and the economy. From 2005 to 2015 India is projected to lose approximately USD 236 billion due to CVDs. The main factors contributing significantly to this problem and exaggerating it are lifestyles, lack of clearly defined risk assessment criteria, consistently high incidences of misdiagnosis and inappropriate referrals. One of the most immediately life threatening forms of CVD is acute myocardial infarction (AMI), which is defined as the necrosis of cardiac myocytes following prolonged ischemia. As AMI causes irreversible damage to the heart, a patient suspected of AMI must be diagnosed as quickly, efficiently and comprehensively as possible using information obtained from the readings of the electrocardiogram (ECG)

and the measurement of cardiac specific biomarkers within the patient's blood. In the acute setting, the need for rapid accurate diagnosis concomitant with superior prognostic prescience has become a major priority to facilitate more timely and efficacious intervention.

The symptoms of AMI include chest pain, pressure, tightness, shortness of breath and heartburn sensations but these can also be associated with panic disorder, stable angina, gastrointestinal disease, musculoskeletal pain and viral infection. Hence, these symptoms are not adequate for correct diagnosis in primary medical clinic. Ladue et al., in 1954, first documented the use of biochemical markers in the study of AMI, when it was reported that glutamate oxaloacetic transaminase activity in serum increased above the reference range a few hours after the onset of AMI, reaching a peak after 2 to 3 days [98]. Nowadays, measurement of cardiac markers in blood samples plays a fundamental role in the diagnosis, prognosis, and risk stratification of patients with suspected AMI [99].

### *1.5.2 Cardiac biomarkers and their application*

An ideal biomarker would possess the following properties:

- Small size, facilitating quick release from injured tissues for early diagnosis
- Tissue specificity: exclusive in cardiac muscle
- High sensitivity: abundant in cardiac tissue
- the capability to remain elevated for a reasonable length of time to allow a suitable diagnostic window
- the ability to be assayed quantitatively with cost and time efficiency

Even though, the parameters mentioned above are critical for monitoring potential AMI patients, there is no cardiac biomarker that can meet all the requirements. Therefore, the knowledge regarding characteristics of biomarkers is vital for both research and clinical applications. Details about several cardiac biomarkers are discussed below and summarized in table 1.1.

#### *1.5.2.1 Myoglobin*

Although not cardiac-specific, cardiac myoglobin (Mb) is one of the earliest known biomarkers for AMI [100]. Mb, a 17.8 kDa monomeric hemeprotein of 153 amino acids is found in heart and skeletal muscles and is known to be an important biological index for the diagnosis of various diseases [101,102]. Due to its small molecular size and weight, Mb will quickly release into the blood stream through cytoderm (cell wall), an hour or so after the onset of AMI, and then is elevated to the peak value in 4 to 12 h, followed by a subsequent drop to baseline in 12 more hours [103,104]. Its quick release as well as its high sensitivity and high predictive value, makes Mb a valuable early screening test for AMI [105]. The normal baseline value of Mb in human blood circulation is found to be  $30 \text{ ng mL}^{-1}$ , which can shoot to  $200 \text{ ng mL}^{-1}$  or even higher within 1 h of onset of AMI and can go up to as high as  $900 \text{ ng mL}^{-1}$  during the peak hour. Commonly, Mb assays are done to assist in the diagnosis of AMI. Either cardiac or skeletal damage can cause elevation in serum Mb; therefore test of Mb is used by the hospitals as a negative predictive value (rule out the diagnosis of AMI).

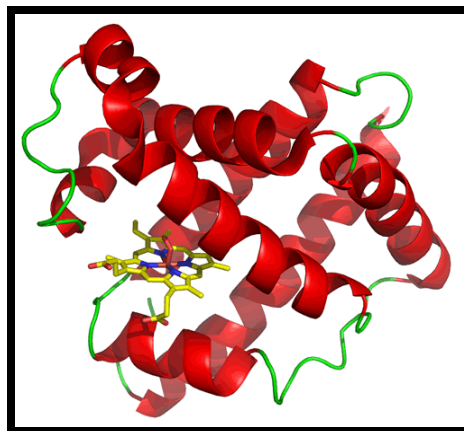


**Fig. 1.3:** Ribbon structure of Myoglobin [106]

#### 1.5.2.2 Cardiac Troponin

Cardiac troponin, a cardiac muscle regulatory protein located on the actin filament of normal myocytes, has significant sensitivity and specificity for myocardial muscle damage; therefore, it has been regarded as the “gold standard” for AMI diagnosis [107,108]. Troponin is more specific to AMI, as unlike other cardiac biomarkers which might also rise with damage to skeletal muscle, troponin levels are not generally affected by intramuscular injections, trauma, strenuous exercise, or drugs. Troponin has three subunits on the thin filament combined with myocardial contractile muscle to control the calcium ions bindings: troponin C (the component for calcium binding), cTnT (the tropomyosin binding) and cTnI (the inhibitory component). Cardiac troponins, cTnI and cTnT are highly cardiac specific and have negligible cross-reactivity with skeletal muscle troponin C. Recent researches and clinical diagnosis have suggested that cTnI is a highly specific and sensitive biomarker of AMI [109]. Generally, the cTnI levels in normal serum are below  $0.6 \text{ ng mL}^{-1}$  [110]. When its concentration reaches to

0.7–1.4 ng mL<sup>-1</sup>, minor myocardial injury can be concluded, while evident myocardial necrotic damage should be considered when cTnI concentration elevates to over 1.5 ng mL<sup>-1</sup> [111]. Since upon AMI, it takes approximately 3-12 h for the cTnI to reach detectable concentrations in blood, they cannot be considered as early markers. However, they remain elevated for 5-9 days after the onset of AMI, indicating their capability to remain elevated for a reasonable length of time to allow a suitable diagnostic window [112,113].

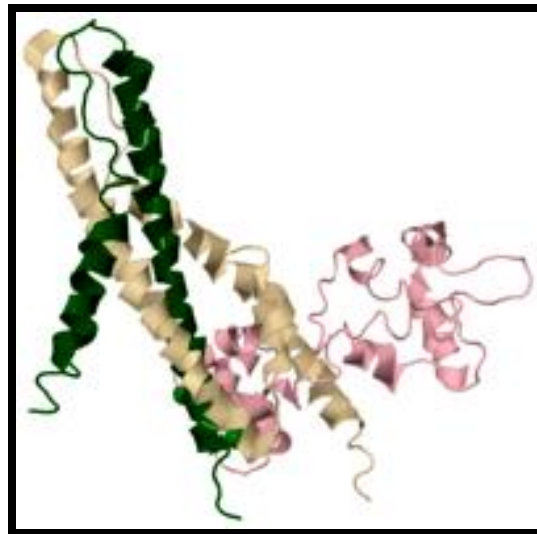


**Fig. 1.4:** Ribbon structure of Troponin [114]

#### 1.5.2.3 C - reactive Protein

C-reactive protein (CRP) was first discovered in 1930 when a soluble extract of the pneumococcus pneumoniae was added in the blood of patients with pneumococcal pneumonia leading to its precipitation. In 1941, it was named CRP because of its ability to react with and precipitate the C-polysaccharide of the pneumococcus [115]. CRP is an



acute phase protein reactant, the release of which is corresponding to acute injury, infection, or inflammation stimuli like hypersensitivity, inflammatory diseases, necrosis, trauma, and malignancy. CRP belongs to the pentraxin family of proteins (5 subunits, protomers, non-covalently bound in a cyclic form), and is produced by hepatocytes, mainly under transcriptional control by the cytokine IL-6 [116,117]. CRP, which exists in concentrations of  $1\text{--}3\ \mu\text{g mL}^{-1}$  in the serum of healthy patients, is synthesized by the liver and is widely accepted as a biomarker for CVD and inflammation. When released in the circulation it is equally distributed in the vascular compartment without substantial tissue sequestration at sites of inflammation [118]. The risks for CVD defined by the American Heart Association and the Center for Disease Control and Prevention are: low for a CRP concentration below  $1\ \mu\text{g mL}^{-1}$ , moderate for a CRP level from  $1\ \mu\text{g mL}^{-1}$  to  $3\ \mu\text{g mL}^{-1}$  and high for concentrations greater than,  $3\ \mu\text{g mL}^{-1}$  [119].

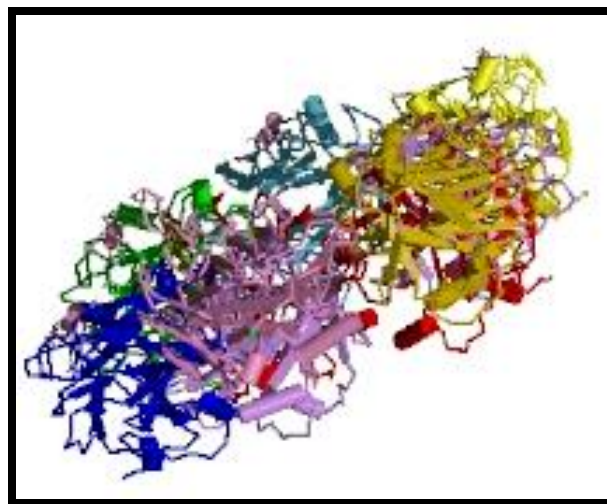


**Fig. 1.5:** *Ribbon Structure of Human C-reactive protein* [120]

**Table 1.1:** Summary of prominent clinically utilized cardiac biomarkers for the diagnosis of various forms of CVD

Cardiac biomarker	Clinical cut-off levels	Initial elevation above clinical cut-off (h)	Duration of elevation	CVD indicator type
Troponin I	0.01–0.1 ng mL <sup>-1</sup>	3-12	5–9 days	Detection of AMI and tool for risk stratification
Troponin T	0.05–0.1 ng mL <sup>-1</sup>	3-4	10–14 days	Detection of AMI and tool for risk stratification
Myoglobin	30–200 ng mL <sup>-1</sup>	1–3	12–24 h	Early detection of MI
C- Reactive Protein	<1 µg mL <sup>-1</sup> low risk, 1–3 µg mL <sup>-1</sup> intermediate risk >3–15 µg mL <sup>-1</sup> high risk.	No clinical consensus ~1–3	No clinical consensus	CVD related inflammatory response based biomarker.

**Chapter 1**  
**(Part II)**  
**Characterization Techniques**

*This part of chapter 1 gives details about the various experimental techniques employed for the nanomaterials characterization and the measurement of the electrochemical properties at different stages of the bioelectrode fabrication and its application thereof.*

## 1.6 X-ray Diffraction

In 1919 A.W. Hull gave a paper titled, “A New Method of Chemical Analysis” in which he pointed out that “....every crystalline substance gives a pattern; the same substance always gives the same pattern; and in a mixture of substances each produces its pattern independently of the others.” About 95% of all solid materials can be described as crystalline. XRD is an instrumental technique in which X-rays interact with a crystalline substance (phase) and one gets a diffraction pattern. This diffraction pattern of a pure substance is, therefore, like a fingerprint of the substance. The three-dimensional structure of crystalline materials is defined by regular, repeating planes of atoms that form a crystal lattice. When a focused X-ray beam interacts with these planes of atoms, part of the beam is transmitted, part is absorbed by the sample, part is refracted and scattered, and part is diffracted (Fig. 1.6).

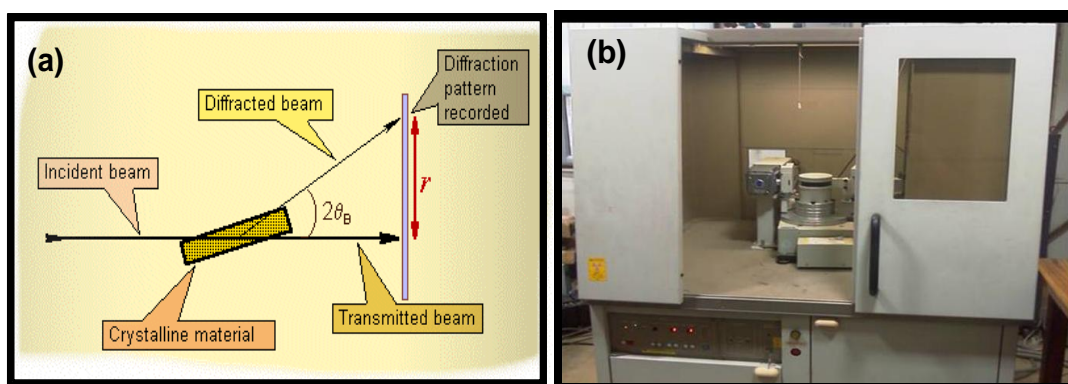


**Fig. 1.6:** (a) A schematic layout of XRD (b) X-ray Powder Diffractometer

Each diffracted X-ray signal corresponds to a coherent reflection, called Bragg reflection, from successive planes of the crystal for which Bragg's Law (Eqn.1.2) is satisfied:

$$2d \sin\theta = n\lambda \quad (1.2)$$

where the integer  $n$  is the order of the diffracted beam,  $\lambda$  is the wavelength of the incident X-ray beam,  $d$  is the distance between adjacent planes of atoms (the  $d$ -spacings), and  $\theta$  is the angle of incidence of the X-ray beam. Since the value of  $\lambda$  is known and we can measure  $\theta$ , the  $d$ -spacings values can be calculated using (Eqn. 1.2). The characteristic set of  $d$ -spacings and their intensity generated in a typical X-ray scan provides a unique 'fingerprint' of the phases present in the sample. When properly interpreted by comparison with standard reference patterns and measurements, this 'fingerprint' allows for identification of the material. The presence of an amorphous material in the sample can be determined by occurrence of specific wide halo on diffraction pattern. The analysis of X-ray diffraction pattern provides a variety of information which includes qualitative (phase identification) and quantitative (lattice parameter determination and phase fraction analysis). The peak positions contain information about crystal system, space group symmetry, translational symmetry, unit cell dimension and qualitative phase identification. The information contained in peak intensities is unit cell contents, point symmetry and quantitative phase identification. The analysis of peak shape and width (full-width at half maximum) of the Bragg peaks of the X-ray diffraction pattern provide information on the crystallite size and strain. A perfect crystal would extend in all directions to infinity, so one can say that no crystal is perfect due to its finite size. This

deviation from perfect crystallinity leads to a broadening of the diffraction peaks. However, above a certain size (100-500 nm) this type of broadening is negligible. Since the peak broadening arises from a combination or convolution of crystallite size, microcrystalline strain and instrumental broadening effects, it is necessary to correct for the instrumental broadening and to sort out the strain components to determine the average crystallite size. Scherrer formula provides average crystallite size if strains and instrumental broadening are corrected. Scherrer (1918) first observed that small crystallite size could give rise to line broadening. He derived a well known equation called the Scherrer formula for relating the crystallite size to the broadening, given by Eqn. 1.3:

$$D = K\lambda/\beta \cos \theta \quad (1.3)$$

where  $D$  = crystallite size,  $K$  = Scherrer constant, somewhat arbitrary value that falls in the range 0.87-1.0,  $\lambda$  = wavelength of the radiation and  $\beta$  = full-width at half maximum (in radians) at  $2\theta$ .

### *1.6.1 Applications of XRD*

The samples for XRD analysis are typically in the form of finely divided powders or flat smooth surfaces. Moreover the samples that can be analysed constitute a vast array of materials including inorganic, organic, polymers, metals or composites. The potential applications of XRD covers almost all research fields including metallurgy, pharmaceuticals, earth sciences, polymers and composites, microelectronics and nanotechnology. The pseudo crystalline structure of mesoporous materials and colloidal

crystals can be studied using powder XRD, provided that the length scales are in the correct size regime.

## 1.7 Fourier Transform Infrared Spectroscopy

The electromagnetic radiation can be divided into different regions of spectrum as shown in Fig. 1.7.

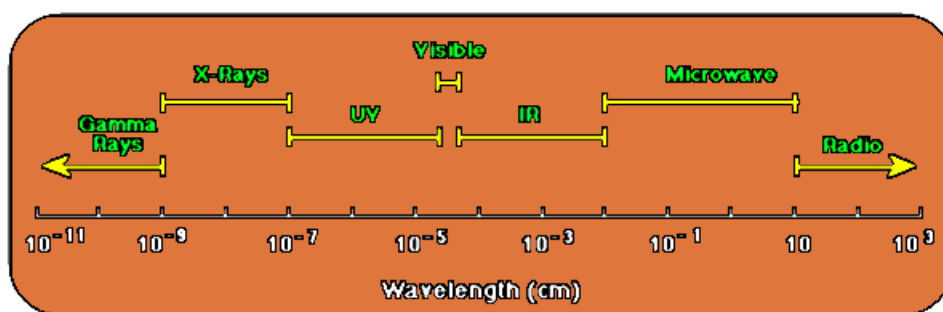


*Fig. 1.7: A graphical representation of the electromagnetic spectrum*

The term “infrared” generally refers to any electromagnetic radiation falling in the region from  $0.7 \mu\text{m}$  to  $1000 \mu\text{m}$  i.e. waves whose wavelengths are longer than the red end of visible light and shorter than microwaves. Infrared (IR) spectroscopy is the study of interactions between matter and electromagnetic fields in the IR spectral region. The population ratio of a molecule under normal conditions is steady and increases with temperature. In this spectral region, the incident IR radiation stimulates a molecule by coupling with its molecular vibrations resulting in the excitation of the molecule to a higher vibrational state. The molecules absorb only specific frequencies that are characteristic of their structure. In general, a frequency will be strongly absorbed if its photon energy coincides with the vibrational energy levels of the molecule. The exact

frequency at which a given vibration occurs is determined by the shape of the molecular potential energy surfaces, the masses of the component atoms, and the associated vibronic coupling. A vibrational mode in a molecule is said to be 'IR active' if it is associated with the changes in the permanent dipole of the molecule. A molecule can have a number of vibrational modes that give rise to absorptions. The normal modes of vibrations for molecules with  $N$  atoms are given by  $3N-5$  for linear molecules and  $3N-6$  for nonlinear molecules. For example, a tri atomic, angular molecule like  $H_2O$  produces 3 normal vibrations: one symmetrical, one asymmetric stretching vibration and a bending vibration [121] while  $CO_2$ , which is a linear molecule, has 4 normal vibrations.

Infrared spectrum can be divided into three different regions: far infrared (having wave number range  $400-100\text{ cm}^{-1}$ ), mid infrared region (having wave number range  $4000-400\text{ cm}^{-1}$ ), and the near infrared (having wave number range  $14285-4000\text{ cm}^{-1}$ ), where wave number =  $1/\lambda$  (cm). The functional groups, known as chemical structural fragments within molecules, absorb infrared radiation regardless of the structure of the rest of the molecule that the functional group is in [122,123]. Fig. 1.8 shows the general regions of the infrared spectrum in which various kinds of vibrational bands are observed with blue colored sections above the dashed line referring to the stretching vibrations while the green colored band below the line encompasses bending vibrations. The infrared spectra in the  $1450\text{ cm}^{-1}$  to  $600\text{ cm}^{-1}$  region is often called the fingerprint region because of the unique patterns found there. Absorption bands in the  $4000\text{ cm}^{-1}$  to  $1450\text{ cm}^{-1}$  region are usually due to stretching vibrations of diatomic units, and this is sometimes called the group frequency region.



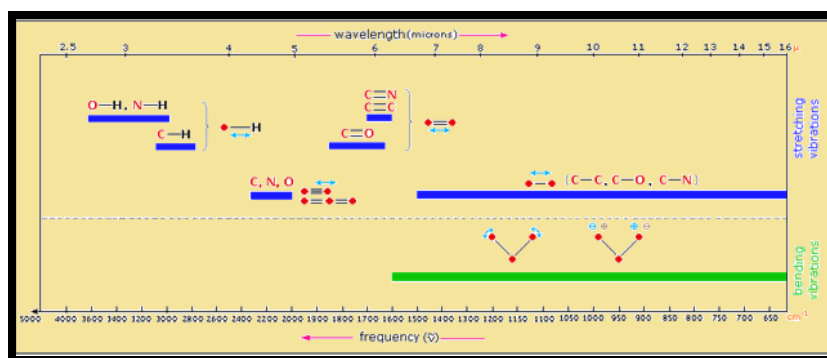


**Fig. 1.8:** Absorption bands corresponding to various regions of IR

Fourier Transform Infrared (FTIR) spectroscopy is a technique which is used to determine qualitative and quantitative features of IR-active organic or inorganic molecules in solid, liquid or gas samples. The invention of Michelson interferometer in 1880 [124] led to the development of FTIR. A diagram of a Michelson interferometer is shown in Fig. 1.9. In Michelson interferometer radiation from a broadband source strikes the beam splitter. Some of the light is transmitted to the movable mirror while some is reflected to a stationary mirror. The moving mirror modulates each frequency of light with a different modulation frequency. In general the paths of the light returning from the stationary mirror and the moving mirror are not in phase. They interfere constructively and destructively to produce a pattern called interferogram. The interferogram contains all the frequencies which make up the IR spectrum and is a plot of intensity versus time (i.e. a time domain spectrum). By performing a mathematical operation known as a Fourier Transform, the interferogram can be decomposed into its component wavelengths to produce a plot of intensity versus frequency, i.e. an FTIR spectrum.

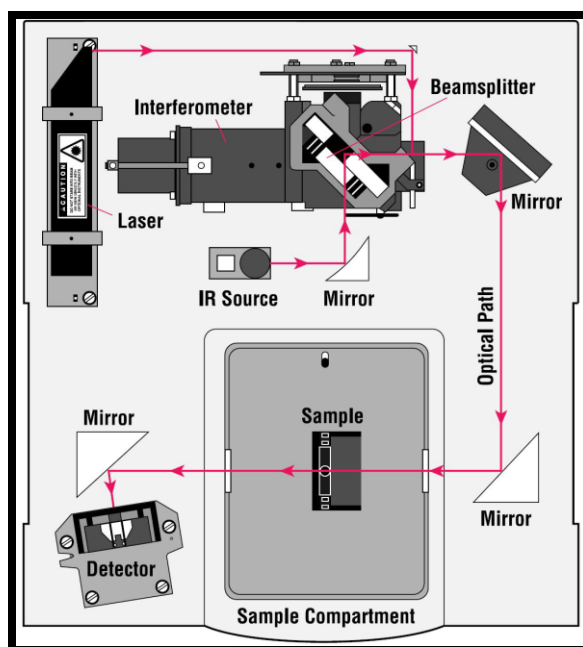


**Fig. 1.9:** A simple layout of an FTIR instrument

### 1.7.1 Advantages of FTIR

1. Multiplex advantage ( Fellgett advantage): In FTIR spectrometers since all wavelengths from the IR source impinge simultaneously on the detector, a complete spectrum can be collected very rapidly.
2. Throughput advantage (Jacquinot advantage): The Jaquinot advantage arises from the fact that the circular apertures used in FTIR spectrometers has a larger area than the slits used in grating spectrometers, thus enabling higher throughput of radiation. In combination with the Multiplex Advantage, this leads to fast scans with low noise levels.
3. Connes advantage: The use of an internal reference laser (He Ne laser) by FTIR instruments is referred to as Connes Advantage. The wave number of this laser is

known to be very accurate and stable. As a result, the wave number calibration of interferometers is very accurate and has long term stability. The advantage of internal calibration is accuracy and precision of better than  $0.1 \text{ cm}^{-1}$ .

4. Negligible stray light: There is no stray light found in FTIR spectrometers because of the way in which the interferometer modulates each source wavelength.
5. Constant resolution: In FTIR, resolution is constant at all wavenumbers in the defined spectral range but the signal-to-noise ratio varies across the spectrum. This is due to high optical throughput through aperture of fixed size, which does not change during data collection.
6. FTIR can analyze small samples of the order of nano grams.
7. FTIR is a noninvasive, simple to use, quick and economic.

### *1.7.2 Limitations of FTIR*

1. It cannot detect atoms or monoatomic ions because single atoms do not contain chemical bonds and do not possess any vibrational motion. Consequently, they absorb no infrared radiation.
2. The spectra obtained from samples are complex and difficult to interpret because it is hard to know which bands are from which molecules of the sample.
3. Its usage in aqueous solutions is also difficult to analyze since water is a strong infrared absorber in specific wave number ranges, thus it masks regions of the sample spectrum.
4. FTIR spectrometers use a single beam technique. The samples and the background are measured at different times. In order to eliminate the instrumental and

environmental contributions to the spectrum, the sample spectrum is divided by the background spectrum. However, spectral artifacts can appear in the sample spectrum as a result of instrumental or the environmental changes of water vapor and carbon dioxide concentration during the time between the sample and background.

## **1.8 Scanning Electron Microscopy**

The scanning electron microscopy (SEM) enables the investigation of solid specimens with a resolution down to the nanometer scale. It is used widely in metallurgy, geology, biology and medicine. SEM uses a focused beam of high-energy electrons which interacts with the sample to generate a variety of signals which reveals certain information about the sample external morphology (texture). The user can obtain high magnification images with a good depth of field and can also analyze individual crystals or other features with detail down to 25 Å or better. In conventional SEM techniques, areas of the samples with widths ranging from approximately 1 cm to 5 μm can be imaged in a scanning mode with magnification ranging from 20 X to approximately 30 kX having spatial resolution of 50 nm to 100 nm. When used in conjunction with the closely-related technique of energy-dispersive X-ray microanalysis (EDX), the composition of individual crystals or features can be determined.

### *1.8.1 Fundamental Principles of SEM*

The basic principle involves the generation of a beam of electrons by a suitable source, typically a tungsten filament or a field emission gun (Fig. 1.10). The electron beam is accelerated through a high voltage (e.g., 20 kV) and after passing through a system of

apertures and electromagnetic lenses becomes a thin beam of electrons which scans the surface of the specimen by means of scan coils. Electrons are emitted from the specimen by the action of the scanning beam and collected by a suitably positioned detector. These include secondary electrons, backscattered electrons and diffracted backscattered electrons. Secondary electrons provide information regarding the morphology and topography of samples while backscattered electrons illustrate contrasts in composition in multiphase samples and, thus are helpful in rapid phase discrimination.

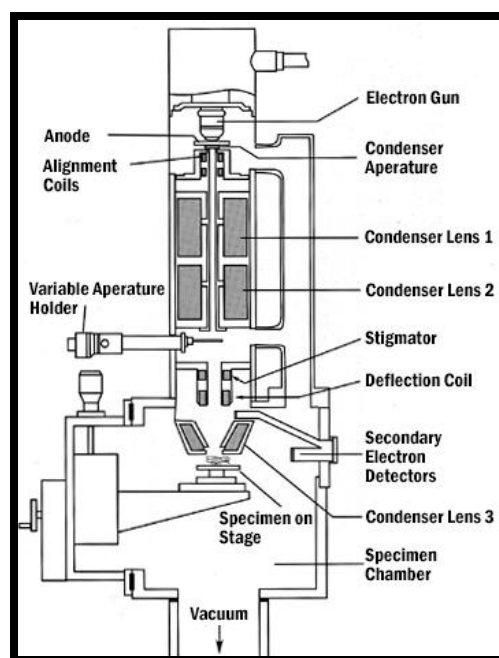


**Fig. 1.10:** A schematic layout of SEM

### 1.8.2 Advantages of SEM

SEM technique is very helpful in the study of solid materials which includes all kinds of samples, both conducting and non-conducting (sputter coated with carbon, gold or iridium). It has many advantages over traditional microscopes.

- The SEM has a large depth of field, which allows more of a specimen to be in focus at one time.
- Due to its higher resolution, closely spaced specimens can be magnified at much higher levels.
- The SEM uses electromagnets rather than lenses which allows the researcher to have much more control in the degree of magnification.

Other advantages of SEM includes minimal sample preparation, rapid data acquisition (less than 5 min/image) with data in digital formats, which are highly portable.

### *1.8.3 Limitations of SEM*

The main disadvantage is the size and cost of the SEM instrument. These are expensive, large and must be housed in an area free of any possible electric, magnetic or vibration interference. Maintenance of these instruments involves; keeping a steady voltage, currents to electromagnetic coils and circulation of cool water. Special training is required to operate an SEM instrument as well as to prepare samples. In addition, SEMs are limited to solid, inorganic samples small enough to fit inside the vacuum chamber that can handle moderate vacuum pressure.

## **1.9 Transmission Electron Microscopy**

The transmission electron microscopy (TEM) is a technique which uses a beam of highly energetic electrons to examine ultra-thin specimens on a very fine scale. An image is formed from the interaction of the electrons transmitted through the specimen, which is then magnified and focused onto an imaging device, such as a fluorescent screen,

photographic film, or is detected by a sensor such as a CCD camera. TEM instruments are capable of imaging at a significantly higher resolution (sub-nanometer) than light microscopes, owing to the small de Broglie wavelength of electrons. This enables to examine the particles in nanometer size range, which is tens of thousands times smaller than the smallest resolvable object in a light microscope. TEM is a powerful technique for characterization of materials in respect of structure and phase identification of small regions.

### *1.9.1 Principle and working of TEM*

The basic principle of TEM is quite similar to optical microscope with a major difference that instead of light a focused beam of electrons is used in TEM to create an image and achieve information regarding the structure and composition of the specimen. An electron Gun present in the TEM produces a stream of electrons which is accelerated towards the specimen using a positive electrical potential. The condenser lenses then focuses this stream of electrons into a thin, focused, monochromatic beam which strikes the specimen. A part of this focused beam gets transmitted through the specimen and is then again focused through objective lenses to form an image. Now depending on the set magnification, the image can be enlarged by the intermediate and projector lenses. After this the image strikes onto a phosphor image screen and light is stimulated, which enables the user to see the image. In the final image we have darker areas, representing the thicker or denser region of the sample, where only fewer electrons were transmitted and the lighter areas, representing thinner or less dense region, where more electrons were transmitted.

Fig. 1.11 shows a schematic layout of TEM. The column of the microscope consists of an electron gun, two stage condenser lenses and a specimen chamber. The image forming system which is composed of an objective, two stage intermediate lenses, projector lens, viewing chamber and camera are also the parts of the column. The viewing chamber consists of a viewing window to see image of specimen formed on the fluorescent screen. A binocular with a clear field of view is also installed with it to see the ten times enlarged image and also for image focusing purposes.

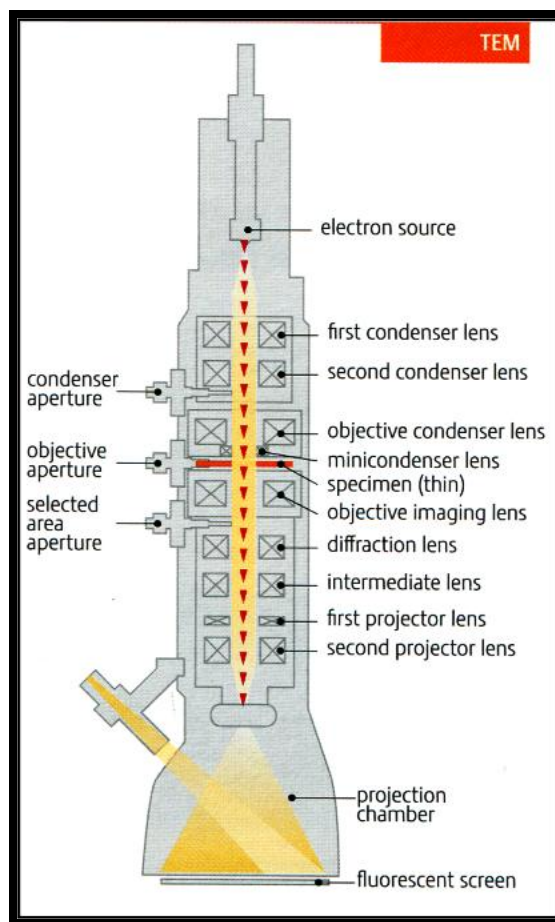


**Fig. 1.11:** A schematic layout of TEM



### *1.9.2 Application of TEM*

The main applications of TEM are as follows:

1. Microstructural investigation of material at high magnification and high resolution.
2. Determination of crystallographic structures by electron diffraction giving information about particle shape, size and size distribution of very fine powders.
3. Study of phase identification, phase transformation, epitaxial growth, lattice imaging, interface structure, defects studies, dislocations, voids, twins and stacking faults.

### *1.9.3 Limitations of TEM*

The main limitations or drawbacks of using TEM are as follows:

- The main disadvantages are cost, size, maintenance, researcher training and image artifacts resulting from specimen preparation.
- Extensive sample preparation is often required in TEM. This leads to slow scan time and lengthy time between scans.
- The basic requirement for the samples to be analyzed is that they must be electron transparent which means that the given material has to be thin on a molecular level. This can lead to unexpected changes in the sample material structure which will ultimately alter the test results.
- For biological samples the microscope itself can be hazardous as the electron beam may damage it.
- Additionally, the problem of calibration and alignment of the instrument requires experience and expertise skills, so that the resulting images and data are reliable.

## **1.10 Atomic Force Microscopy**

The Atomic Force Microscope (AFM) was developed to overcome a basic drawback with scanning tunneling microscope that it can only image conducting or semiconducting surfaces. The AFM can image almost any type of surface including polymers, ceramics, composites, glass and biological samples. Binnig, Quate and Gerber invented the AFM in 1985. Their original AFM consisted of a diamond shard attached to a strip of gold foil.

### *1.10.1 Principle and working of AFM*

The AFM utilizes a sharp probe which moves over the surface of a sample in a raster scan. The probe is a tip on the end of a cantilever which bends in response to the force between the tip and the sample. The cantilever is typically silicon or silicon nitride with radius of curvature of the tip, of the order of nanometers. When the tip is brought into proximity of a sample surface, forces between the tip and the sample lead to a deflection of the cantilever according to Hooke's law. These forces could be mechanical contact forces, van der Waals forces, capillary forces, chemical bonding, electrostatic forces, magnetic forces, solvation forces, etc. In the case of adhesive interaction between the tip and a surface, these forces are of the order 0.1- 1 nN. In order to detect the small bending caused by these weak forces, a laser beam is focused on the back of the cantilever which reflects it to a position sensitive photo detector. Depending on the cantilever deflection, the position of the reflected beam changes. The photo detector converts this change into an electrical signal. The AFM can be operated in a number of modes depending on the

application. The different imaging modes are divided into static (also called contact) modes and a variety of dynamic (non-contact and ‘tapping’) modes.

### *1.10.2 Modes of operation*

The simplest measurement method is the contact mode in which the scanning is done while the end of the tip is in mechanical contact with the sample. As the tip is raster scanned across the surface, it is deflected as it moves over the surface corrugation. An electronic feedback control keeps the resulting deflection constant by adjusting the z position and therefore constant height is maintained above the surface. However, the ability to track the surface in this manner has a disadvantage that the tip exerts forces on the sample. Although, these forces are only of the order of 0.1-1 nN, the pressure applied to the sample can easily reach 1000 bar because of the small contact area. This may lead to structural damages, especially on soft surfaces.

Noncontact mode refers to the use of an oscillating cantilever for scanning purpose. A stiff cantilever is oscillated in the attractive regime meaning that the tip is quite close to the sample, but not touching it. The forces between the tip and the sample are quite low, in the order of pN. The detection scheme is based on measuring changes to the resonant frequency or amplitude of the cantilever.

Tapping mode is also referred to as intermittent contact or in more general term dynamic force mode. This mode uses a stiff cantilever which is oscillated closer to the sample than in noncontact mode. A part of the oscillation extends into the repulsive regime, so the tip intermittently touches or taps the surface. The advantage of tapping the

surface is improved lateral resolution on soft samples. Also, lateral forces such as drag, common in contact mode are virtually eliminated.

### 1.10.3 Advantages of AFM

The AFM has several advantages:

- (i) AFM provides a true three-dimensional surface profile.
- (ii) Samples viewed by AFM do not require any special treatments (such as metal/carbon coatings) that would irreversibly change or damage the sample.
- (iii) AFM does not require an expensive vacuum environment for proper operation. Most AFM modes can work perfectly well in ambient air or even a liquid environment. This makes it possible to study biological macromolecules and even living organisms.

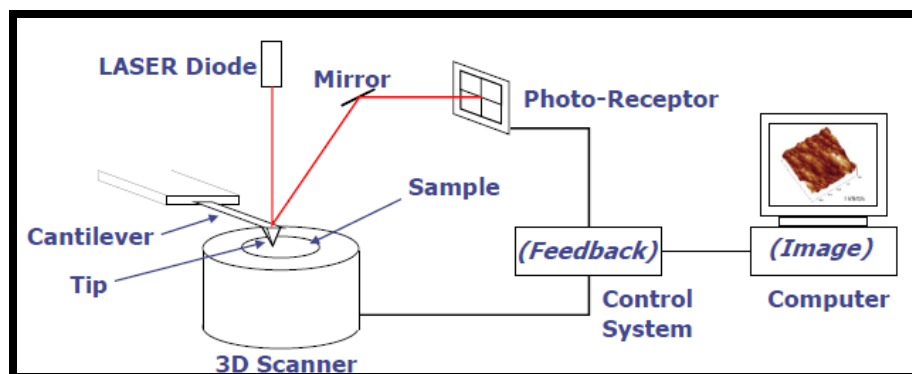


*Fig. 1.12: Block diagram of AFM*

## 1.11 Cyclic Voltammetry

Cyclic voltammetry was first reported in 1938 as an electrochemical technique which can provide both qualitative and quantitative information as well as a fast and reliable

characterization tool to probe the mechanics of redox and transport properties of a system in solution [125]. This is accomplished by using a three electrode arrangement whereby the potential relative to some reference electrode is scanned at a working electrode while the resulting current flowing through a counter (or auxiliary) electrode is monitored in a quiescent solution. The working electrode is subjected to a triangular potential sweep, whereby the potential rises from a start potential value ( $E_i$ ) to a final potential value ( $E_f$ ) then returns back to the start potential at a constant potential sweep rate (Fig.1.13a). The selected value of sweep rate applied can vary from a few millivolts per second to a few hundred millivolts per second. The current measured during this process is then plotted against the applied potential, and the result is referred to as a cyclic voltammogram (CV) (Fig.1.13 b). The voltammogram determines the potentials at which different electrochemical processes occur. A peak in the CV at a particular potential is characteristic of any electrode reaction taking place at that potential. The peak width and height for a particular process may depend on the sweep rate, electrolyte concentration and the electrode material [126, 127]. With the help of CV, kinetics of various electrochemical reactions taking place at electrode/solution interface can be easily analyzed [128, 129]. It is possible to investigate the role of adsorption, diffusion and coupled homogeneous chemical reaction mechanisms using the sweep-rate dependence of the peak amplitudes, widths and potentials of the peaks observed in the voltammograms [127, 130].

Cyclic voltammetry is of particular significance for the study of electrochemical processes that are limited by finite rates of electron transfer. Faradaic processes are non-

adsorptive processes arising from electron transfer across the electrode/electrolyte interface. The resulting redox reaction of solution species that takes place is controlled by Faraday's laws [127, 131]. Electrode surfaces where Faradaic processes take place are classified as charge transfer electrodes, since the extent of reaction depends on the measured charge passing through the electrode surface. The redox reaction taking place in the solution can be expressed as:  $O + ne^- \rightleftharpoons R$ , where O and R are the oxidized and reduced forms of the redox couple, respectively. When the electron transfer rate in both the forward and reverse directions at the electrode is high, the process is described as reversible, and the cathodic and anodic peaks are separated by a potential of approximately  $59/n$  mV at  $25^\circ\text{C}$  (Fig. 1.13 b), where  $n$  is the number of electrons transferred. In a reversible process, the peak separation ( $\Delta E_p$ ) is given by Eqn. 1.4:

$$\Delta E_p = (E_p)_{\text{ox}} - (E_p)_{\text{red}} = 59/n \text{ mV} \quad (1.4)$$

where  $(E_p)_{\text{ox}}$  and  $(E_p)_{\text{red}}$  are the potentials at which the oxidation and reduction processes occur.

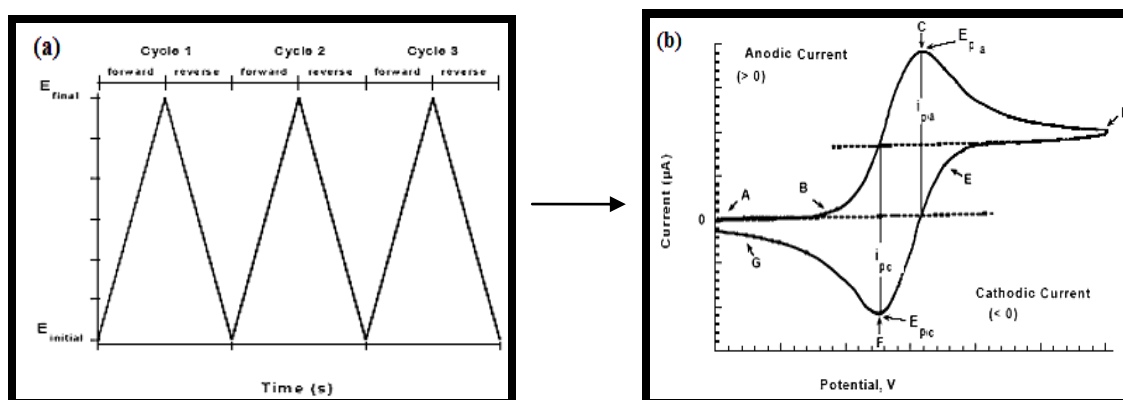


**Fig.1.13:** (a) A cyclic voltammetry potential waveform with switching potentials (b) A typical cyclic voltammogram showing reduction and oxidation peak

## 1.12 Electrochemical impedance spectroscopy

As already discussed in section 1.3.2.1.3, EIS is a measure of the variation in the impedance of a system ( $Z$ ) with frequency of an applied perturbation. In electrochemical systems this perturbation is normally an AC voltage of small amplitude (typically 5–10 mV peak-to-peak) and the response is a current that differs in amplitude and phase (phase difference,  $\varphi$ ) with the applied voltage. The AC voltage is kept small enough so that the system response is linear thus allowing a simple equivalent circuit analysis. The ratio of applied voltage to the measured current is the impedance of the system ( $Z = E/I$ ), which is easily calculated over a wide frequency range. From a physical point of view, impedance is just a totally complex resistance (measured in Ohms,  $\Omega$ ) that appears when an AC current flows through a circuit made of resistors, capacitors, inductors or any combination of these. This magnitude shows a complex notation, with a resistive or real part attributable to resistors (in phase with the applied voltage) and a reactive or imaginary part attributable to the contribution of capacitors (out of phase with the applied voltage by  $+\pi/2$ ) and/or inductors (out of phase with the applied voltage by  $-\pi/2$ ) as depicted by Eqn. 1.5:

$$Z = Z' + jZ'' = R - jX; X = 1/\omega C; j = \sqrt{-1}, \quad (1.5)$$

where  $R$  is the resistance (measured in  $\Omega$ ),  $X$  the reactance,  $C$  the capacitance (measured in Farads,  $F$ ), and  $\omega$  the applied angular frequency (measured in rad/s;  $\omega = 2\pi f$ ,  $f$  is the frequency measured in Hz).

The complete description of the electrochemical system, in terms of capacitance, resistances and impedance can be obtained by circuit fitting the experimental data to the computer simulated data using an appropriate equivalent circuit. In such circuits, a resistance ideally describes a conductive path, such as that generated by the bulk conductivity of the system or the charge-transfer step due to an electrode reaction, whereas a capacitance generally describes space-charge-polarization regions within the system as well as modification of an electrode surface due to adsorption processes or polymer-layer deposition. The Randles circuit is the simplest equivalent circuit that describes an electrochemical cell, where a single-step Faradaic process in the presence of diffusion may occur (Fig. 1.14).

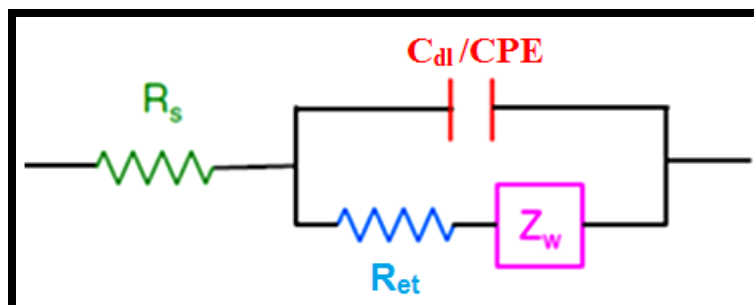


**Fig. 1.14:** Randles equivalent circuit

It combines four major components, namely the electrolyte resistance between working and reference electrodes ( $R_s$ ), the double-layer capacitance ( $C_{dl}$ ), charge-transfer resistance ( $R_{et}$ ) and the Warburg Impedance ( $Z_w$ ). All these components can be identified by studying the variation in impedance of an electrochemical cell over a wide frequency range (normally 100 kHz–1 Hz). A common way of showing the resulting data is the complex plane or Nyquist Plot (Fig. 1.15a), in which the real ( $Z'$ ) versus the imaginary



( $-Z''$ ) components of the impedance are plotted. In this plot, two separate processes are very well differentiated. The semicircle depicts a charge-transfer-controlled process, the intercept of which with the X axis gives  $R_s$  and  $R_{ct}$  values and a straight line with a slope of 1 due to  $Z_w$ , whose extrapolation to the X axis allows calculation of the Warburg coefficient ( $\sigma$ ), from which the diffusion coefficients of the electroactive species can be estimated. From the frequency at the top of the semicircle in the Nyquist Plot, where the value of  $-Z''$  is maximum, the time-relaxation constant ( $\tau$ ) for the Faradaic process can also be calculated. Another way of presenting impedance data is the Bode Plot, in which the logarithm of the absolute value of  $Z$  and the phase ( $\phi$ ) are plotted against the logarithm of frequency ( $f$ ). Fig. 1.15(b) shows the Bode Plots for the Randles circuit. Unlike the Nyquist Plots, these data presentations give direct information about  $f$  and  $\phi$  that help ascertain the different constituent phases of the system more easily. Thus, in those frequency regions where a resistive behavior is dominant, a horizontal line is observed for the  $\log Z$ - $\log f$  representation and  $\phi$  value close to  $0^\circ$  is obtained. Also, capacitive behavior within a frequency region is described by a straight line with a slope of -1 in the  $\log Z$ - $\log f$  plots and a  $\phi$  value around  $90^\circ$ , whereas diffusion-controlled phenomena (Warburg Impedance) would give a straight line with a slope of -1/2 and a  $\phi$  value of  $45^\circ$ . A detailed mathematical description of all the above parameters can be found elsewhere [132, 133]. Impedance behavior described by Nyquist Plots with more than one semicircle or Bode Plots exhibiting different capacitive/resistive regions may describe electrochemical systems with several phases and/or more complicated Faradaic

processes (i.e., coating formation/ deterioration or adsorption phenomena on the transducer as well as coupled chemical reactions).

In the present work the electrochemical impedance measurements have been carried out using a conventional three-electrode cell configuration consisting of a working electrode, Ag/AgCl reference electrode and a platinum wire mesh as a counter electrode. The impedance measurements were taken in an electrolytic solution containing phosphate buffer saline (PBS; pH 7.4, 0.1 M KCl) having a mixture of 2 mM  $K_3[Fe(CN)_6]$  and 2 mM  $K_4[Fe(CN)_6]$ . The experimental data so obtained after each stage of surface modification of the working electrode has been circuit fitted by GPES (General purpose electrochemical system version 4.9, Eco Chemie, The Netherlands) software and the corresponding values of EIS parameters were obtained which were utilized in this work for characterizing the nanomaterials modified electrode surface and the charge transfer process occurring at the bioelectrode surface.

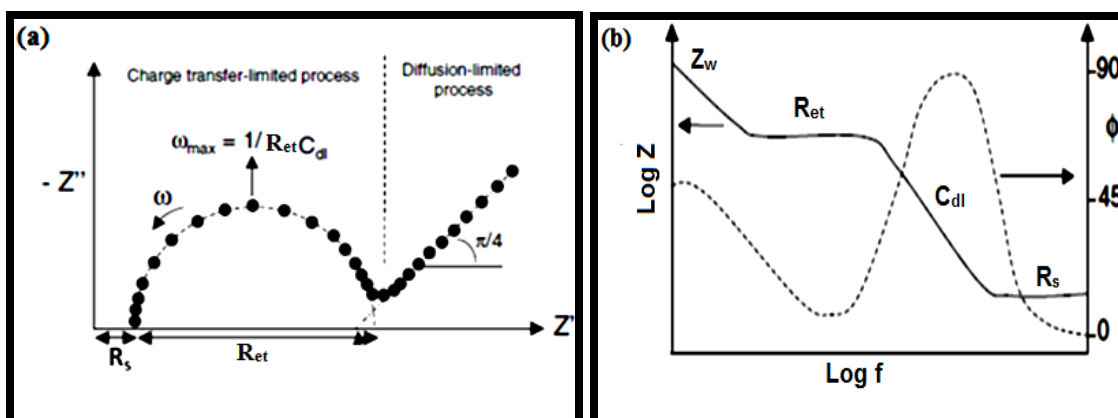


**Fig. 1.15:** (a) Nyquist plot; (b) Bode plot

## 1.13 References

1. L.C. Clark and C. Lyons, *Ann. N. Y. Acad. Sci.* 102 (1962) 29.
2. C. Chen, Q. Xie, D. Yang, H. Xiao, Y. Fu, Y. Tana and S. Yao, *RSC Adv.* 3 (2013) 4473.
3. A.D. McNaught and A. Wilkinson, "IUPAC Compendium of Chemical Terminology", 2nd ed. Blackwell Scientific Publications, Oxford, 1997.
4. "Biosensors Market - Global Industry Analysis, Size, Share, Growth, Trends and Forecast, 2012–2018", <http://www.transparencymarketresearch.com/biosensors-market.html>.
5. Y. Tian, M. Cuneo, A. Changela, B. Höcker, L. Beese and H. Hellinga, *Protein Science* 16 (2007) 2240.
6. J. Metzger, P. Landenberg, M. Kehrel, A. Buhl, K. Lackner and P. Lupp, *Clin. Chem.* 53 (2007) 1137.
7. J. Xu, D. Suarez and D. Gottfried, *Anal Bioanal Chem.* 389 (2007) 1193.
8. M. Velasco-Garcia and T. Mottram, *Biosystems Engineering* 84 (2003) 1.
9. L. Terry, S. White and L. Tigwell, *J Agric Food Chem.* 53 (2005) 1309.
10. S. Rodriguez, M. Lopez and D. Barceló, *Anal Bioanal Chem.* 386 (2006) 1025.
11. K. Donaldson, M. Kramer and D. Lim, *Biosens. Bioelectron.* 20 (2004) 322.
12. S. Ohlson, M. Strandh and H. Nilshans, *J. Mol. Recognit.* 10 (1997) 135.
13. D. Wang and Y. Tan, *Electrochim. Acta* 116 (2014) 495.
14. N. J. Ronkainen-Matsuno, J. H. Thomas, H. B. Halsall and W. R. Heineman, *TrAC, Trends Anal. Chem.* 21 (2002) 213.

15. R. A. Copeland, "Enzymes" John Wiley & Sons VCH, New York, NY, USA, 2000.
16. C. Cheng, Y. Peng, J. Bai, X. Zhang, Y. Liu, X. Fan, B. Ning and Z. Gao, *Sens. Actuators, B* 190 (2014) 900.
17. W. Jin, G. Yang, H. Shao and A. Qin, *Food Control* 39 (2014) 185.
18. J. Wang, D. Chen, Y. Xu and W. Liu, *Sens. Actuators, B* 190 (2014) 378.
19. M. Giannetto, E. Umiltà, M. Careri, *Anal. Chim. Acta* 806 (2014)197.
20. S. Ge, M. Sun, W. Liu, S. Li, X. Wang, C. Chu, M. Yan and J. Yu, *Sens. Actuators, B* 192 (2014) 317.
21. X. Wang, J. Dong, X. Liu, Y. Liu and S. Ai, *Biosens. Bioelectron.* 54 (2014) 85.
22. D. R.P. Morris, J. Fatisson, A. L.J. Olsson, N. Tufenkji and A. R. Ferro, *Sens. Actuators, B* 190 (2014) 851-857
23. A. C. Chan, D. Ager and I. P. Thompson, *J. Microbiol. Methods* 93 (2013)209.
24. A. Bentley, A. Atkinson, J. Jezek and D.M Rawson, *Toxicol In Vitro* 15 (2001) 469.
25. E. Paleček and M. Bartošik, *Chem. Rev.* 112 (2012) 3427.
26. M. Vaničkova, J. Lehotay, J. Čížmarikova and J. Labuda, *Bioelectrochemistry* 66 (2005) 125.
27. M. Bučkova, J. Labuda, J. Šandula, L. Križkova, I. Štepanek and Z. Duračkova, *Talanta* 56 (2002) 939.
28. J. Galandova, R. Ovadekova, A. Ferancova and J. Labuda, *Anal. Bioanal. Chem.* 394 (2009) 855.
29. A. Ferancova, M. Buckova, E. Korgova, O. Korbut, P. Grundler, I. Warnmark, R. Stepan, J. Barek, J. Zima, and J Labuda, *Bioelectrochemistry* 67 (2005) 191.

- 
30. A. K.H. Cheng, D. Sen and Hua-Zhong Yu, *Bioelectrochemistry* 77 (2009) 1.
  31. S. Song, L. Wang, J. Li, C. Fan and J. Zhao. *TrAC, Trends Anal. Chem* 27 (2008) 108.
  32. B. R. Eggins, “Chemical Sensors and Biosensors”, John Wiley & Sons, West Sussex, England, 2002.
  33. J. Wang, “Analytical Electrochemistry”, John Wiley & Sons VCH, Hoboken, New Jersey, USA, 2006.
  34. J. Wang, *Chem. Rev.* 108 (2008) 814.
  35. J. Wang, M. Musameh, *Analyst* 129 (2004), 1.
  36. K. Wojciechowski, M. Kucharek, W. Wróblewski, P. Warszynski, *J. Electroanal. Chem.* 638 (2010) 204.
  37. W. Ngeontae, W. Janrungratsakul, P. Maneewattanapinyo, S. Ekgasit, W. Aeungmaitrepirom, T. Tuntulani, *Sens. Actuators, B* 137 (2009) 320.
  38. S.M. Usman Ali, O. Nur, M. Willander, B. Danielsson, *IEEE Trans. Nanotechnol.* 8 (2009) 678.
  39. A. Poghossian, *Sens. Actuators, B* 44 (1997) 361.
  40. X.L. Luo, J.J. Xu, W. Zhao, H.Y. Chen, *Sens. Actuators, B* 97 (2004) 249.
  41. A. Seki, S. Ikeda, I. Kubo, I. Karube, *Anal. Chim. Acta* 373 (1998) 9.
  42. G. Davis, *Biosensors* 1 (1985) 161.
  43. M. N. Sonuç and M. K. Sezgintürk, *Talanta* 120 (2014) 355.
  44. R. Elshafey, A. C. Tavares, M. Siaj and M. Zourob, *Biosens. Bioelectron.* 50 (2013) 143.

- 
45. Hai-Bo Wang, Hong-Ding Zhang, Shu-Ping Xu, T. Gan, Ke-Jing Huang and Yan-Ming Liu, *Sens. Actuators, B*, 194 (2014) 478.
  46. T. Yang, S. Wang, H. Jin, W. Bao, S. Huang and J. Wang, *Sens. Actuators, B* 178 (2013) 310.
  47. N. S. Ferreira and M. G. F. Sales, *Biosens. Bioelectron.* 53 (2014) 193.
  48. M. Schaeferling, S. Schiller, H. Paul, M. Kruschina, P. Pavlickova, M. Meerkamp, C. Giammasi and D. Kambhampati, *Electrophoresis* 23 (2002) 3097.
  49. T. Hang and A. Guiseppi-Ellie, *Biosens. Bioelectron.* 19 (2004) 1537.
  50. I.O. K'Owino, and O.A. Sadik, *Electroanalysis* 17 (2005) 2101.
  51. S. Lepinay, A. Staff, A. Ianoul and J. Albert, *Biosens. Bioelectron.* 52 (2014) 337.
  52. María-José Bañuls, R. Puchades and Á. Maquieira, *Anal. Chim. Acta* 777 (2013) 1.
  53. X.D. Hoa, A.G. Kirk and M. Tabrizian, *Biosens. Bioelectron.* 23 (2007) 151.
  54. J. Ngeh-Ngwainbi, A. A. Suleiman and G. G. Guilbault, *Biosens. Bioelectron.* 5 (1990) 13.
  55. R. L. Bunde, E. J. Jarvi and J. J. Rosentreter, *Talanta* 46 (1998) 1223.
  56. A. Nábauer, P. Berg, I. Ruge, E. Müller, P. Woias, C. Kösslinger and H. Drobe *Sens. Actuators, B* 1(1990) 508.
  57. S.P. Mohanty and E. Kougiannos, *Potentials* 25 (2006) 35.
  58. M.L. Antonelli, C. Spadaro and R.F. Tornelli, *Talanta* 74 (2008)1450.
  59. S.G. Bhand, S. Soundararajan, I. Surugiu-Warnmark, J.S. Milea, E.S. Dey, M. Yakovleva and B. Danielsson, *Anal.Chim. Acta.* 668 (2010) 13.
  60. R. Ramanathan and B. Danielsson, *Biosens. Bioelectron.* 16 (2001) 417.
-

- 
61. S. Vermeir, B.M. Nicolai, P. Verboven, P. Van Gerwen, B. Baeten, L. Hoflack, V. Vulsteke and J. Lammertyn, *Anal. Chem.* 79 (2007) 6119.
  62. C. L. Choi and A. P. Alivisatos, *Annu. Rev. Phys. Chem.* 61 (2010) 369.
  63. D. V. Talapin, J.-S. Lee, M. V. Kovalenko and E. V. Shevchenko, *Chem. Rev.* 110 (2010) 389.
  64. J.Q. Liu, A. Chou, W. Rahmat, M.N. Paddon-Row and J.J. Gooding, *Electroanalysis* 17 (2005) 38.
  65. F. Patolsky, Y. Weizmann and I. Willner, *Angew. Chem. Int. Ed.* 43 (2004) 2113.
  66. M. Musameh, J. Wang, A. Merkoci and Y.H. Lin, *Electrochem. Commun.* 4 (2002) 743.
  67. M. Dequaire, , C. Degrand, and B. Limoges, *Anal. Chem.* 72 (2000) 5521.
  68. M. Pumera, S. Sanchez, I. Ichinose and J. Tang, *Sens. Actuators, B* 123 (2007) 1195.
  69. Y.H. Xiao and C.M. Li, *Electroanalysis* 20 (2008) 648.
  70. L. Agui, P. Yanez-Sedeno and J.M. Pingarron, *Anal. Chim. Acta* 622 (2008) 11.
  71. S.A. Kumar and S.M. Chen, *Anal. Lett.* 41 (2008) 141.
  72. S. Sirivisoot and T.J. Webster, *Nanotechnology* 19 (2008) 1.
  73. E. Katz and I. Willner, *Chem phys chem* 5 (2004) 1085.
  74. A. Merkoci, M. Aldavert, S. Marin, and S. Alegret, *TrAC Trends Anal. Chem.* 24 (2005) 341.
  75. J.M. Pingarron, P. Yanez-Sedeno, A. Gonzalez-Cortes, *Electrochim. Acta* 53 (2008) 5848.
  76. Z. Nie, A. Petukhova and E. Kumacheva, *Nat. Nanotechnol.* 5 (2010) 15.
-

- 
77. A. N. Shipway, E. Katz and I. Willner, *Chem Phys Chem* 1 (2000) 18.
78. Y. N. Xia, B. Gates, Y. D. Yin and Y. Lu, *Adv. Mater.* 12 (2000) 693.
79. D.H. Bamford, *Curr Biol.* 10 (2000) R558.
80. G.M. Whitesides, *Small* 1 (2005) 172.
81. N. Herron and D. L. Thorn, *Adv. Mater.* 10 (1998) 1173.
82. H. Shirakawa, E. J. Louis, A. G. MacDiarmid, C. K. Chiang and A. J. Heeger, *J. Chem. Soc., Chem. Commun.* 578 (1977) 578.
83. J. Heinze, *Top. Curr. Chem.* 152 (1990) 2.
84. H. S. Nalwa, "Handbook of Organic Conductive Molecules and Polymers", John Wiley & Sons, New York, 1997.
85. T. A. Skotheim, R. L. Elsenbaumer and J. R. Reynolds, "Handbook of Conducting Polymers", 2nd Edn. ed., Marcel Dekker, New York, 1998.
86. M. E. G. Lyons, "Advances in Chemical Physics, Polymeric Systems", ed. I. Prigogine and S. A. Rice, John Wiley & Sons, New York, 94 (1997) 297.
87. J. Simonet and J. R. Berthelot, *Prog. Solid State Chem.* 21 (1991) 1.
88. Y. Zhao, S. Si, L. Wang, C. Liao, P. Tang and H. Cao, *J. Power Sources* 248 (2014), 962.
89. S. S. Shinde, G. S. Gund, D. P. Dubal, S. B. Jambure and C. D. Lokhande, *Electrochim. Acta* 119 (2014) 1.
90. Y. Xie and Y. Zhao, *Mater. Sci. Eng., C* 33 (2013) 5028.
91. S.T. Navale, A.T. Mane, M.A. Chougule, R.D. Sakhare, S.R. Nalage and V.B. Patil, *Synth. Met.* 189 (2014) 94.
-



- 
92. M. Sookhakian, Y.M. Amin, S. Baradaran, M.T. Tajabadi, A. Moradi Golsheikh and W.J. Basirun, *Thin Solid Films* 552 (2014) 204.
  93. C. Merlini, R. S. Almeida, M. A. D'Ávila, W. H. Schreiner and G. M. O. Barra *Mater. Sci. Eng., B* 179 (2014) 52.
  94. M. Sharma, G. I.N. Waterhouse, S. W.C. Loader, S. Garg and D. Svirskis, *Int. J. Pharm.* 443 (2013)163.
  95. Y.H. Xiao and C.M. Li, *Electroanalysis* 20 (2008) 648.
  96. S. Allender, P. Scharbotough, V. Peto, M. Rayner, J. Leal and R. Luengo-Fernández. "European cardiovascular disease statistics", 2008 edition.
  97. "Facts about cardiovascular diseases", [http://www.who.int/mediacentre /factsheets /fs317/en/index.html](http://www.who.int/mediacentre/factsheets/fs317/en/index.html), World Health Organization, 2007.
  98. J.S. Ladue, F. Wroblewski and A. Karmen, *Science* 120 (1954) 497.
  99. S. Vittorini and A. Clerico, *Clin Chem Lab Med* 46 (2008) 748.
  100. C. Montague and T. Kircher, *Am. J. Clin. Pathol.* 4 (1995) 472.
  101. M. Singh-Zocchi, J. Hanne and G. Zocchi, *Biophys. J.* 83 (2002) 2211.
  102. N.S.K. Gunda and S.K. Mitra, *Biomicrofluidics* 4 (2010) 014105.
  103. M. Plebani and M. Zaninotto, *Clin Chim Acta* 272 (1998) 69.
  104. S. S. Wong, *Ann Clin Lab Sci* 12 (1996) 301.
  105. T. M. O'Regan, L. J. O'Riordan, M. Pravda, C. K. O'Sullivan and G. G. Guilbault, *Anal. Chim. Acta* 460 (2002) 141.
  106. S. E. Phillips, *J Mol Biol.* 142 (1980) 531.
  107. A.A. Mohammed and J.L. Januzzi Jr., *Cardiol. Rev.* 18 (2010)12.
-

- 
108. F.S. Apple, A. H. B. Wu and A.S. Jaffe, *Am. Heart J.* 144 (2002) 981.
  109. W. Shen, D.Y. Tian, H. Cui, D. Yang and Z.P. Bian, *Biosens. Bioelectron.* 27 (2011) 18.
  110. G. Boriani, M. Biffi, V. Cervi, G. Bronzetti, G. Magagnoli, R. Zannoli and A. Branzi, *Chest* 118 (2000) 342.
  111. F.S. Apple, A.J. Maturen, R.E. Mullins, P.C. Painter, M.S. Pessin-Minsley, R.A. Webster, J.S. Flores, R. DeCresce, D.J. Fink, P.M. Buckley, J. Marsh, V. Ricchiuti and R.H. Christenson, *Clin. Chem.* 45 (1999) 206.
  112. Z. Yang and D.M. Zhou, *Clin. Biochem.* 39 (2006) 771.
  113. S.F. Melanson, D.A. Morrow and P. Jarolim, *Am J Clin Path*, 128 (2007) 282.
  114. M. V. Vinogradova, D. B. Stone, G. G. Malanina, C. Karatzaferi, R. Cooke, R. A. Mendelson and R. J. Fletterick, *Proc Natl Acad Sci USA* 102 (2005) 5038.
  115. H.C. Ablij and A. E. Meinders, *Eur J Intern Med* 13 (2002) 412.
  116. D Thompson, M.B. Pepys and S.P. Wood, *Structure* 7 (1999) 169.
  117. M.B. Pepys and G.M. Hirschfiel, *J Clin Invest*, 101(2003) 1805.
  118. E.B. Oliveira, E.C. Gotschlich and T.Y. Liu, *Proc Natl Acad Sci USA* 74 (1977) 3148.
  119. Y.N. Yang, H.I. Lin, J.H. Wang, S. C. Shiesh and G.B. Lee, *Biosens. Bioelectron.* 24 (2009) 3091.
  120. A. K. Shrive, G. M. T. Cheetham, D. Holden, D. A. Myles, W. G. Turnell, J. E. Volanakis, M. B. Pepys, A. C. Bloomer and T. J. Greenhough, *Nat Struct Biol* 3 (1996) 346.

121. D.F. Shriver, P.W. Atkins and C.H. Langford, "Inorganic Chemistry", second Edition. Oxford University press, Oxford, United Kingdom 1994.
122. P.B. Coleman, "Practical Sampling Techniques for: Infrared Analysis", CRC Press 1993.
123. B. C. Smith, "Fundamentals of Fourier Transform infrared spectroscopy", CRS Press, 1996.
124. D.M. Livingston, "The master of light: A biography of Albert Abraham Michelson", The University Press of Chicago, 1973.
125. J. Randles, *Trans. Far. Soc.* 44 (1948) 327.
126. E. Gileadi, E. Kirowa-Eisner and J. Penciner, "Interfacial Chemistry: An Experimental Approach", Addison-Wesley, U.S.A, 1975.
127. A. J. Bard and L. R. Faulkner, "Electrochemical Methods, Fundamentals and Applications", John Wiley and Sons, New York, 1980.
128. C. M. A. Brett and A. M. O. Brett, "Electrochemistry: Principles Methods and Applications", Oxford University Press, 1993.
129. J. Bockris and S.U.M. Khan, "Surface Electrochemistry: A Molecular Level Approach", Plenum Press New York and London, 1993.
130. R. Parsons, *Surf. Sci.* 90 (1990) 813.
131. M. Faraday, *Phil Trans. Roy. Soc., A.* 124 (1834) 77.
132. C.M. Brett and A.M.O. Brett, "Electrochemistry: Principles, Methods, and Applications", Oxford University Press New York USA, 1993.

133. S. Krause, Impedance methods, In “Encyclopedia of Electrochemistry; A.J. Bard, M. Stratmann, P.R. Unwin (Eds.)”, vol. 3, Wiley-VCH, Weinheim, Germany, 2003.

## CHAPTER 2

---

### Protein functionalized ZnS(MPA)-PPy nanocomposite film based bioelectrode

---

*In this chapter an electrochemically synthesized ZnS nanoparticles modified polypyrrole (PPy) nanocomposite film based immunosensor for the detection of C-reactive protein ( $\alpha$ CRP) is reported. The ZnS-PPy composite film was characterized by TEM, AFM and electrochemical techniques. The modified film showed good biocompatibility with efficient binding to protein antibody (Ab- $\alpha$ CRP) molecules through ZnS nanoparticles exhibiting an attractive platform for immunosensor fabrication. The electrical and sensing properties of the polymer composite film of different thickness towards protein antigen (Ag- $\alpha$ CRP) were delineated. The immunosensor exhibited an impedance response towards different concentrations of Ag- $\alpha$ CRP, in a linear range from 10 ng mL<sup>-1</sup> to 10  $\mu$ g mL<sup>-1</sup>.*

## 2.1 Introduction

Colloidal nanoparticles, often referred to as quantum dots, have attracted extensive scientific and industrial interests as a consequence of their strong size-dependent properties and unique optical and electronic features,[1–3] which give rise to their potential use in biological labels [4,5]. Recently, ZnS nanoparticles decorated single walled carbon nanotubes have been used as chemiresistive label free DNA sensor [6]. However, demonstrations of their targeted usage towards the detection of cardiac markers are limited. The conducting polymers have been considered useful for immunosensing applications, due to their high chemical stability, compatibility with immunoactive entities, and facility to be doped with nanoparticles [7]. PPy is an intrinsically conducting polymer with various interesting properties [8]. Its synthesis, characterization, and applications have received a lot of attention in publication over the past two decades. The insolubility of PPy in most common solvents and adherence of PPy to the electrode surface during sensor preparation via chemical method is problematic. These disadvantages however may be avoided, if electrochemical polymerization is applied. The thickness and morphology of the polymer film can easily be controlled by the type of solvent, electrolyte concentration, type of electrode material, current density, applied potential, polymerization time and temperature [9]. As a result of its good intrinsic properties, PPy has proven promising for several applications including batteries, supercapacitors, electrochemical biosensors, conductive textiles and fabrics, mechanical actuators, electromagnetic interference shielding, anti-static coatings and drug delivery systems [10]. Due to its favorable biocompatibility, PPy is often chosen for biological

applications as an ideal electroactive polymer and has been applied to form sensors including protein [11] and DNA biosensors [12]. The organic/inorganic hybrid materials (PPy and ZnS in this case) with biomolecules stimulate growing interests in the research areas of biotechnology and nanotechnology due to their unique properties derived from the combinatorial effects of the individual phases [13].

Cardiac biomarkers are the molecules that are released in the blood when there is some damage to the heart. C-reactive protein (CRP) is classified as a characteristic acute phase reactant in human serum and a classic marker of inflammation [14-16]. The basic biochemical reaction that constitutes blood CRP detection is the selective association of the protein with a specific analyte. The majority of analytical methodologies use immunoassays techniques, based on an antigen-antibody approach. Enzyme Linked Immuno Sorbent Assay (ELISA) is the most commonly used technique, which shows a higher sensitivity and allows the quantification of CRP in blood. In clinical procedures/protocols, the most used technique to obtain a fast analysis of CRP is based on kit tests, due to easy assay availability, biochemical stability, and can obtain international standards and inter-assay precision, but limited to elevated concentrations of CRP. Other techniques, using a wide variety of nanoparticles with different detection systems, selective ligands such as phosphocholine or o-phosphorylethanolamine and emerging techniques based on the formation of plasmon and synthetic receptors by means of molecular imprinted polymer techniques are shown in Fig. 2.1 [17, 18]. But these methods are complicate multistage processes, tedious, and time consuming. Recently, some other methods for CRP quantification including those based on piezoelectric

microcantilevers [19], quartz crystal microbalance technology [20] and microfluidics [21] have been developed during the past few years.

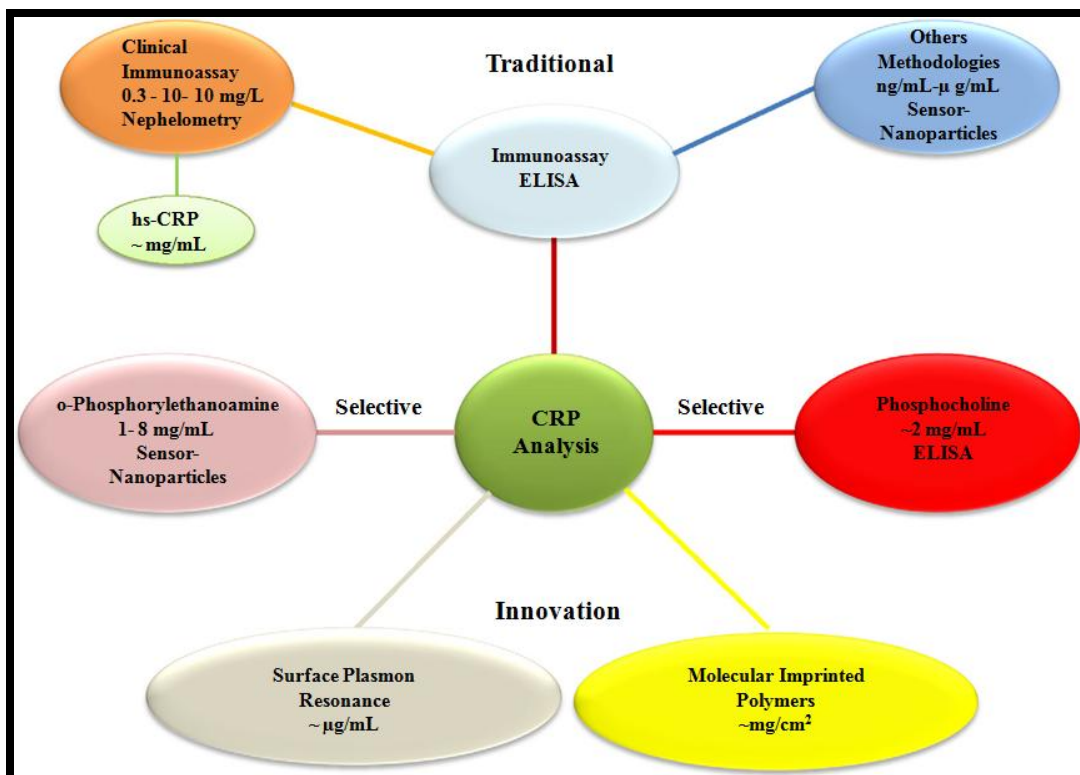


**Fig. 2.1:** Current analytical techniques used to quantify CRP samples. [17]

EIS has been used to study a variety of electrochemical phenomena due to their low cost, small instrument size, and speed of analysis. Electrochemical immunosensor, an analytical device for the measurement of antibody or antigen concentrations, is based on bio-specific recognition interactions and is one of the major analytical tools used in clinical diagnostics, food safety and quality control, biological analysis and environmental monitoring. EIS measures the response (current and its phase) of an electrochemical system to an applied oscillating potential as a function of the frequency.



As one of the electrochemical technologies, EIS is a rapidly developing electrochemical technique for the investigation of bulk and interfacial electrical properties of any kind of solid or liquid material which is connected to, or part of, an appropriate electrochemical transducer. EIS is a powerful technique for examining many chemical and physical processes in solutions as well as solids. For solution phase electrochemistry a complex sequence of coupled processes such as, electron transfer, mass transport and chemical reaction can all control or influence the output from an electrochemical measurement. Impedance measurements are divided into two categories namely non-Faradic and Faradic impedance. EIS is a Faradic impedance technique and it is performed in the presence of a redox probe, whereas the non-Faradic impedance is conducted in the absence of any redox probe. This technique is regarded as an effective tool for sensing the formation of antigen–antibody interaction, biotin–avidin complexes and oligonucleotides–DNA interaction on the electrode surface by probing the features of the interfacial properties.

Here, we present a simple and direct one step procedure for the electrochemical synthesis of 3-Mercaptopropionic acid (MPA) capped ZnS modified PPy nanocomposite film on to the surface of Indium tin oxide (ITO) coated glass plate. The small-sized ZnS nanoparticles with free carboxyl groups from MPA on its surface provided large number of binding sites for the covalent immobilization of protein antibody on the polymer nanocomposite film, making this an excellent choice as transducer material, for the design of electrochemical impedimetric immunosensor. In this work, the electrical and sensing properties of ZnS(MPA)-PPy nanocomposite film based bioelectrode were

systematically investigated for Ag- $\alpha$ CRP detection in PBS solution using impedance measurements.

## 2.2 Experimental

### 2.2.1 Reagents

Ab- $\alpha$ CRP (Cat 4C28 mAbC2) and Ag- $\alpha$ CRP (Cat 8C72) were obtained from Hytest (Turku, Finland). Zinc Nitrate hexahydrate ( $\text{Zn}(\text{NO}_3)_2 \cdot 6\text{H}_2\text{O}$ ), sodium sulfide nonahydrate ( $\text{Na}_2\text{S} \cdot 9\text{H}_2\text{O}$ ), Pyrrole (Py), Para toluene sulphonic acid (pTSA), 3-Mercaptopropionic acid 99% (MPA), N-(3-Dimethylaminopropyl)-N'-ethyl carbodiimide hydrochloride (EDC) and N-Hydroxy Succinimide 98% (NHS) were obtained from Sigma-Aldrich chemicals. Pyrrole monomer was distilled thrice and other chemicals were of analytical grade and used without further purification. Water used in all reactions was double de-ionized (DI) water obtained from a Millipore purification system having resistivity of 18.2 M $\Omega$  cm at 25 °C.

### 2.2.2 Equipments

FTIR spectra of the films were taken on a Nicolet 5700 FTIR spectrometer. TEM images were taken on a TEM model Technai G2F30 S Twin, The Netherlands. XRD pattern were recorded using a Bruker AXS Advance D8 powder X-ray diffractometer. AFM images were obtained on a VEECO/DICP2, USA scanning probe microscope. Cyclic voltammetry and EIS measurements were done on a PGSTAT302N, AUTOLAB instrument from Eco Chemie, The Netherlands. All measurements were carried out in a conventional three-electrode cell configuration consisting of the proposed modified

electrode as working electrode, Ag/AgCl as reference electrode and a platinum wire as counter electrode. The electrochemical impedance spectroscopy was conducted in a PBS (pH 7.4, 0.1 M KCl) solution containing 2 mM  $[\text{Fe}(\text{CN})_6]^{3-}/[\text{Fe}(\text{CN})_6]^{4-}$ , in the frequency range from 1 Hz to 100 KHz at an AC voltage of 0.05 V.

### *2.2.3 Synthesis of ZnS(MPA) nanoparticles*

The aqueous ZnS(MPA) nanoparticles were synthesized, at room temperature, by a method as reported earlier [22]. Briefly, appropriate amounts of  $\text{Zn}(\text{NO}_3)_2$ ,  $\text{Na}_2\text{S}$  and MPA were dissolved separately in deionized (DI) water. 4 mL of 0.37 M  $\text{Zn}(\text{NO}_3)_2$  was dropped slowly into 36 mL of 0.16 M MPA solution under continuous stirring. The pH of the mixture was adjusted to 8 by using ammonium hydroxide ( $\text{NH}_4\text{OH}$ ) and then 4 mL of 0.39 M  $\text{Na}_2\text{S}$  was rapidly added to it with vigorous stirring. The colloidal solution so formed was left for 5 min for the reaction to be complete. The above procedure was carried under continuous  $\text{N}_2$  bubbling.

### *2.2.4 Preparation of the bioelectrode*

For the preparation of ZnS(MPA)-PPy nanocomposite film, the ITO coated glass plates ( $10\Omega/\square$ ) were first cleaned by sequential ultrasonic cleaning in soap solution, acetone, ethanol, isopropyl alcohol and DI for 10 min each and dried in vacuum. The ZnS(MPA) modified PPy films of various thickness were electrochemically prepared on ITO glass plates ( $0.5 \times 0.5 \text{ cm}^2$ ) in an aqueous solution containing 0.025 M pyrrole, 0.025 M pTSA, and 0.01M ZnS(MPA), at a fixed current density of  $1 \text{ mA cm}^{-2}$  by injecting charge densities of  $250 \text{ mC cm}^{-2}$  and  $1000 \text{ mC cm}^{-2}$ , respectively. By using Taylor- Hobson

Talystep profilometer, the thickness of the films so obtained was found to be  $95\pm 5$  nm and  $200\pm 10$  nm, for the injecting charge density of 250 and  $1000\text{ mC cm}^{-2}$ , respectively. The free carboxyl groups present on ZnS(MPA) nanoparticles have been utilized for the covalent attachment of antibodies, Ab- $\alpha$ CRP, through peptide linkage using the linkage reagents EDC and NHS where EDC and NHS worked as a coupling agent and an activator, respectively. In brief, for the bioelectrode formation, ZnS(MPA)-PPy/ITO-glass plate was first incubated in a solution mixture of 30 mM NHS and 150 mM EDC for 1 h and then in  $100\text{ }\mu\text{g mL}^{-1}$  Ab- $\alpha$ CRP in PBS (pH 7.4), for an overnight period at a temperature of  $4^\circ\text{C}$ . This was followed by washing off of the unattached protein antibody on the bioelectrode surface with PBS and drying with  $\text{N}_2$  gas flow. Finally, the bioelectrode was incubated in 1.0% (W/V) bovine serum albumin (BSA) solution for 30 min to block the non-specific reactive sites, if available, on the ZnS(MPA) nanoparticles and/or PPy surface, and subsequently rinsed with PBS, dried under  $\text{N}_2$  and stored at  $4^\circ\text{C}$ . The stepwise construction of the prototype bioelectrode assembly is schematically represented in Fig. 2.2.

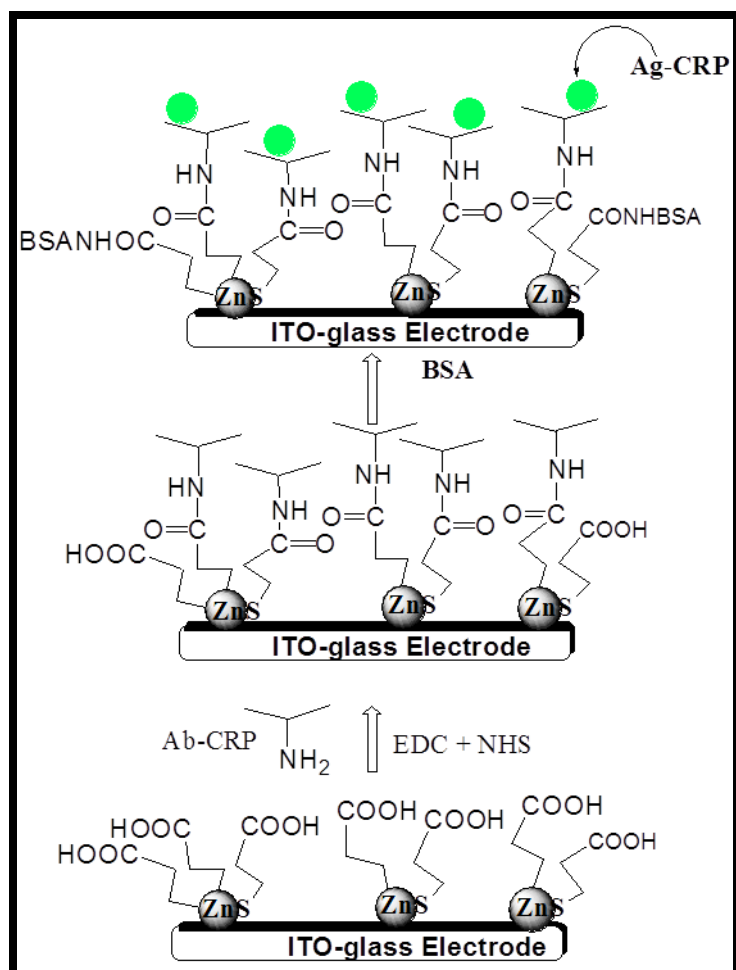


**Fig. 2.2:** Scheme showing the stepwise fabrication of the immunosensor

## 2.3 Results & Discussion

### 2.3.1 Microstructural Characterization

AFM images of pure PPy (Fig. 2.3a) revealed that the PPy film surface consists of a random distribution of globular features (grains or nodules) with average surface roughness ( $R_a$ ) of 8.80 nm. After the incorporation of ZnS(MPA) in PPy film, numerous small particles of ZnS of spherical sizes ranging between 5 and 8 nm (small dots in the

image) with agglomeration at certain places were seen in between the rough globular structure of PPy with  $R_a$  of 9.88 nm (Fig. 2.3b). Upon protein Ab- $\alpha$ CRP immobilization, the composite film shows a completely different morphology with  $R_a$  of 5.78 nm (Fig. 2.3c). This may be attributed to the immobilization of protein molecules resulting in a smooth and featureless image similar to an earlier reported morphology for glucose oxidase immobilized PPy film [23].

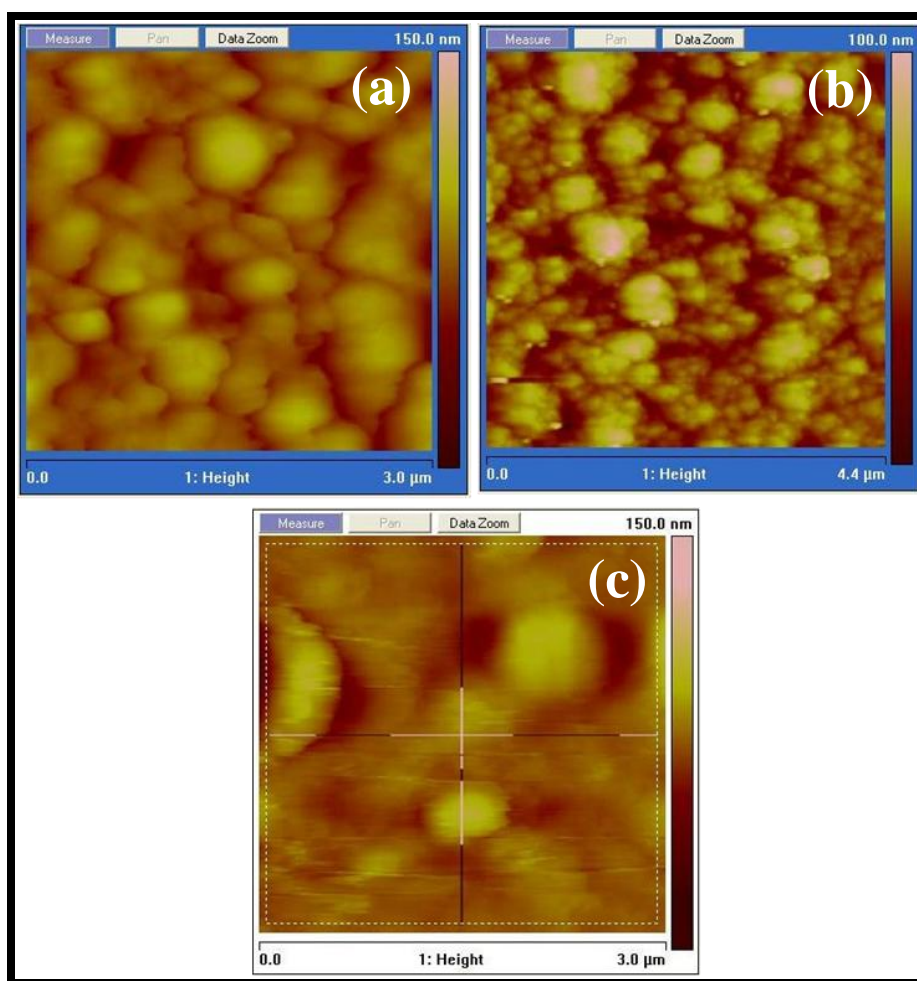


**Fig. 2.3:** AFM images of (a) PPy/ITO-glass, (b) ZnS(MPA)-PPy/ITO-glass and (c) Ab- $\alpha$ CRP/ZnS(MPA)-PPy/ITO-glass.

This was further characterized by TEM images of the ZnS(MPA)-PPy sample prepared on Cu-grid (inset of Fig. 2.4), which depicts a uniform distribution of the ZnS(MPA) nanoparticles of average size 5 nm entrapped inside the PPy film. These are well separated and more or less spherical with clear lattice fringes. D-spacing values indicate that both cubic and orthorhombic ZnS(MPA) nanoparticles were encapsulated. The d-spacing value of 0.25 nm corresponds to PPy (321) orthorhombic lattice plane, while the d-spacing values of 0.30 nm and 0.18 nm correspond to ZnS(111) cubic and ZnS(220) orthorhombic lattice plane, respectively.

Further, XRD pattern shows broad peaks of ZnS(MPA) (Fig. 2.4a) corresponding to small particle size of the ZnS(MPA) nanoparticles, while the sharp peaks in the XRD pattern of ZnS(MPA)-PPy indicate the crystalline nature of the modified PPy film (Fig.2.4c). The XRD pattern of pure PPy film (Fig. 2.4b) shows orthorhombic structure with lattice parameters  $a=10.00 \text{ \AA}$ ,  $b=9.26 \text{ \AA}$ , and  $c=8.40 \text{ \AA}$  and angles  $\alpha=\beta=\gamma=90^\circ$  and a volume of  $778.73 \text{ \AA}^3$ . The XRD spectra of ZnS(MPA)-PPy composite film shows a sharp peak of ZnS (MPA) indicating the encapsulation of ZnS (MPA) nanoparticles inside the PPy film. The calculated lattice parameters for PPy in the ZnS (MPA)-polymer composite film are  $a=13.164 \text{ \AA}$ ,  $b=10.867 \text{ \AA}$ , and  $c=7.167 \text{ \AA}$  with angles  $\alpha=\beta=\gamma=90^\circ$  and a volume of  $1025.15 \text{ \AA}^3$ . A significant increase in the value of lattice parameter b related to interchain spacing and increased volume observed in case of composite film with respect to pristine polymer film indicates a strong interaction between PPy and ZnS(MPA) [24].

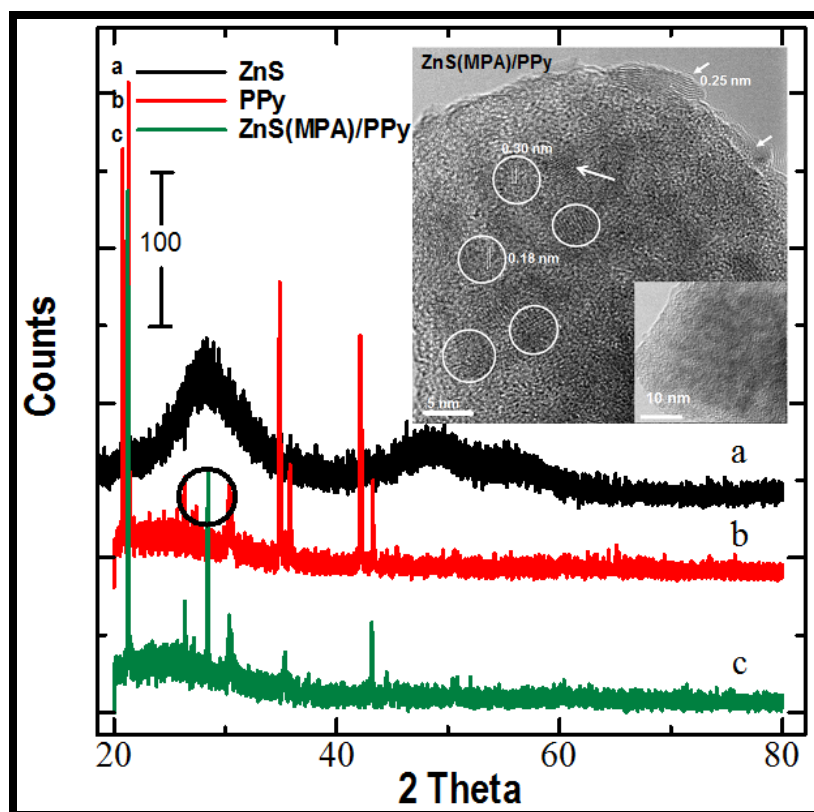


**Fig. 2.4:** XRD pattern of (a) ZnS(MPA), (b) pure PPy and (c) ZnS(MPA)-PPy; Inset: TEM image of ZnS(MPA)-PPy film electrochemically grown on a copper grid.

FTIR spectra of the PPy film and the ZnS-PPy nanocomposite film are shown in Fig. 2.5. The pure PPy film has characteristic peaks of  $890\text{ cm}^{-1}$  (=C-H out-of plane vibration),  $1040\text{ cm}^{-1}$  (=C-H in-plane vibration),  $1170\text{ cm}^{-1}$  (N-C stretch bending), and  $1410\text{ cm}^{-1}$  (pyrrole ring vibration) [25]. A prominent shift in peak positions and significant changes in the peak intensities in the case of the polymer composite with respect to those of pure PPy indicate a change in the PPy backbone structure as modified by ZnS(MPA). The appearance of a new peak at  $1720\text{ cm}^{-1}$  corresponds to a characteristic stretching band of carboxylic groups arising from the encapsulated MPA capped ZnS nanoparticles in polymer composite film.



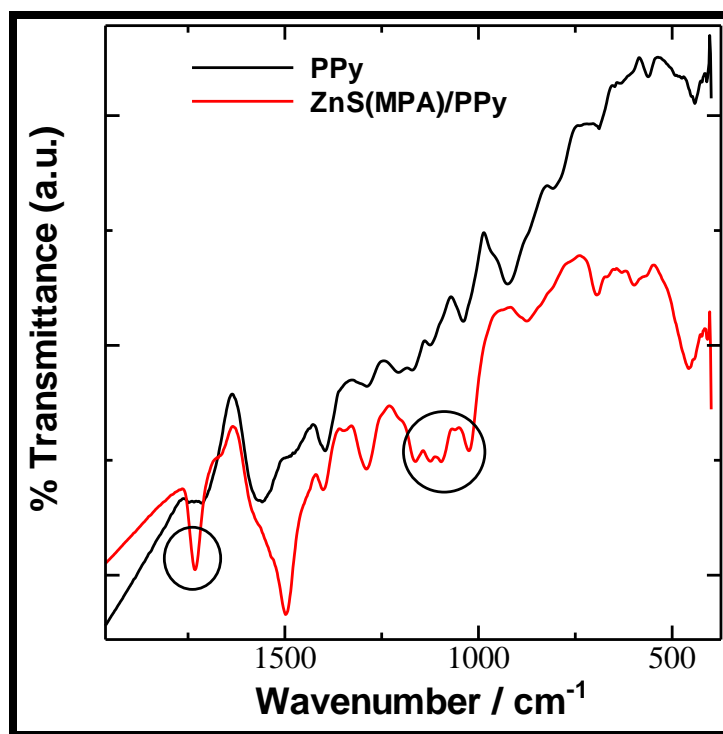


**Fig. 2.5:** FTIR spectra of PPy film and ZnS(MPA)-PPy nanocomposite film

### 2.3.2 Electrochemical characterization of the bioelectrode

The Ab- $\alpha$ CRP/ZnS(MPA)-PPy/ITO-glass plate was also characterized by cyclic voltammetry and EIS. The changes in peak current and separation of peak potentials in cyclic voltammogram, at different electrode surfaces are theoretically related to the electron transfer rate constant i.e. the electron transfer resistance. The  $[\text{Fe}(\text{CN})_6]^{3-/4-}$  probe in PBS buffer (pH=7.4) was used as a marker to investigate the changes in electrode behavior after each surface modification step. The cyclic voltammograms (CV) of the modified electrode before and after the protein antibody immobilization is shown

in Fig. 2.6. In all the CV experiments, 3rd cycle was considered as stable one, since no significant changes were observed in the subsequent cycles.

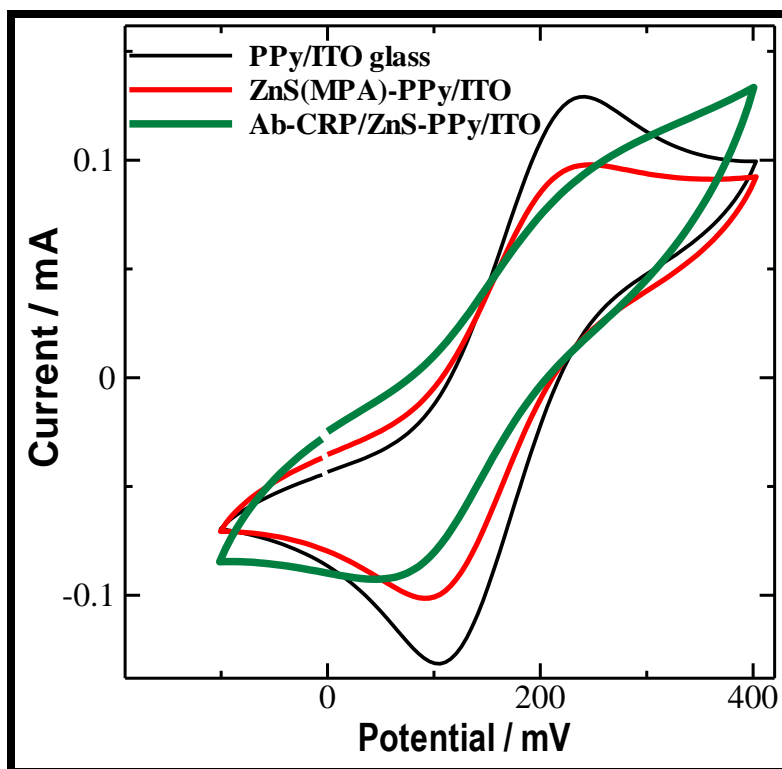


**Fig. 2.6:** Cyclic voltammograms of: PPy/ITO-glass; ZnS(MPA)-PPy/ITO-glass and Ab- $\alpha$ CRP/ZnS(MPA)-PPy/ITO-glass in PBS (pH 7.4) with 0.1 M KCl solution containing 2mM  $[\text{Fe}(\text{CN})_6]^{3-}/[\text{Fe}(\text{CN})_6]^{4-}$ ; scan rate 50 mV/s.

The native PPy/ITO-glass electrode shows a quasi reversible CV with a peak-to-peak separation between the oxidation and reduction potentials ( $\Delta E_p$ ) of 110 mV. This on modification by ZnS(MPA) shows a widening in peak separation  $\Delta E_p$  to 130 mV. This is due to the repulsive interaction of terminal carboxyl ions ( $\text{COO}^-$ ) with ionic probe  $[\text{Fe}(\text{CN})_6]^{3-/4-}$  at the electrode surface/solution interface, conforming the formation of ZnS(MPA)-PPy/ITO-glass electrode. There is a further increment in the separation of

$\Delta E_p$  to 180 mV in the CV curve of protein antibody, Ab- $\alpha$ CRP, immobilized ZnS(MPA)/PPy/ITO-glass bioelectrode. This significant change in the CV curve with increased  $\Delta E_p$  indicates an efficient covalent bonding of protein antibody, Ab- $\alpha$ CRP, with the  $-\text{COOH}$  groups of ZnS(MPA)-PPy/ITO-glass electrode, forming an insulated layer at the electrode surface, which perturbed the interfacial electron transfer considerably.

The electrochemical behavior of the modified electrode was characterized by EIS, using an AC signal of 5mV amplitude, at a formal potential of the redox couple, at a frequency range of 100 kHz to 0.1 Hz. The impedance spectra taken before and after the modification of ITO-glass electrode with different thickness of the polymer composite films prepared at injected charge densities of 250 and 1000  $\text{mC cm}^{-2}$  are shown as Nyquist plots (Fig. 2.7). A typical Nyquist plot showed a semicircle region lying on the axis over a high frequency range, the radius of which corresponds to the charge transfer resistance ( $R_{et}$ ). The impedance result is modeled by an electronic equivalent circuit (inset Fig. 2.7) for the solution resistance,  $R_s$ , the Warburg impedance,  $Z_w$ , resulted from the diffusion of ions in a bulk electrolyte, the double layer capacitance,  $C_{dl}$ , and  $R_{et}$  for the electrochemical reaction. The PPy/ITO glass electrode shows a  $R_{et}$  value of  $48.75\Omega \text{ cm}^2$ . The  $R_{et}$  value for ZnS(MPA)-PPy/ITO-glass electrode was increased to  $86.75 \Omega \text{ cm}^2$ , which indicates a perturbation to electronic transport at the electrode surface interface after the ZnS(MPA) modification of PPy/ITO glass electrode. A further increase in  $R_{et}$  with the immobilization of protein antibody molecules, as evident from (Fig. 2.7) demonstrates an efficient covalent bonding of protein molecules at the electrode surface, which is in accordance with the results (Table 2.1) obtained in CV measurements.

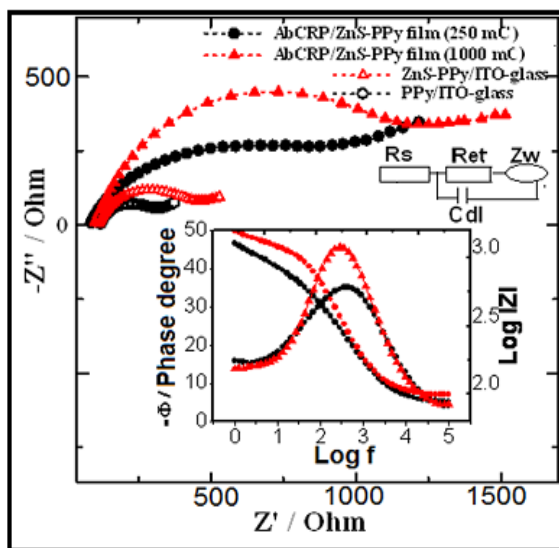


**Fig. 2.7:** Nyquist diagrams for PPy/ITO-glass, ZnS(MPA)-PPy/ITO-glass and Ab- $\alpha$ CRP/ZnS(MPA)-PPy/ITO-glass bioelectrodes with different film thickness prepared at 250 and 1000mC cm<sup>-2</sup> injected charge densities; inset: Bode plots of the corresponding bioelectrodes

**Table 2.1:** Electron charge transfer properties of bare and modified polymer-composite electrodes before and after protein Ag- $\alpha$ CRP immobilization.

Type of Electrode	$\Delta E_p$ (mV)	$R_{et}$ ( $\Omega\text{cm}^2$ )	$C_{dl}$ (F cm <sup>-2</sup> )	$k^0$ (cm s <sup>-1</sup> )	$\tau$ (s)
PPy/ITO-glass	110	48.75	$1.62 \times 10^{-5}$	$10.89 \times 10^{-2}$	$78.97 \times 10^{-5}$
ZnS(MPA)-PPy/ITO	130	86.75	$1.22 \times 10^{-5}$	$6.12 \times 10^{-2}$	$105.92 \times 10^{-5}$
Ab- $\alpha$ CRP/ZnS(MPA)- PPy / ITO (250 mC cm <sup>-2</sup> injected thick film)	180	194.47	$1.11 \times 10^{-5}$	$2.71 \times 10^{-2}$	$216.45 \times 10^{-5}$
Ab- $\alpha$ CRP/ZnS(MPA)- PPy / ITO (1000 mC cm <sup>-2</sup> injected thick film)	220	279.10	$0.8 \times 10^{-5}$	$1.9 \times 10^{-2}$	$223.28 \times 10^{-5}$

The impedance spectra of Ab- $\alpha$ CRP /ZnS(MPA)-PPy/ITO-glass with composite films prepared at 250 and 1000 mC cm<sup>-2</sup> injected charge densities were analyzed to see the effect of the film thickness on electron charge transfer process. The impedance spectra showed an increased value of  $R_{ct}$  from 194.47  $\Omega$  cm<sup>2</sup> to 279.10  $\Omega$  cm<sup>2</sup> for 250 and 1000 mC cm<sup>-2</sup> injected charged thick film electrodes, respectively and were used to obtain the response of heterogeneous charge-transfer kinetics:

$$R_{ct} = RT/nFi^0 \quad (2.1)$$

where the exchange current  $i^0$  is given by Eqn. 2.2

$$i^0 = nFAk^0C \quad (2.2)$$

where  $k^0$  is the electron transfer rate constant between the redox probe and electrode; C is the concentration of the redox probe in the bulk solution; n is the number of electrons involved in the electrode reaction; A is the electrode area; R is a gas constant, T is the temperature and F is the Faraday constant.

The corresponding  $k^0$  of the modified electrodes was calculated by using charge transfer kinetics (Eqn. 2.3):

$$k^0 = RT/n^2F^2A R_{ct} C \quad (2.3)$$

It is worth to be noted that with the increase in the thickness of the polymer composite film prepared at 250 to 1000 mCcm<sup>-2</sup> charge density, the electron transfer rate constant decreases considerably from 2.9 x10<sup>-2</sup> cm s<sup>-1</sup> to 1.92 x10<sup>-2</sup> cm s<sup>-1</sup> respectively, indicating a slow electron charge transfer process on the polymer film surface. This is more evident in the impedance module and shift-phase angle versus frequency Bode plot (inset of Fig.

2.7), wherein the phase angle value of  $45^\circ$  for  $1000 \text{ mC cm}^{-2}$  charge density film demonstrates that the process is controlled by ionic diffusion [26]. Whereas, a significantly low phase angle value of  $35^\circ$  was obtained for  $250 \text{ mC cm}^{-2}$  injected charge density composite film indicating that the process is dominant by interfacial impedance [27]. The time constant of the corresponding charge transfer process was calculated from the maximum frequency value,  $\omega_{\text{max}}$ , in which the semicircle draws a maximum in the imaginary axis by using the Eqn. 2.4:

$$\tau = 1/\omega_{\text{max}} = R_{\text{et}} C_{\text{dl}} \quad (2.4)$$

The results showed an augmented value of time constant for polymer film prepared at  $1000 \text{ mC cm}^{-2}$  charge density in comparison to the film of  $250 \text{ mC cm}^{-2}$  injected charge density. This and sluggish electron transfer rate constant with ionic diffusion process results in the generation of low capacitance at the electrode surface of thick polymer film prepared at  $1000 \text{ mC cm}^{-2}$  charge density.

### 2.3.3 Electrochemical impedance response to protein antigen

Electrochemical impedance response studies of the bioelectrode to protein antigen, Ag- $\alpha$ CRP, was carried out in a 0.1 M KCl solution containing 2mM  $[\text{Fe}(\text{CN})_6]^{3-}/[\text{Fe}(\text{CN})_6]^{4-}$  (pH 7.4), at the scanning frequencies from 1.0 Hz to 10 kHz. The measurement was conducted in a sample solution containing no protein antigen, Ag- $\alpha$ CRP, and the corresponding electron transfer resistance observed in a Nyquist plot was taken as a control sample response. The bioelectrode, as prepared, was tested as an impedance immunosensor with different concentration of protein antigen, Ag- $\alpha$ CRP in aqueous

solution. It was found that with each successive addition of the aliquots of different concentration of Ag- $\alpha$ CRP in a sample solution increases the diameter of Nyquist circle, indicating increased electron-transfer resistance of immunosensor (Fig. 2.8). This is due to the protein antibody-antigen coupling at the immunosensor surface, which acts as a kinetic barrier for the electron transfer [27]. This is more pounced in the Bode diagram, (inset of Fig. 2.8) which shows an increasing trend in both impedance module and phase angle on increasing antibody-antigen coupling at the electrode surface.

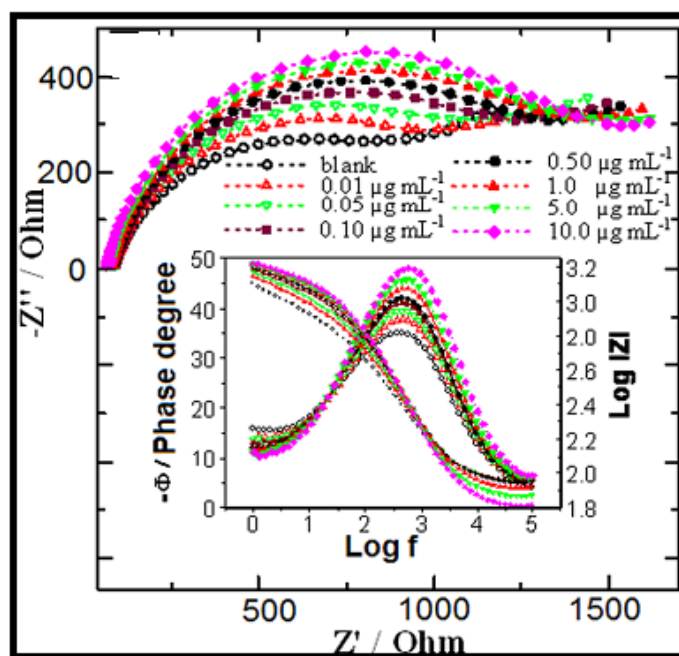


**Fig. 2.8:** Nyquist plot of the bioelectrode prepared at  $250 \text{ mC cm}^{-2}$  injected charge density before and after incubating with different concentrations of Ag- $\alpha$ CRP in PBS (pH 7.4) with  $0.1 \text{ M KCl}$  solution containing  $2 \text{ mM } [\text{Fe}(\text{CN})_6]^{3-/4-}$  inset: Bode plots of the corresponding immunoreaction

Fig. 2.9 shows a linear relationship curve between the electron-transfer resistance and logarithmic value of  $[\text{Ag-}\alpha\text{CRP}]$  in the range of  $10 \text{ ng mL}^{-1}$  to  $10 \text{ }\mu\text{g mL}^{-1}$  with a

correlation coefficient of 0.993 and 0.9998 for immunosensor with polymer composite films prepared at injected charge density of 250 and 1000  $\text{mC cm}^{-2}$ , respectively. The above linear range of  $\alpha\text{CRP}$  detection is wide enough to cover the whole range of relative risk categories: low risk ( $<1 \mu\text{g mL}^{-1}$ ), average risk ( $1\text{--}3 \mu\text{g mL}^{-1}$ ), and high risk ( $>3 \mu\text{g mL}^{-1}$ ) for patients with an intermediate 10-year CVD risk [28].

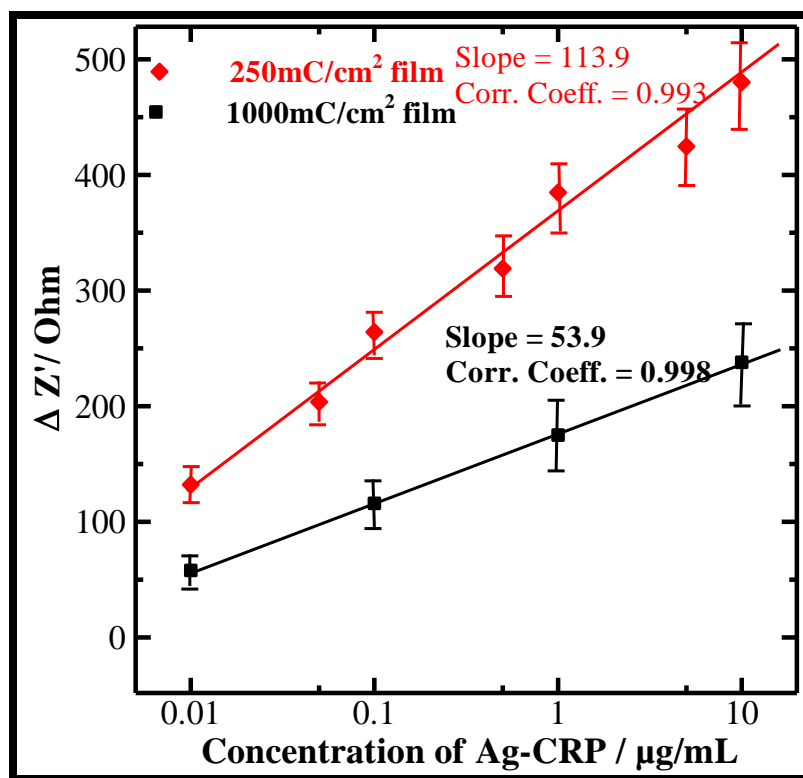


**Fig. 2.9:** Concentration dependent calibration curve of the bioelectrodes; the error bars represent the standard deviation from three separate experiments

It has been found that the thickness of the film has considerable affect on the sensitivity (slope of the calibration curve) of the immunosensor towards Ag- $\alpha\text{CRP}$ . Fig. 2.9 shows that the sensitivity of the immunosensor to Ag- $\alpha\text{CRP}$  decreases with increased thickness



of the polymer composite film. The polymer composite film prepared at injected charge density of  $250 \text{ mC cm}^{-2}$  provides a sensitivity of  $113.9 \Omega$  per decade towards Ag- $\alpha$ CRP, which is double to the sensitivity of  $53.9 \Omega$  per decade obtained with the film prepared at injected charge density of  $1000 \text{ mC cm}^{-2}$ . This is due to the generation of high capacitance upon coupling of antibody-antigen immunoreaction at thin film, where interfacial impedance is a dominant factor as compare to thick film immunosensor. Any film prepared with an injected charge density of less than  $250 \text{ mC cm}^{-2}$ , was found to be too thin to handle and was not stable for a longer time in a working solution.

## 2.4 Conclusion

In conclusion, we have reported a ZnS nanoparticles modified PPy nanocomposite film based electrochemical impedance immunosensor for the detection of  $\alpha$ CRP. The polymer composite film showed a good biocompatibility, wherein the capping agent surrounding the ZnS nanoparticles embedded within the film provided the sufficient binding site for the covalent immobilization of protein antibody molecules for immunoreaction. The immunosensor exhibited an electrochemical impedance response towards protein antigen, Ag- $\alpha$ CRP concentration in a linear range from  $10 \text{ ng mL}^{-1}$  to  $10 \mu\text{g mL}^{-1}$ . A thin film of ZnS(MPA)-PPy composite prepared at  $250 \text{ mC cm}^{-2}$  charge density showed a comparatively better sensitivity towards Ag- $\alpha$ CRP detection than high charge density film.

## 2.5 References

1. Y. Li, A. Rizzo, R. Cingolani and G. Gigli, *Adv. Mater.* 18 (2006) 2545.
2. Q. Wang and D.K. Seo, *Chem. Mater.* 18 (2006) 5764.
3. S. Coe, W. K. Woo, M. G. Bawendi and V. Bulovic, *Nature* 420 (2002) 800.
4. W. Jiang, S. Mardiyani, H. Fischer and C.W. Chan, *Chem. Mater.* 18 (2006) 872.
5. Y. Zheng, S. Gao and J. Y. Ying, *Adv. Mater.* 19 (2007) 376.
6. Rajesh, B. K. Das, S. Srinives and A. Mulchandani, *Appl. Phys. Lett.* 98 (2011) 013701.
7. L. Wu, M. McIntosh, X. Zhang and H. Ju, *Talanta* 74 (2007) 387.
8. T. Ahuja, D. Kumar and Rajesh, *Sensor Lett.* 6 (2008) 1.
9. T. Ahuja, I. A Mir, D. Kumar and Rajesh, *Biomaterials* 28 (2007) 791.
10. B Scrosati, "Applications of Electroactive Polymers", Chapman & Hall, London, 1993.
11. Y.P. Hsiao, W.Y. Su, J.R. Cheng and S.H. Cheng, *Electrochim. Acta* 56 (2011) 6887.
12. C. M. Li, C. Q. Sun, S. Song, V. E. Choong , G. Maracas and X. J. Zhang, *Front. Biosci.* 10 (2005) 180.
13. A. Kaushik, P. R. Solanki, M. K. Pandey, S. Ahmad and B. D. Malhotra, *Appl. Phys. Lett.* 95 (2009) 173703.
14. A. S Maisel, V. Bhalla and E. Braunwald, *Nat. Rev. Cardiol.* 3 (2006) 24.
15. A. Dolci and M. Panteghini, *Clin. Chim. Acta* 369 (2006) 179.
16. Rajesh, V. Sharma, V. K. Tanwar and A. M. Biradar, *Sens. Lett.* 8 (2010) 362.
17. M. Algarra, D. Gomes and J. C.G. E. da Silva., *Clin. Chim. Acta* 415 (2012) 1.

18. K. Kriz, F. Ibraimi, M. Lu, L.O. Hansson and D. Kriz, *Anal. Chem.* 77 (2005) 5920.
19. K.W. Wee, G.Y. Kang, J. Park, J.Y. Kang, D.S. Yoon, J.H. Park and T.S. Kim, *Biosens. Bioelectron.* 20 (2005) 1932.
20. N. Kim, D.K. Kim and Y.J. Cho, *Sens. Actuators, B* 143 (2009) 444.
21. Y. P. Timalisina, J. Branan, B. E. Aston, K. Noren, G. Corti, R. Schumacher and D. N. Nellroy, *J. Appl. Phys.* 110 (2011) 014901.
22. Rajesh, T. Sarkar and A. Mulchandani, *Appl. Phys. Lett.* 99 (2011) 173110.
23. M. K. Ram, M. Adami, S. Paddeu and C. Nicolini, *Nanotechnology* 11(2000)112.
24. A. Joshi, D. K. Aswal, S. K. Gupta, J. V. Yakhmi and S. A. Gangal, *Appl. Phys. Lett.* 94 (2009) 103115.
25. R.G. Davidson and T.G. Turner, *Synth. Met.* 72 (1995)121.
26. M. Gamero, F. Pariente, E. Lorenzo and C. Alonso, *Biosens. Bioelec.* 25 (2010) 2038.
27. F. Lisdat and D. Schafer, *Anal. Bioanal. Chem.* 391(2008)1555.
28. B. McDonnell, S. Hearty, P. Leonard and R. O’Kennedy, *Clin. Biochem.* 42 (2009) 549.

## CHAPTER 3

---

### Protein functionalized Pt(MPA)-PPy nanocomposite film based bioelectrode

---

*In this chapter an electrochemically prepared 3-mercaptopropionic acid (MPA) capped Platinum nanoparticles-Polypyrrole (PPy) nanocomposite film based bioelectrode for the detection of C-reactive protein ( $\alpha$ CRP) has been described. The electrochemical deposition provides homogeneous distribution of ultrafine Pt(MPA)-NPs within the uniform and adherent PPy film with high degree of geometrical conformity and controllable film thickness. Protein antibody, Ab- $\alpha$ CRP, was covalently immobilized through the site specific carboxyl groups of Pt(MPA)-NPs within the polymer nanocomposite film by carbodiimide coupling reaction. The bioelectrode interfacial surface electron transport study towards protein antigen, Ag- $\alpha$ CRP, was carried out by electrochemical impedance spectroscopy (EIS). The value of 'n', a Constant Phase Element exponent used as a gauge of the heterogeneity, for Pt(MPA)-PPy nanocomposite film was found to be 0.88~1 which is indicative of a rather homogenous morphology of the composite film with minimal defects. The EIS of the bioelectrode exhibited significant changes in charge transfer resistance ( $R_{et}$ ) component at a low ac frequency of < 20 Hz towards Ag- $\alpha$ CRP detection over a linear range of 10 ng mL<sup>-1</sup> to 10  $\mu$ g mL<sup>-1</sup> in PBS with a sensitivity of 109.74  $\Omega$  cm<sup>2</sup> per decade.*

### 3.1 Introduction

With the rapid development of nanotechnology over the past decade, various nanomaterials, including nanowires, nanotubes and nanoparticles have found a variety of potential applications especially in the field of proteins detection and catalysts modification [1-3]. The nanomaterials are preferred as suitable matrices for antibodies immobilization with proper orientation, due to their unique optical, electrical and molecular properties and in particular their extremely large surface areas, high reactivity and beneficial chemically tailored physicochemical properties, that help to obtain a sensitive, compact, and stable immunosensor [4-5]. Nanocomposites of electrically conducting polymers and metal nanoparticles have found great attention not only because of the scientific curiosity, but also for their potential applications in molecular electronic devices, gas sensors, biosensors, capacitors and catalysts [6-10]. The nanocomposites of PPy and noble metal particles (such as Pt, Au, Ag, and Pd) exhibit interesting and excellent physical or chemical properties (optical, electrochemical and conductive properties) due to the hybridization of metal nanoparticles and  $\pi$ -conjugated polymers and are currently of great research interest, essentially motivated by their high analytical sensitivity in sensing applications [11-13]. Also, the polymer coating improves the stability of the metal nanoparticles which are otherwise stable as a suspension solution only and tend to undergo irreversible aggregation over time. Among the noble metals, Pt nanoparticles are typical inorganic nanomaterials with excellent chemical and physical properties [14]. The distinctive properties of Pt at nanoscale dimensions have attracted widespread attention in their utilization for the bioassay,

especially for electrochemical detection, where they can be used as conductive pathway for electron transfer, improving the electrochemical reactions at a low potential. The Pt nanoparticles are considered very effective as a matrix for the immobilization and study of various kinds of biomolecules and macromolecules, such as DNA, enzymes, other proteins and antibodies by taking advantage of their biocompatibility and high surface area [15, 16].

Due to the risk of severe consequences for patients with high  $\alpha$ CRP concentrations, bio-analytical devices of high sensitivity are required that allow a fast and precise diagnosis of disease at an early stage. Hu et al. has developed a CRP sensor based on Surface Plasmon Resonance (SPR) biosensing methodology, where CRP antibodies were bound to a gold (Au) surface through Protein G, having a detection limit of 8 nM ( $1 \mu\text{g mL}^{-1}$ ) of purified CRP [17]. Meyer et al. has also established an SPR immunosensor for CRP detection based on two different anti-CRP antibodies: one for CRP entrapment and one for labeling with a linear detection range of 16–40 nM ( $2\text{--}5 \mu\text{g mL}^{-1}$ ) CRP in PBS buffer [18].

In this work, we report a single step electrochemical polymerization of p-toluene sulphonic acid doped PPy in conjunction with MPA capped Pt nanoparticles for the preparation of an electroactive Pt(MPA)-PPy nanocomposite film on an ITO coated glass plate. The free carboxyl groups of the MPA capped Pt-NPs intercalated within the polymer film were utilized for the site specific immobilization of protein antibody, Ab- $\alpha$ CRP, using carbodiimide coupling reaction, for the construction of a bioelectrode. These 3-dimensional MPA capped Pt-NPs not only provided the high protein loading

with efficient covalent binding due to their large surface area to volume ratio and availability of free pendant carboxyl groups for better probe orientation but also facilitated the improved charge shuttling throughout the material. This site-specific and efficient bio-molecular immobilization of Pt-NPs together with the conducting polymer matrix helped in enhancing the impedance response sensitivity of the bioelectrode towards the detection of target protein antigen, Ag- $\alpha$ CRP, in phosphate buffer solution (PBS; pH 7.4).

## 3.2 Experimental

### 3.2.1 Reagents

Ab- $\alpha$ CRP (Cat 4C28 mAbC2) and Ag- $\alpha$ CRP (Cat 8C72) were obtained from Hytest (Turku, Finland). Mouse immunoglobulin-G (Ag-IgG) (Cat IGP3) was obtained from GENEI, Bangalore, India. Hydrogen hexachloroplatinate hexahydrate ( $H_2PtCl_6 \cdot 6H_2O$ ) and sodium borohydride ( $NaBH_4$ ) were purchased from Aldrich. Pyrrole (Py), Para toluene sulphonic acid (pTSA), 3-Mercaptopropionic acid 99% (MPA), N-(3-Dimethylaminopropyl)-N'-ethyl carbodiimide hydrochloride (EDC) and N-Hydroxy Succinimide 98% (NHS) were obtained from Sigma-Aldrich chemicals. All other chemicals were of analytical grade and used without further purification.

### 3.2.2 Equipments

Electropolymerization, cyclic voltammetry (CV) and EIS measurements were done on a PGSTAT302N, AUTOLAB instrument from Eco Chemie, The Netherlands. The EIS experiments were carried out at a bias voltage of 0.3 V vs Ag/AgCl with an ac voltage of

---

0.05 V in the frequency range of 1 Hz to 100 kHz. XRD pattern were recorded using Bruker AXS Advance D8 powder X-ray diffractometer. Microstructural characterization was carried out by high resolution transmission electron microscopy (HRTEM model: Tecnai G2 F30 STWIN with field emission gun, operated at 300 kV). AFM images were obtained on VEECO/DICP2, USA scanning probe microscope. FTIR spectra of the films were taken on a Nicolet 5700 FTIR spectrometer.

### *3.2.3 Preparation of bioelectrode*

MPA capped Pt nanoparticles were synthesized by conventional sodium borohydride reduction method in aqueous solution with slight modification [19]. For the preparation of Pt(MPA)-PPy nanocomposite film, the ITO coated glass plates ( $10\Omega / \square$ ) were first cleaned by sequential ultrasonic cleaning in extran, acetone, ethanol, isopropyl alcohol and DI for 10 min each and dried in vacuum. The Pt(MPA)-PPy nanocomposite film was electrochemically deposited on an ITO-glass plate (0.5 cm x 0.5 cm) by using chronopotentiometric method from an aqueous solution containing  $0.1 \text{ mg mL}^{-1}$  Pt(MPA), 25 mM pyrrole and 25 mM pTSA, at a fixed current density of  $1 \text{ mA cm}^{-2}$  with a total injected charge density of  $250 \text{ mC cm}^{-2}$ . Ab- $\alpha$ CRP was covalently attached to site-specific pendant carboxyl groups of MPA capped Pt NPs-PPy nanocomposite film on ITO-glass using EDC-NHS chemistry where EDC and NHS worked as a coupling agent and an activator, respectively. In brief, Pt(MPA)NPs-PPy/ITO-glass plate was first incubated in a solution mixture of 30 mM NHS and 150 mM EDC for 1 hr and then in  $100 \mu\text{g mL}^{-1}$  Ab- $\alpha$ CRP in PBS (pH 7.4), for an overnight period, at a temperature of  $4^\circ\text{C}$ , followed by washing with PBS and drying with  $\text{N}_2$  gas flow. Finally, the bioelectrode

---



was incubated in 1.0% (W/V) bovine serum albumin (BSA) solution for 30 min. to block the non-specific reactive sites, if available, on the Pt-NPs and/or PPy surface, and subsequently rinsed with PBS, dried under N<sub>2</sub> gas flow and stored at 4° C. The stepwise construction of the prototype assembly is schematically represented in Fig. 3. 1.

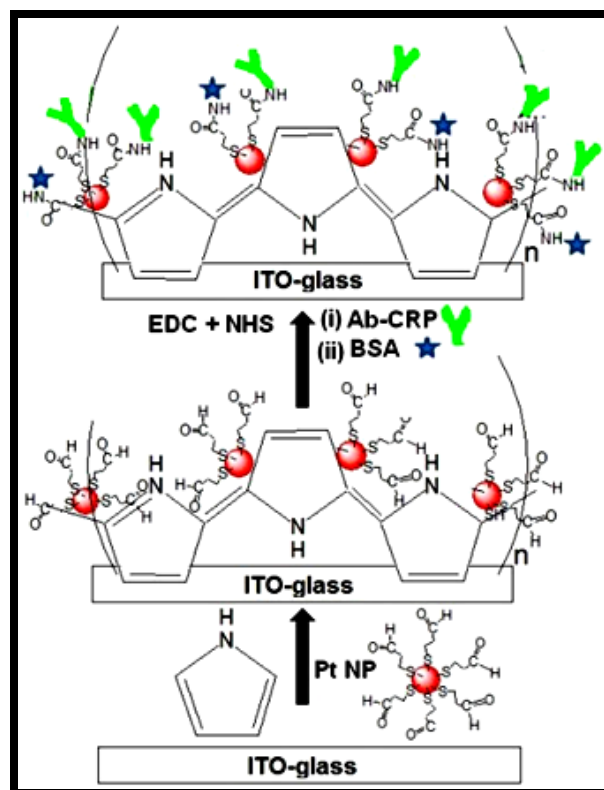


*Fig. 3.1: Schematic representation of the stepwise fabrication of the bioelectrode*

### 3.3 Results and Discussion

#### 3.3.1 Micro structural characterization

Figure 3.2 shows XRD spectra of both the pristine PPy and Pt(MPA)NPs-PPy nanocomposite films. A broad diffraction peak at  $2\theta = 25.54^\circ$  (inset Fig. 3.2) was obtained for PPy, indicating a low order of crystallinity due to the PPy intermolecular

spacing. The XRD patterns of Pt(MPA)-PPy nanocomposite film showed a broad characteristic peak for PPy together with the faint Pt diffraction peaks indicative of the Pt NPs fully covered with PPy. These Pt(MPA)NPs characteristic peaks obtained at  $2\theta = 38.4^\circ$ ,  $45.5^\circ$ , and  $64.70^\circ$  corresponds to (111), (200), and (220) planes, respectively, of a faced center-cubic (fcc) structure.

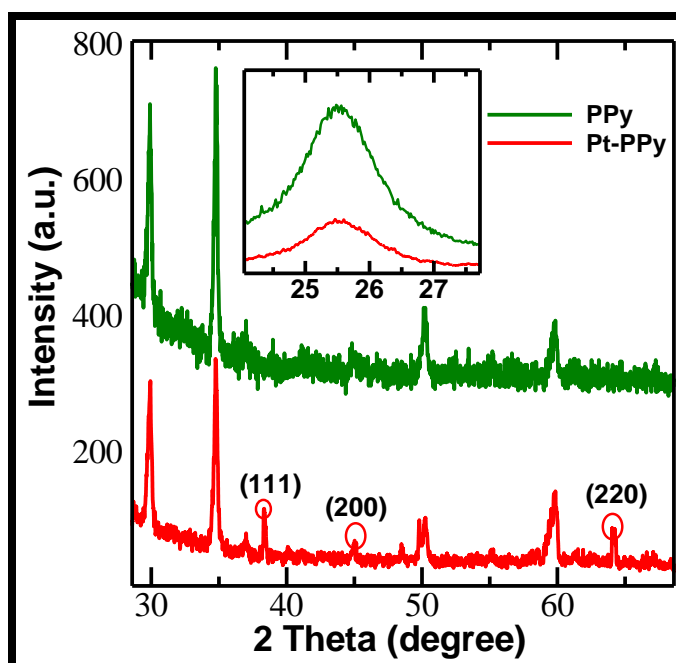


**Fig. 3.2:** XRD Pattern of pristine PPy and Pt(MPA)NPs-PPy composite

Figure 3.3 shows the FTIR spectra of PPy and Pt(MPA)-PPy taken on an attenuated total reflection mode, which provides an additional information regarding the formation of Pt(MPA)-PPy nanocomposite.

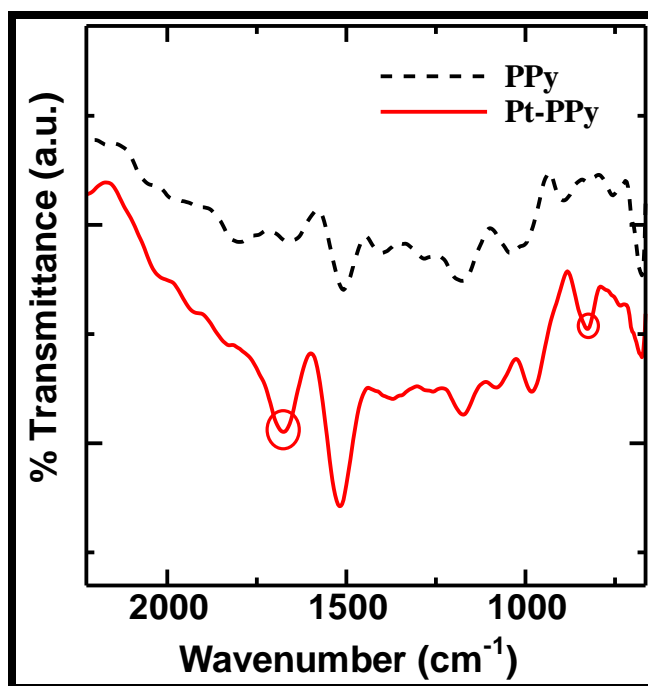


**Fig. 3.3:** FTIR spectra of PPy and Pt(MPA)-PPy showing additional peaks and shift in peak positions

The pure PPy film shows the characteristic peaks of  $893\text{ cm}^{-1}$  ( $=\text{C-H}$  out-of-plane vibration) indicating the polymerization of pyrrole,  $1036\text{ cm}^{-1}$  and  $1176\text{ cm}^{-1}$  corresponding to  $=\text{C-H}$  in-plane vibration and (N-C stretch bending) respectively, while the two other bands at  $1405\text{ cm}^{-1}$  and  $1515\text{ cm}^{-1}$  can be attributed to the symmetric and anti-symmetric ring stretching mode of PPy, indicating the extent of conjugation of the PPy structure. The FTIR spectra of Pt(MPA)-PPy composite film exhibited a sharp peak at  $1677\text{ cm}^{-1}$  that may be attributed to C=O stretching mode of the free carboxyl groups of MPA capped Pt NPs encapsulated in PPy matrix. Moreover, the significant changes were found both in peak's position as well as in intensity in the FTIR spectra of Pt(MPA)-PPy composite in comparison to pristine PPy, showing red shifts in the characteristic peaks at  $893$ ,  $1036$  and  $1176\text{ cm}^{-1}$  to  $825$ ,  $984$  and  $1168\text{ cm}^{-1}$ , respectively.

This may be attributed to the doping of PPy with Pt(MPA) due to good interaction between the two moieties, as found earlier in case of PPy-Ag nanofiber composite [20].

HRTEM characterization was carried out on the Pt (MPA)-PPy nanocomposite film, which was electrochemically deposited on a carbon-coated TEM grid by taking it as a working electrode using the same method as describe for ITO-glass support. The micro structural features of the Pt(MPA)NPs-PPy composite film was investigated by HRTEM measurements. The HRTEM microstructure of Pt(MPA)NPs depicts uniform distribution of Pt NPs with individual particles revealing faceted growth with a nature of intermingling to each other (Fig. 3.4a). The Gaussian histogram revealed the size of Pt NPs in the range of 2 to 9 nm in general and 4 to 5 nm on average (Fig. 3.4 b).

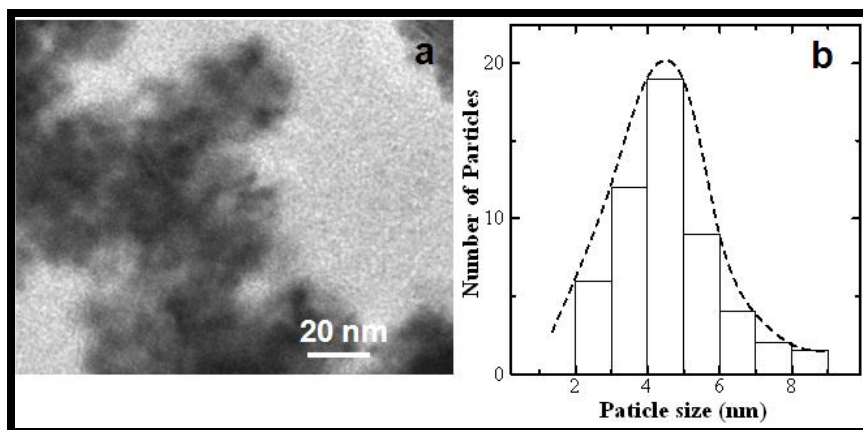


**Fig. 3.4:** HRTEM image of (a) distribution of nanoparticles and (b) Gaussian size-distribution curve of the nanoparticles.

These Pt-particles embedded in PPy exhibited a very random distribution of a homogeneous dispersion. A contour of Pt-particles revealing most of the instances very uniform formation of a nanocomposite of metal with a base-matrix of a polymer, has been marked with a white dotted line throughout the micrograph (Fig. 3.5a). A

corresponding selected area electron diffraction pattern (SAEDP) recorded from the composite microstructure, elucidates the presence of important planes, in the form of Debye rings, of Pt-face centered cubic structure (space group:  $Fm\bar{3}m$ , and lattice parameter:  $a = 0.39$  nm, ref. JCPDF card no. 040802) with the interplanar spacings of 0.23, 0.20 and 0.14 nm corresponding to hkl: 111, 200 and 220, respectively (inset in Fig. 3.5a). An open arrow marked on a diffuse ring shows the electron diffraction pattern of the PPy (inset in Fig. 3.5a), typical reciprocal space information normally obtained in case of a polymer-matrix.

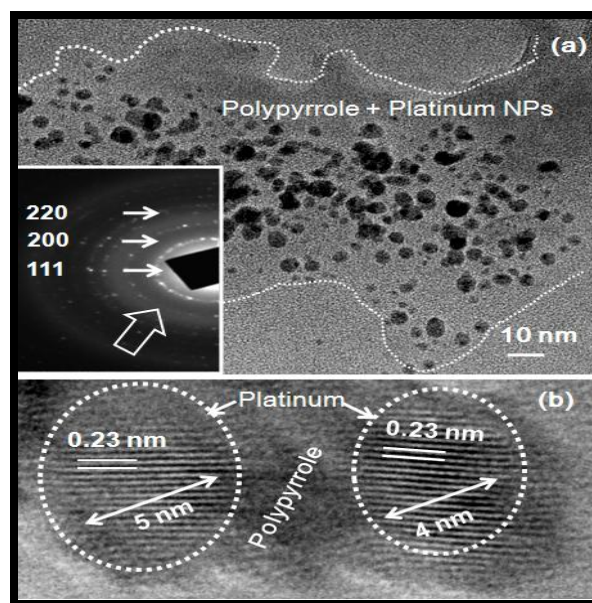


**Fig. 3.5:** HRTEM image showing (a) distribution of Pt-nanoparticles in a PPy-matrix, and (b) atomic scale images of Pt-nanoparticles in the PPy matrix; Inset: SAEDP of nanocomposite.

It is important to mention that there is also a possibility of the existence of a minor crystallinity in polymer too, nevertheless in general such materials gives rise to diffuse-ring contrast in the reciprocal space. However a coexistence of uniform rings of Pt and

diffuse ring of PPy further authenticates a good quality homogeneous two phase material of a nano-composite. Atomic scale imaging performed on polymer-Pt(MPA)NPs composite clearly shows that the individual Pt-particles are immersed in the polymer matrix without any porosity leaving behind a good interface between the two dissimilar materials (Fig. 3.5b). In both the particles, crystallographic planes of hkl: 111 (interplanar spacing: 0.23 nm) are well oriented and constituted the entire individual crystallites. Moreover the individual Pt-particles of about 4 to 5 nm in size are separated apart about a distance of 5 nm with a uniform linkage of PPy-matrix in between (Fig. 3.5b).

The surface morphology of the substrate was further investigated by taking the subtle AFM surface topographical images of the pristine PPy, Pt(MPA)NPs-PPy composite and biofunctionalized Ab- $\alpha$ CRP/Pt(MPA)NPs-PPy film, as shown in Fig. 3.6. AFM image of pristine PPy shows globular morphology of the polymer film with significant depressions and high points, having surface roughness parameter ( $R_a$ ) value of 8.8 nm (Fig. 3.6a). However, this has been found to be altered to a symmetric dense grainy structure having  $R_a$  value of 2.7 nm in the Pt(MPA)NPs-PPy composite film with the formation of some large grains by nanometric subunits (Fig. 3.6b). A significant increase in  $R_a$  value to 3.9 nm showed a comparatively high surface roughness of the composite film after protein Ab- $\alpha$ CRP immobilization with a globular looking feature of the protein molecules [21]. This may be due to the non compact assembly of the protein molecules over the composite film resulting from the covalent bonding of protein to free carboxyl groups of Pt(MPA)NPs over the PPy matrix.

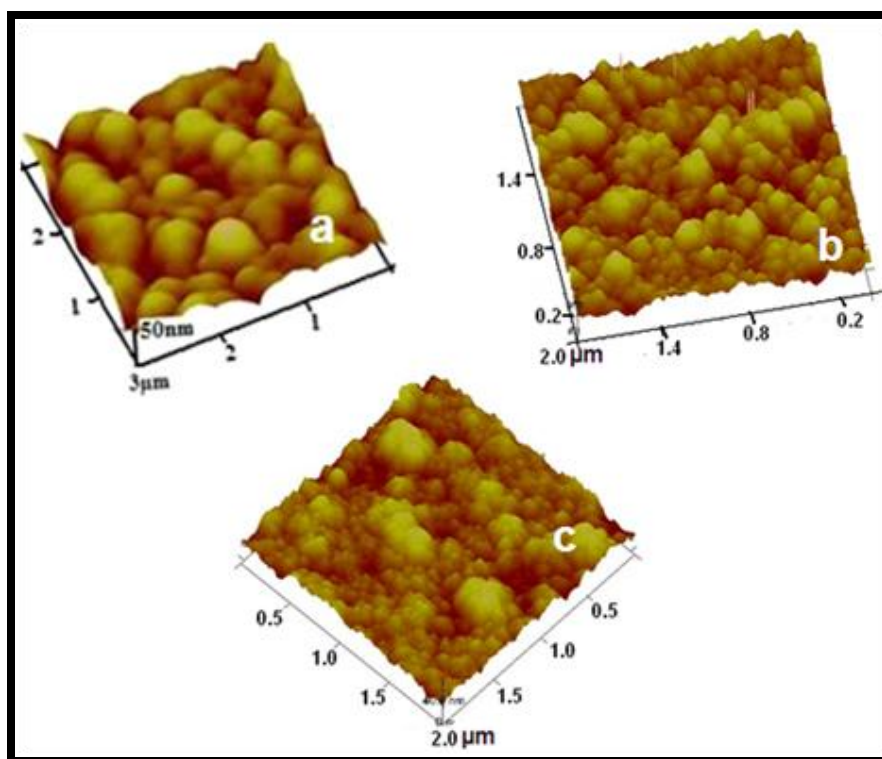


**Fig. 3.6:** AFM images of (a) PPy/ITO-glass, (b) Pt(MPA)NPs-PPy/ITO-glass and (c) Ab- $\alpha$ CRP/Pt(MPA)NPs-PPy/ITO-glass plate

### 3.3.2 Electrochemical characterization of the bioelectrode

Alternating current (AC) impedance or EIS is known as an effective tool for the qualitative and quantitative characterization of electrochemical processes occurring in the conducting polymer films [22, 23]. Some factors like microscopic chemical inhomogeneity and roughness of the electrode make it difficult to describe such a system in terms of the known properties of an ideal capacitor. So, for such systems a non-intuitive circuit element called Constant Phase Element (CPE) has been used for the purpose of describing the electrochemical behavior of inhomogeneous electrode. CPE is thus related to surface inhomogeneity, roughness or fractal geometry, electrode porosity,

current and potential distribution associated with the electrode geometry and its impedance is represented by the Eqn. (3.1) [24]:

$$Z_{\text{CPE}}(\omega) = Y_0^{-1} (j\omega)^{-n} \quad (3.1)$$

where  $Y_0$  is the frequency-independent constant relating to the surface electroactive properties,  $\omega$  is the radial frequency,  $j$  is an imaginary unit, the exponent  $n$  arises from the slope of  $\log Z$  vs.  $\log f$  (and has values  $-1 \leq n \leq 1$ ). An  $n$  value of zero corresponds to a pure resistor; a unit value of  $n$  corresponds to a pure capacitor, while a 0.5 value corresponds to Warburg impedance ( $Z_w$ ) which is associated with the domain of mass transport control arising from the diffusion of ions to and from the electrode/solution interface. The deviation of frequency ( $\omega$ ) exponent  $n$  from ideal values was attributed to the homogeneities of analyzed layer, such as roughness or defects. In the present case, the value of  $n$  for the Pt(MPA)NPs-PPy composite film was found close to 1 (table 3.1), which indicated a minimal defects in the fabricated nanocomposite film on the electrode surface and the CPE resembling a capacitor. The modified Randles' equivalent circuit was used to obtain fitted Nyquist plots that match with experimental Nyquist plots through computer simulations. The Nyquist plots (real part of the impedance  $Z'$  vs. imaginary part  $-Z''$ ) obtained after various steps of surface modifications of the electrode are presented in Fig. 3.7a. The semicircle diameter of the Nyquist plot is equal to  $R_{\text{ct}}$  which controls the electron transfer kinetics of the redox probe at the electrode interface. Since the Chi-squared function ( $\chi^2$ ) is the measure of the quality of the fitted data, a small  $\chi^2$  of the order of  $10^{-4}$  obtained in the present case suggested an appropriate

---



selection of the circuit model. Significant differences in the impedance spectra in terms of  $R_{et}$  values (Table 1) were observed during stepwise modification of the electrode. The bare PPy/ITO-glass electrode showed a  $R_{et}$  value of  $26.8 \Omega \text{ cm}^2$ , which increases to  $46.2 \Omega \text{ cm}^2$  for Pt(MPA)NPs-PPy/ITO-glass electrode with a decrease in  $Y_0$  value from  $4.36 \mu\text{Fcm}^{-2}$  to  $2.46 \mu\text{Fcm}^{-2}$ . This increase in  $R_{et}$  value and subsequent decrease in  $Y_0$  value for Pt(MPA)NPs-PPy/ITO-glass electrode may be attributed to the presence of negatively charged carboxyl terminal groups on the electrode surface which generates a repulsive effect towards negatively charged probe ions at the electrode/solution interface thus reducing the ability of the probing electrolyte to penetrate the layer. This assumption was further evidenced by the use of non-carboxyl functionalized Pt NPs-PPy/ITO-glass electrode which showed a drop off in  $R_{et}$  value to  $14.2 \Omega \text{ cm}^2$  with a significant increase in  $Y_0$  value to  $5.1 \mu\text{Fcm}^{-2}$  due to the unhindered approach of the probe ions towards the electrode surface at the electrode/solution interface. A significant increase in the  $R_{et}$  value to  $98.5 \Omega \text{ cm}^2$  and decrease in  $Y_0$  value to  $1.88 \mu\text{Fcm}^{-2}$  was obtained after the site specific immobilization of the protein Ab- $\alpha$ CRP on the Pt(MPA)NPs-PPy/ITO-glass electrode. This increment in the  $R_{et}$  value and decrease in  $Y_0$  value is due to the insulating behavior of the immobilized protein antibody layer on the bioelectrode surface, which acts as an electron communication and mass-transfer blocking layer, thereby hindering the access of redox probe towards the electrode surface and thus resulting in a sluggish electron-transfer kinetic.

Although the Nyquist plots are more commonly displayed, the data in a Nyquist plot is often poorly resolved (particularly at high frequencies), and the explicit frequency

dependence is not displayed. Hence, bode plot was used to provide a more clear description of the electrochemical system's frequency-dependent behavior. The Bode plots display both the logarithm of the total impedance  $|Z|$  as calculated by Eqn. (3.2) and the phase angle ( $\varphi$ ) as a function of the logarithm of the frequency.

$$Z(\omega) = Z'(\omega) + i Z''(\omega) \quad (3.2)$$

In the bode plot as shown in Fig. 3.7b,  $\varphi$  was found to be nearly zero at a frequency  $> 25$  KHz, which corresponds to in phase relationship between the applied voltage and the current, resembling the circuit element  $R_s$ . Negligible changes were obtained in the Log  $|Z|$  values for the modified electrodes with respect to changes in frequency values in this region indicating that the  $R_s$  is independent of frequency. At frequency  $< 25$  KHz, particularly in the intermediate range of frequency where an increase in the value of  $\varphi$  was obtained for the modified electrodes with peak values of  $\varphi > 0^\circ$  but  $< 90^\circ$  showed the presence of a dielectric region where the signal was dominated by the dielectric pseudo capacitive circuit element, CPE. It is to be noted that in the case of bioelectrode the peak value of  $\varphi$  gets shifted towards the lower frequency region in comparison to both the Pt(MPA)NPs-PPy/ITO-glass and pristine PPy/ITO-glass electrodes indicating the presence of the charge storage properties i.e. showing a capacitive behavior even at low frequencies. At lower frequencies, the impedance corresponding to CPE becomes very high so the current flows only through  $R_{et}$  and  $Z_w$ . This phenomena was observed at frequency  $< 80$  Hz for both the Pt(MPA)NPs-PPy/ITO-glass and PPy/ITO-glass electrodes while the same was observed at comparatively much lower frequency of  $< 20$  Hz for the bioelectrode exhibiting a predominant charge transfer behaviour. This bio

interfacial charge transfer phenomenon at a very low frequency region shows a biocompatible behaviour of the bioelectrode.

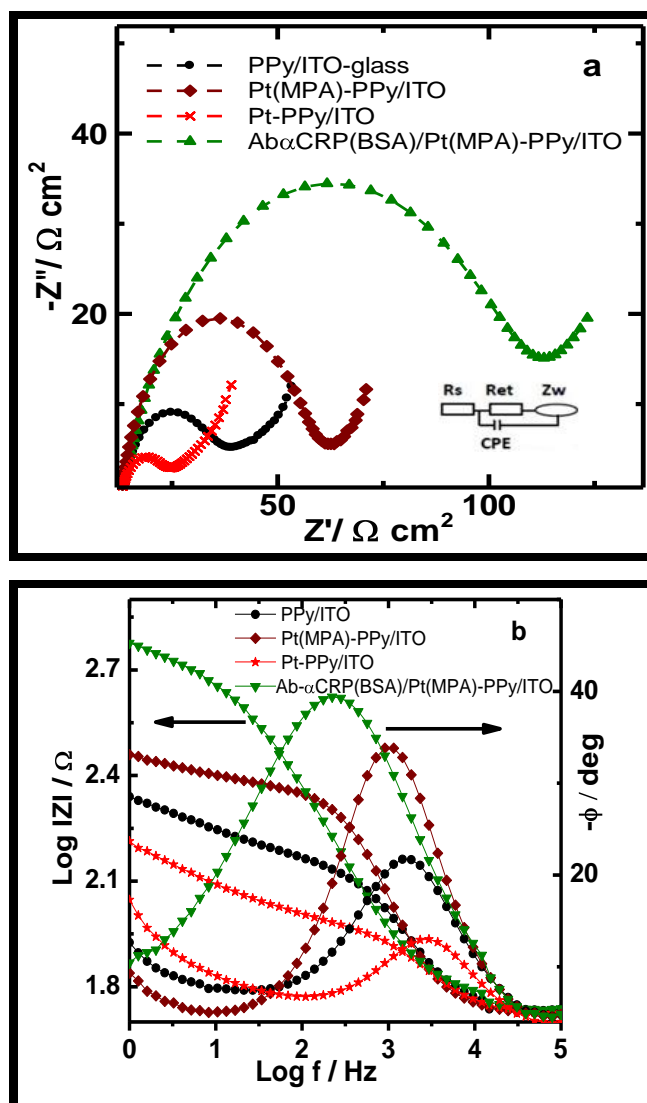


**Fig. 3.7:** (a) Nyquist plots obtained for pristine PPy-ITO glass, Pt(MPA) NPs-PPy/ITO-glass, Pt-PPy/ITO-glass and Ab- $\alpha$ CRP/Pt(MPA)NPs-PPy/ITO-glass in PBS (pH 7.4, 0.1M KCl) containing 2mM  $[\text{Fe}(\text{CN})_6]^{3-/4-}$  and (b) Corresponding bode plots

Davies and Compton employed a theoretical framework to determine the diffusion layer thickness  $\delta$ , which helps in categorizing the type of diffusion occurring at

the spatially heterogeneous electrodes such as those represented by porous electrodes, partially blocked electrodes, microelectrode arrays, and electrodes made of composite materials [25, 26]. The value of  $\delta$  can be obtained from the modified Einstein equation for the root mean square displacement of diffusing particles as shown in Eqn. 3.3 and listed in table 3.1:

$$\delta = (2D\Delta E/v)^{1/2} \quad (3.3)$$

where  $D$  is diffusion coefficient of aqueous ferrocyanide ( $6.3 \times 10^{-6} \text{ cm}^2\text{s}^{-1}$ ),  $\Delta E$  is the potential width of the voltammogram and  $v$  is the scan rate ( $0.05 \text{ Vs}^{-1}$ ). The  $\delta$  values obtained for the modified electrodes indicates that a case 3 type of behavior related to the voltammetric responses of spatially heterogeneous electrodes, was occurring at the electrode/electrolyte interface. This type of behavior is associated with an overlap of adjacent diffusion layers resulting from the small size of the inert part of the electrode [27].

**Table 3.1:** EIS parameters at various stages of surface modification of the electrodes

Type of Electrodes	$R_{et}$ ( $\Omega\text{cm}^2$ )	CPE		$Z_w$ ( $\times 10^{-3}$ ) ( $\Omega\text{cm}^2$ )	$\chi^2$ ( $\times 10^{-4}$ )	$\delta$ ( $\mu\text{m}$ )
		$Y_0$ ( $\mu\text{Fcm}^{-2}$ )	$n$			
PPy/ ITO-glass	26.8	4.36	0.84	5.42	3.08	56.5
Pt(MPA)/PPy/ ITO	46.2	2.46	0.88	5.94	3.15	59.1
Pt/PPy/ ITO	14.2	5.10	0.85	5.10	2.45	55.2
Ab- $\alpha$ CRP/Pt(MPA)/PPy/ ITO	98.5	1.88	0.86	4.18	1.48	69.1

Useful information regarding electrochemical mechanism occurring at the electrode /electrolyte interface of the bioelectrode can be acquired from the relationship

between the peak current and the scan rate. The various CV obtained for the bioelectrode at different scan rates in the range from 25-125  $\text{mV s}^{-1}$  in PBS (pH 7.4) containing 2mM  $[\text{Fe}(\text{CN})_6]^{3-/4-}$  are shown in Fig. 3.8.

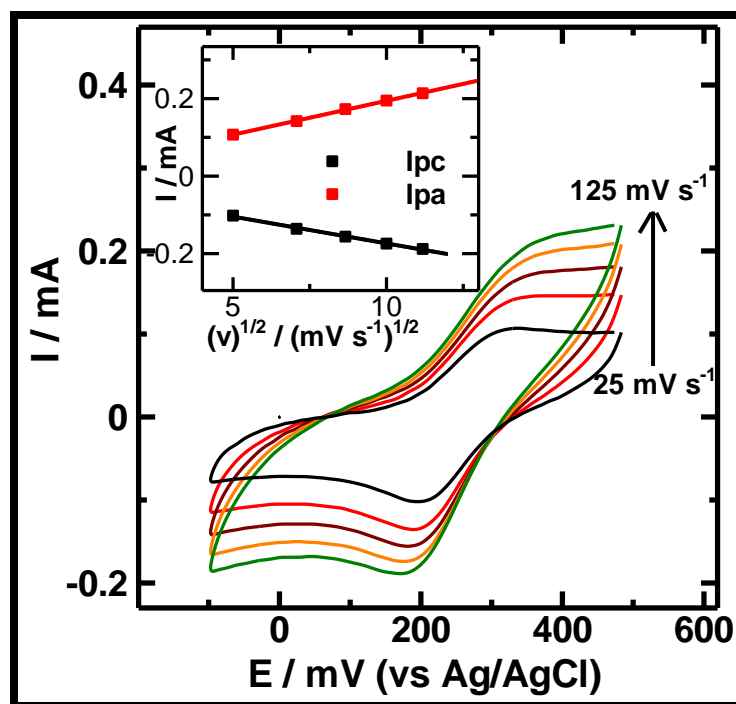


**Fig. 3.8:** CV of bioelectrode as a function of scan rate in PBS (pH 7.4, 0.1M KCl) containing 2mM  $[\text{Fe}(\text{CN})_6]^{3-/4-}$ . Inset: plot of redox peak current vs  $v^{1/2}$

### 3.3.3 Electrochemical impedance response to protein antigen

From a stock solution of  $100 \mu\text{g mL}^{-1}$  of protein antigen, Ag- $\alpha$ CRP, aliquots of different concentrations were prepared in PBS. EIS response of the bioelectrode was measured after the addition of successive aliquots of different concentrations of protein antigen Ag- $\alpha$ CRP in PBS (pH 7.4, 0.1 M KCl) solution containing 2 mM  $[\text{Fe}(\text{CN})_6]^{3-}/[\text{Fe}(\text{CN})_6]^{4-}$  at the scanning frequencies from 1 Hz to 10 kHz. The immunoreaction was

performed in this frequency range as in the frequency region of  $<1$  Hz bioelectrode exhibited perturbations in EIS signal which amounts to a significant variations in the circuits' elemental parameters while above 10 kHz the EIS signal remains independent of frequency. Figure 3.9 (a & b) shows the Nyquist and Bode plots of the bioelectrode obtained with different added concentrations of target Ag- $\alpha$ CRP. The  $R_{et}$  value of the bioelectrode corresponding to a sample solution containing no protein antigen was taken as the control sample response. Supplementary addition of successive aliquots of different concentration of protein antigen to the control sample solution leads to the formation of antibody-antigen immunocomplex at the bioelectrode surface which hinders the biointerfacial electron transfer resulting in an increase in the corresponding fitting values of  $R_{et}$  (Table 3.2). On comparing the changes in the values of different circuit elements after each subsequent immunoreaction with added protein antigen concentration (as shown in Table 3.2), the changes in  $R_{et}$  values were found to be much more prominent than those of other impedance components. Hence, it has been taken as a suitable signal response for immunosensing purpose. A small but noticeable decrease in  $Y_0$  values (Table 3.2) was also observed with subsequent immunoreaction indicating a decrease in capacitive behavior of the bioelectrode with immunoreaction. The frequency spectrum as represented by the Bode plot in Fig. 3.9 b can be approximately divided into three main regions.

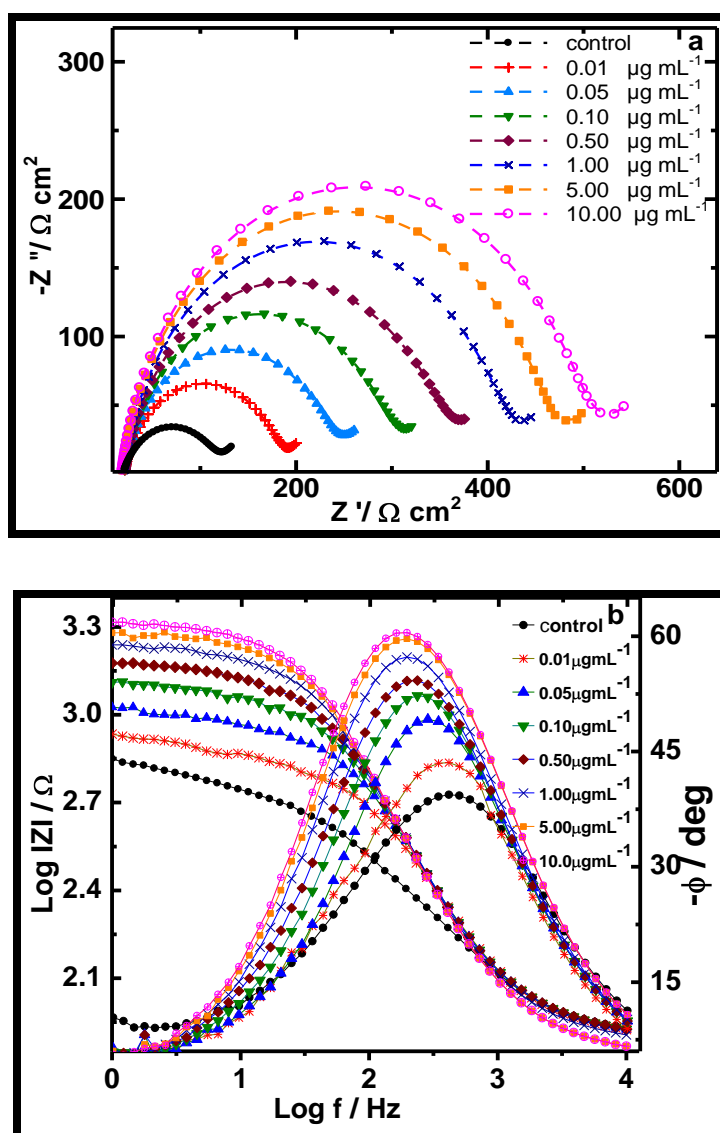


**Fig. 3.9:** (a) Faradaic impedance spectra of the Ab- $\alpha$ CRP/Pt(MPA)-PPy/ITO-glass bioelectrode before and after incubating with different concentrations of Ag- $\alpha$ CRP in PBS (pH7.4) with 0.1 M KCl solution containing 2 mM  $[\text{Fe}(\text{CN})_6]^{3-/4-}$  (b) Corresponding bode plots

It was observed that both the low and high frequency region of the spectra were dominated by a resistance while the mid spectrum region by a capacitance. The high-frequency region ( $>7$  KHz) was more related to the electrolyte ionic transfer behavior

and here solution resistance  $R_s$  plays a critical role. In the intermediate range of frequency i.e. from 7 kHz to 50 Hz a phase angle greater than  $40^\circ$  but less than  $90^\circ$  was obtained, indicating a dielectric pseudo capacitive behavior at the bioelectrode/solution interface. At the low frequencies,  $< 20$  Hz, electrode polarization and electrode kinetics becomes the principal factors contributing to the impedance and thus increases the importance of the charge transfer process, which relates to the circuit element  $R_{et}$ . In this low frequency region, we obtained significant changes in the log modulus of  $|Z(f)|$  with the increasing antigen, Ag- $\alpha$ CRP concentration, which indicates that when the antigen is linked to the specific sites of the antibody on immunoreaction, the  $R_{et}$  value increases.

**Table 3.2:** EIS characteristic parameters of the bioelectrode upon immunoreaction

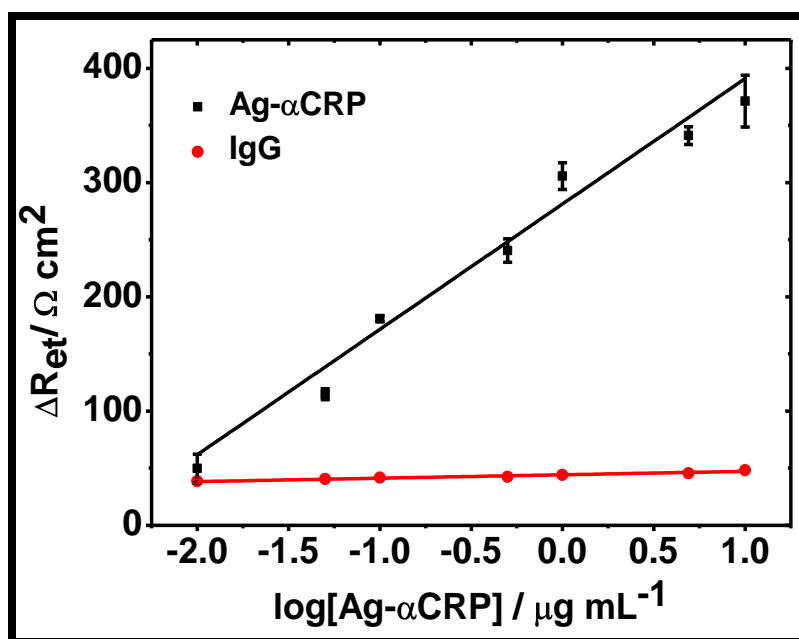
Concentration of Ag- $\alpha$ CRP	$R_{et}$ ( $\Omega\text{cm}^2$ )	CPE ( $Y_0$ ) ( $\mu\text{Fcm}^{-2}$ )	n	$Z_w$ ( $\times 10^{-3}$ ) ( $\Omega\text{cm}^2$ )	$\chi^2$ ( $\times 10^{-4}$ )
Control	98.5	7.55	0.862	4.18	1.48
$0.01\mu\text{g mL}^{-1}$	157.2	6.14	0.878	3.81	9.12
$0.05\mu\text{g mL}^{-1}$	216.7	5.34	0.875	3.72	2.29
$0.10\mu\text{g mL}^{-1}$	277.5	5.13	0.880	3.30	2.59
$0.50\mu\text{g mL}^{-1}$	331.8	5.01	0.884	3.10	3.11
$1.00\mu\text{g mL}^{-1}$	396.0	4.63	0.894	2.73	3.55
$5.00\mu\text{g mL}^{-1}$	445.2	4.44	0.900	2.70	4.48
$10.00\mu\text{g mL}^{-1}$	485.8	4.32	0.903	2.54	4.89

Figure 3.10 shows a linear relationship between the change in specific electron charge transfer resistance ( $\Delta R_{et} = (R_{et})_{\text{after immunoreaction}} - (R_{et})_{\text{control}}$ ) and logarithmic value



of Ag- $\alpha$ CRP concentration in the range of  $10 \text{ ng mL}^{-1}$  to  $10 \text{ }\mu\text{g mL}^{-1}$  and is represented by the Eqn. (3.5):

$$\Delta R_{\text{et}} = b \log [\text{Ag-}\alpha\text{CRP}] + c \quad (3.5)$$



*Fig. 3.10: Concentration dependent calibration curve of bioelectrode; the error bars represent the standard deviation from three separate experiments*

The bioelectrode showed sensitivity (slope  $b$  of the calibration curve) of  $109.74 \text{ }\Omega \text{ cm}^2$  per decade of Ag- $\alpha$ CRP and intercept  $c$  of  $281.26 \text{ }\Omega \text{ cm}^2$  having a correlation regression coefficient of 0.990 ( $n = 7$ ). The limit of detection was found out to be  $4.54 \text{ ng mL}^{-1}$  based on three times of signal-to noise ratio. The EIS detection procedure described above did not involve any pre-treatment or incubation time and requires about 12 minutes for complete assay including 3 minutes for the sample preparation. The comparison of the current bioelectrode with some recently reported CRP sensors

(Table 3.3) shows its improved performance in terms of linear range of detection [28-30], assay time [31, 32] and sensitivity [33].

**Table 3.3:** Comparison of analytical performance of electrochemical sensors for Ag- $\alpha$ CRP

Electrochemical sensor type	Transduction platform	Linear range	Limit of Detection (LOD)	References
EIS	SAM/Au electrode	60 ng mL <sup>-1</sup> to 6.0 $\mu$ g mL <sup>-1</sup>	19 ng mL <sup>-1</sup>	[28]
EIS	Ab-BSA /Au-NPs/Cyst/Au electrode	5 to 25 $\mu$ g mL <sup>-1</sup>	-	[34]
Capacitance	interdigitated Au electrodes on nanocrystalline diamond surface	25 to 800 ng mL <sup>-1</sup>	-	[30]
square-wave anodic stripping voltammetry	poly(dimethylsiloxane)-Au nanoparticle	0.5 to 200 ng mL <sup>-1</sup>	307 amol in 30- $\mu$ L samples	[31]
EIS	NHS/MUA/MPA/Au electrode	45 ng mL <sup>-1</sup> to 5.84 $\mu$ g mL <sup>-1</sup>	30 ng mL <sup>-1</sup>	[33]
EIS	Pt(MPA)NPs-PPy/ITO-glass	10 to 10,000 ng mL <sup>-1</sup>	4.54 ng mL <sup>-1</sup>	Present work

The reproducibility of the bioelectrode for Ag- $\alpha$ CRP was investigated with inter-assay precision. The inter-assay precision was estimated for Ag- $\alpha$ CRP levels with three bioelectrodes prepared independently under similar experimental conditions. The inter-

assay variation coefficient, as estimated was found to be a minimum of about 1.4% and a maximum of about 15 % over a range of  $0.01 \mu\text{g mL}^{-1}$  to  $10 \mu\text{g mL}^{-1}$  of Ag- $\alpha$ CRP, as depicted by error bar in Fig. 3.10, indicating an acceptable precision and fabrication reproducibility. The stability of the bioelectrode was examined by repeatedly carrying out the impedimetric response measurements on the bioelectrode for the same sample of Ag- $\alpha$ CRP under identical conditions and it was found that no significant change in  $R_{\text{et}}$  was observed even after 5 repeated impedance measurements. This indicates that the bioelectrode retains its biocompatible property both in the solution and in open as well. The nonspecific adsorption is one of the major problems in immunosensing. The specificity of the bioelectrode was examined by carrying out the impedance measurement with non-specific protein antigen, mouse immunoglobulin-G (Ag-IgG) over a concentration range of  $0.01 \mu\text{g mL}^{-1}$  to  $10 \mu\text{g mL}^{-1}$  under identical conditions. Since no significant changes were found in the  $R_{\text{et}}$  values with the added aliquots of the increasing concentration of IgG with respect to the control sample without IgG, it may be concluded that non-specific interactions, if any, plays either negligible or insignificant role on the evaluation of EIS spectra using this bioelectrode.

### 3.4 Conclusion

This work demonstrates a facile in-situ electrochemical synthesis of functionalized Pt NPs intercalated conducting polypyrrole nanocomposite film deposited over an ITO-glass. The work also demonstrates the utility of combining the two types of advanced materials with complementary properties, organic conducting polymers and inorganic

nanoparticles, to construct a bioelectrode for the detection of protein antigen, Ag- $\alpha$ CRP. The protein, Ab- $\alpha$ CRP, has been covalently immobilized on the biocompatible Pt(MPA)NPs-PPy nanocomposite, which provides a high protein loading capacity with site-specific protein bindings. The long chain of PPy in the polymer composite acts as a spacer between the biomolecules and the transducer, wherein the Pt nanoparticles helps in preserving the native protein conformation and reducing the steric hindrance for better probe orientation and accessibility of the biomolecules to the analyte. This high protein loading together with a fine probe orientation on the electroactive Pt leads to the construction of a highly specific and sensitive bioelectrode exhibiting a wide linear range of Ag- $\alpha$ CRP detection from  $10 \text{ ng mL}^{-1}$  to  $10 \text{ }\mu\text{g mL}^{-1}$  with a  $R_{\text{ct}}$  sensitivity of  $109.74 \text{ }\Omega \text{ cm}^2$  per decade. Though this device protocol shows a better performance for the detection of Ag- $\alpha$ CRP in PBS in comparison to a few recently reported sensors, under identical conditions, in terms of dynamic detection range, sensitivity and specificity, this can further be optimized with blood serum samples for clinical applications in real practice.

### 3.5 References

1. R. V Mundra, X. Wu, J. Sauer, J. S Dordick and R. S Kane, *Curr. Opin. Biotechnol.* 28 (2014) 25.
2. L. Hou, Z. Gao, M. Xu, X. Cao, X. Wu, G. Chen and D. Tang, *Biosens. Bioelectron.* 54 (2014) 365.
3. I-T. Liu, M-H. Hon and L.G.Teoh, *Ceram. Int.* 40 (2014) 4019.
4. J. Wang, *Anal. Chim. Acta* 500 (2003) 247.
5. N.L. Rosi and C.A. Mirkin, *Chem. Rev.* 105 (2005) 1547.
6. R.J. Tseng, J. Huang, J. Ouyang, R.B. Kaner and Y. Yang, *Nano Lett.* 5 (2005) 1077.
7. M. Xue , X. Ma , Z. Xie , L. Duan , Y. Jiang , M. Zhang and T. Cao , *Chem. Asian J.* 5 (2010) 2266.
8. R. Devi and C.S. Pundir, *Sens. Actuators, B* 193 (2014) 608.
9. B.C. Kim, C.O. Too, J.S. Kwon, J.M. Ko and G.G. Wallace, *Synth. Met.* 161 (2011) 1130.
10. B. Domènech, K. K Ziegler, F. Carrillo, M. Muñoz, D. N Muraviev and Jorge Macanás, *Nanoscale Res. Lett.* 8 (2013) 238.
11. J. Gong, L. Wang and L. Zhang, *Biosens. Bioelectron.* 24 (2009) 2285.
12. X. Yang, L. Li and F. Yan, *Sens. Actuators, B* 145 (2010) 495.
13. V. Saumya and T. P. Rao, *Anal. Methods* 4 (2012) 1976.
14. A. Chen and P. H-Hindle, *Chem. Rev.* 110 (2010) 3767.
15. Y. Yu, Q. Sun, T. Zhou, M. Zhu, L. Jin and G. Shi, *Bioelectrochemistry* 81 (2011) 53.

16. M. Ahmad, C. Pan, L. Gan, Z. Nawaz and J. Zhu, *J. Phys. Chem. C* 114 (2010) 243.
17. W.P. Hu, H.Y. Hsu, A. Chiou, K.Y. Tseng, H.Y. Lin, G.L. Chang and S.J. Chen, *Biosens. Bioelectron.* 21 (2006) 1631.
18. M.H. Meyer, M. Hartmann and M. Keusgen, *Biosens. Bioelectron.* 21 (2006) 1987.
19. P. R. V. Rhee, M. J. McKelvy and W. S. Glaunsinger, *J. Solid State Chem.* 67 (1987) 151.
20. S. Xing and G. Zhao, *Mater. Lett.* 61 (2007) 2040.
21. L. Yang and Y. Li, *Biosens. Bioelectron.* 20 (2005) 1407.
22. F. Yakuphanoglu, I.S. Yahia, B.F. Senkal, G.B. Sakr and W.A. Farooq, *Synth. Met.* 161 (2011) 817.
23. A.D. Chowdhury, A. De, C. R. Chaudhuri, K. Bandyopadhyay and P. Sen, *Sens. Actuators, B* 171 (2012) 916.
24. S.J. Ding, B.W. Chang, C.C. Wu, M.F. Lai and H.C. Chang, *Electrochim. Acta* 50 (2005) 3660.
25. T. J. Davies, C. E. Banks and R. G. Compton, *J. Solid State Electrochem.* 9 (2005) 797.
26. R. G. Compton and C. E. Banks, "Understanding Voltammetry", World Scientific, London, 2007.
27. S.A. Mamuru and K.I. Ozoemena, *Electroanalysis* 22 (2010) 985.
28. T. Bryan, X. Luo, P.R. Bueno and J.J. Davis, *Biosens. Bioelectron.* 39 (2013) 94.
29. W. Zhan and A.J. Bard, *Anal. Chem.* 79 (2007) 459.

30. A. Quershi, Y. Gurbuz, W. P. Kang and J. L. Davidson, *Biosens. Bioelectron.* 25 (2009) 877.
31. F. Zhou, M. Lu, W. Wang, Z.P. Bian, J.R. Zhang and J.J. Zhu, *Clin. Chem.* 56 (2010) 1701.
32. N. Gan, L. Wang, H. Zhou, T. Li, W. Sang, F. Hu and Y. Cao, *Int. J. Electrochem.* 7 (2012) 11564.
33. N. Puri, V. K. Tanwar, V. Sharma, T. Ahuja, A.M. Biradar and Rajesh, *IJIB* 9 (2010) 1.
34. J.J. Zhu, J.Z. Xu, J.T. He, Y.J. Wang, Q. Miao and H.Y. Chen, *Anal. Lett.* 36 (2003) 1547.

## CHAPTER 4

### Protein Functionalized ZnS nanoparticles-Silane composite based bioelectrode

*In this work ZnS(MPA) nanoparticles are covalently attached to a self assembled monolayer (SAM) of 3-aminopropyl triethoxysilane (APTES) on an ITO coated glass plate. The protein antibody, anti-Myoglobin (Ab-Mb), are covalently linked to free carboxyl groups present on ZnS(MPA) nanoparticles via carbodiimide coupling reaction to form a bioelectrode (Ab-Mb(BSA)/ZnS(MPA)/APTES/ITO-glass). This bioelectrode has been characterized using AFM, contact angle measurements, cyclic voltammetry and EIS. The optimal equivalent circuit model that matches the impedimetric responses of the bioelectrode describes three distinct regions: the electrolyte solution resistance ( $R_s$ ), the double layer capacitance ( $C_{dl}$ ) and the specific charge transfer resistance ( $R_{et}$ ). The EIS measurements revealed that the  $R_{et}$  increases considerably with no significant change in  $C_{dl}$  after immunoreaction with protein specific antigen myoglobin, Ag-Mb, so that the prepared bioelectrode can be used for the detection of Ag-Mb. The bioelectrode exhibits an electrochemical impedance response to Ag-Mb, in a linear range from  $10 \text{ ng mL}^{-1}$  to  $1 \text{ } \mu\text{g mL}^{-1}$  phosphate buffer solution (pH 7.4) with a  $R_{et}$  sensitivity of  $117.36 \text{ } \Omega \text{ cm}^2$  per decade.*



## 4.1 Introduction

Metal and semiconductor nanoparticles in the size range of 2–10 nm are of considerable interest, due to their dimensional similarities with biological macromolecules (e.g. nucleic acids and proteins). Gold nanoparticles, silica nanoparticles and semiconductor nanoparticles (CdS, PbS, ZnS) are used in electrochemical immunosensors in order to immobilize antibodies and to enhance the sensor performance [1–3]. Recent advances in semiconductor nanoparticles have led to their large scale preparation owing to their strong size-dependent properties, excellent chemical processibilities, large specific surface area, and ease of preparation. ZnS is an important semiconducting material with numerous applications in sensors [4, 5], electroluminescence [6, 7] and biodevices [8,9]. The water-soluble ZnS nanoparticles coated with different capping agents can permit greater affinity to bind or interact with biotarget molecules [10].

Myoglobin (Mb) is a heme-containing protein found in all muscle cells: smooth, skeletal, and cardiac. Recently metal particle-enhanced fluorescence on silver island films for myoglobin immunoassay has been reported [11]. However, this method is disadvantageous due to the non-homogeneous nature of the silver island film and significant deviation in results, making it difficult to use as analytical method for myoglobin detection. Recently a review article providing a brief overview of electrochemical sensors for the detection of cardiac biomarkers is reported [12]. Suprun et al. have reported an electrochemical immunosensor based on metal nanoparticles (gold, silver, and copper) for cardiac myoglobin detection in human blood plasma [13, 14]. Although the method does not require signal enhancement or amplification, the

electrode needs a 15 min immunoreaction time with the target Mb sample, followed by further 5 min incubation in PBS and washing of nonspecifically binding molecules before electrochemical measurement [14]. Pakapongpan et al. [15] have reported electrochemical sensors for hemoglobin and Mb based on methylene blue-multiwalled carbon nanotubes nanohybrid modified glassy carbon electrode. This electrochemical sensor is based on direct electrochemical reduction of Mb at the electrode surface with a wide range of [Mb] detection without going through an immunoreaction and hence does not require any specific reagent and antibody molecules. However, the wide linear range of [Mb] detection from 0.1  $\mu\text{M}$  to 3.0  $\mu\text{M}$  ( $\sim 1.78 \mu\text{g mL}^{-1}$  to  $53.40 \mu\text{g mL}^{-1}$ ) is out of the physiological range of [Mb] in human blood serum and would require a sample dilution for low [Mb] detection. Billah et al. [16] used a mixed self assembled monolayer (SAM) of alkanethiols and phospholipid based immunosensor for the detection of Mb. The Mb detection range of the sensor was found to be  $10^{-2}$ – $10^{-6}$  M. However, the fabrication of the immunosensor is not cost effective as it requires the use of an expensive biotin functionalized Mb antibody immobilized at the transducer surface. We have also reported earlier an electrochemical immunosensor based on a thin flat gold wire with a mixed SAM of a small and a long chain alkanethiol for Mb detection [17]. However, in order to enhance the stability and loading of the antibody molecules at the transducer surface, we have utilized high surface area ZnS nanoparticles as protein immobilizing conjugates, in the present work, for Mb detection.

In this chapter, we report the synthesis of ZnS(MPA) nanoparticles and their covalent attachment to SAM of APTES on ITO-glass plates. These ZnS(MPA) modified

ITO-glass plates were subsequently immobilized with the protein antibody, Ab-Mb, through free carboxyl groups available on ZnS(MPA) nanoparticles by using N-(3-dimethylaminopropyl)-N'-ethyl carbodiimide hydrochloride (EDC)/N-hydroxy Succinimide (NHS) approach, for the fabrication of a bioelectrode (Ab-Mb(BSA)/ZnS(MPA)/APTES/ITO-glass). The bioelectrode was systematically characterized by spectroscopic techniques and its immunosensing characteristic towards the quantitative estimation of the protein antigen, Ag-Mb, concentration was investigated by EIS using  $[\text{Fe}(\text{CN})_6]^{3-/4-}$  as a redox probe.

## 4.2 Experimental

### 4.2.1 Reagents

Ab-Mb (Cat4M2 MAb 4E2) and Ag-Mb (Cat 8M50) were obtained from Hytest (Turku, Finland). APTES was purchased from Merck Chemicals (Germany). EDC, NHS, zinc nitrate hexahydrate ( $\text{Zn}(\text{NO}_3)_2 \cdot 6\text{H}_2\text{O}$ ), sodium sulfide nonahydrate ( $\text{Na}_2\text{S} \cdot 9\text{H}_2\text{O}$ ) and 3-mercaptopropionic acid (MPA) were obtained from Sigma-Aldrich Corp. All the chemicals used were as purchased without further purification.

### 4.2.2 Equipments

Contact angles were recorded on a drop shape analysis system; model DSA10MK2 from Krüss GmbH, Germany. The contact angle measurements were made by using five drops of ultra pure water at different regions of the electrode surface and an average value of these measurements was used for the calculation and comparison of different samples. TEM images were taken on a high resolution TM model Technai G2F30 S Twin, The

Netherlands. The XRD pattern was recorded using a Bruker AXS Advance D8 powder X-ray diffractometer. AFM images were obtained on a VEECO/DICP2, USA scanning probe microscope. Cyclic voltammetry and EIS measurements were done on a PGSTAT302N, AUTOLAB instrument from Eco Chemie, The Netherlands.

#### 4.2.3 Microstructural characterization of ZnS(MPA) nanoparticles

The aqueous ZnS(MPA) nanoparticles were synthesized, at room temperature, by method as reported earlier [18] and described in chapter 2. The nano-crystallite size and structure of the ZnS(MPA) so prepared was determined by using the X-ray powder diffraction method (Fig. 4.1).

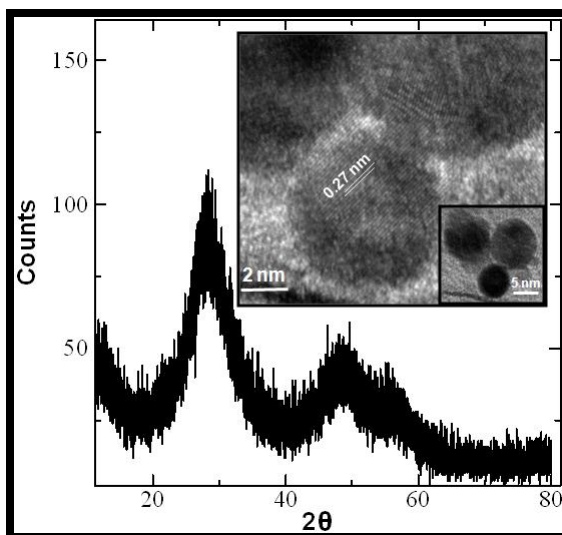


**Fig. 4.1:** XRD pattern of the ZnS(MPA) nanoparticles; Inset: TEM micrograph of the ZnS(MPA) nanoparticles.

The powder sample was prepared by precipitating out the nanoparticles from the colloidal suspension of ZnS(MPA) nanoparticles by adding ethanol, followed by centrifugation and air-drying, at room temperature. The XRD data indicates that the

ZnS(MPA) nanoparticles exhibited a cubic structure with a lattice constant of  $a=b=c=5.34 \text{ \AA}$ . The observed broad peak at  $2\theta=28.91^\circ$  corresponds to the (111) plane of the zinc blend type structure. The crystallite size (D) of the ZnS(MPA) nanoparticles estimated by Scherrer's equation  $D=0.89\lambda/\beta \cos\theta$  was found to be 5.23 nm, where  $\lambda$  is the wavelength of X-ray (0.1541 nm),  $\beta$  is the width at half maximum of the diffraction peak (FWHM), and  $\theta$  is the diffraction angle.

A TEM micrograph of the ZnS(MPA) nanoparticles is shown in Fig. 4.1 (inset). It indicates that the particles are spherical in shape having 5 to 8 nm diameter size range with agglomeration at some places. They have clear boundaries with an interplanar spacing value of 0.27 nm. The clear lattice fringes indicate a highly crystalline structure of the ZnS(MPA) nanoparticles.

#### *4.2.4 Preparation of bioelectrode*

The ITO coated glass plates ( $0.5 \times 0.5 \text{ cm}^2$ ) were cleaned sequentially in the order of ultrasonic cleaning in acetone, ethanol, and distilled water for 10 min each, and dried. Then it was exposed to oxygen plasma in a plasma chamber for 5 min to increase the number of hydroxyl groups on the ITO-glass surface. The pre-cleaned ITO-glass plates were immersed in 2% APTES solution prepared in ethanol for 1.5 h, under ambient conditions, to form a SAM of APTES and were rinsed with ethanol to remove any unbound APTES molecules and dried under  $\text{N}_2$  gas flow. These plates were then immersed in a 5 mL solution of 30 mM ZnS(MPA) nanoparticles containing 30 mM NHS and 150 mM EDC, for 3 h, followed by washing with double distilled water and dried under  $\text{N}_2$  gas flow. Finally, the protein antibody (Ab-Mb) was immobilized onto

these modified electrodes (ZnS(MPA)/APTES/ITO-glass) by treating them with a PBS buffer (pH 7.4) containing  $100 \mu\text{g mL}^{-1}$  Ab-Mb, for an overnight period at  $4 \text{ }^\circ\text{C}$ , followed by washing with PBS and drying with  $\text{N}_2$  gas flow. These protein antibody immobilized electrodes were then incubated in 1% BSA solution, for 30 min to block the nonspecific binding sites and unbound free carboxyl groups, if any, on the electrode surface, followed by washing with PBS to remove any physically adsorbed antibodies and dried under  $\text{N}_2$  flow. The stepwise fabrication of the bioelectrode is shown in Fig. 4.2.

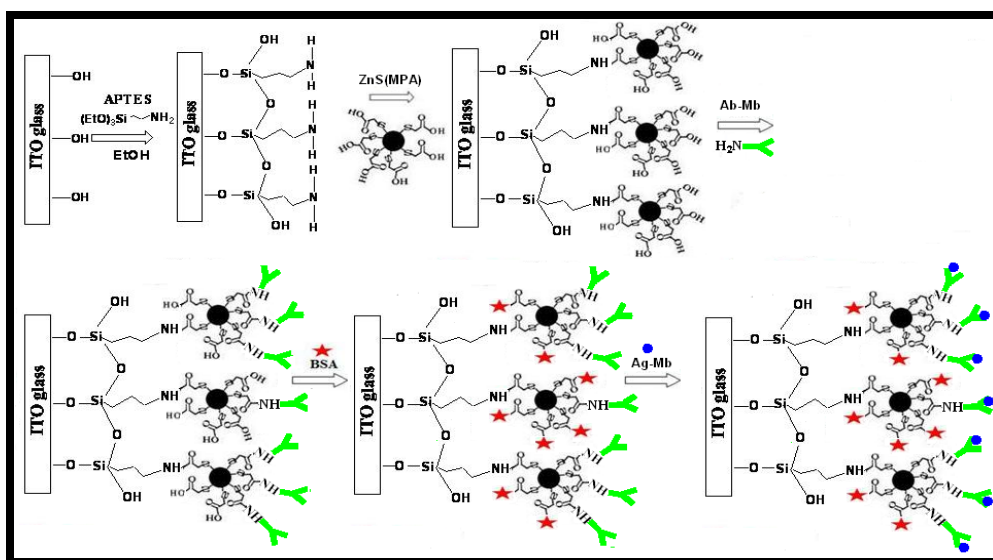


*Fig. 4.2: Schematic representation of the stepwise fabrication of the bioelectrode*

## 4.3 Results and discussion

### 4.3.1 Contact angle measurement

Contact angle measurements were conducted to investigate the hydrophilic/hydrophobic nature of the electrode surface before and after each step of surface modification by the

static sessile drop method and is shown in Fig.4.3. The drop image was stored and an image analysis system calculated the contact angle ( $\theta$ ) from the shape of the drop. A low contact angle of  $39.92^\circ \pm 2^\circ$  (Fig. 4.3a) initially obtained for the bare ITO-glass plate corresponds to surface hydrophilic hydroxyl groups.

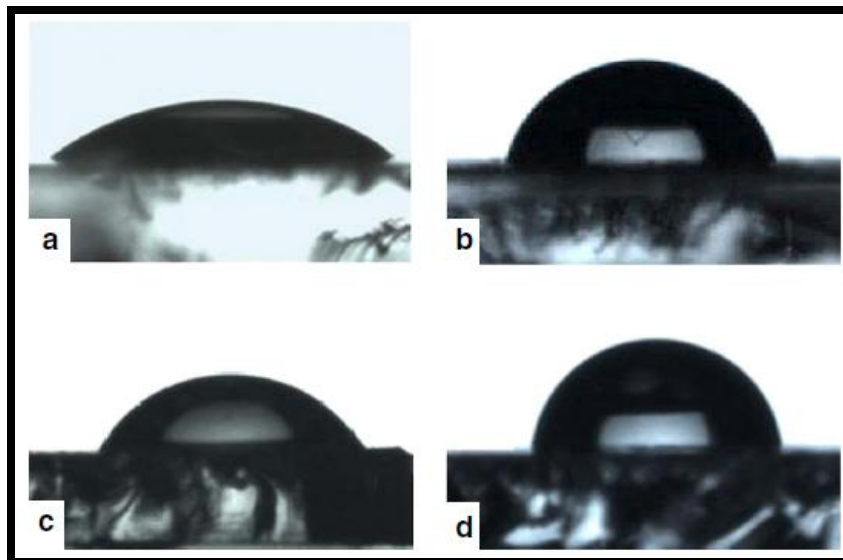


**Fig. 4.3:** Contact angle measurement images of the (a) ITO-glass plate; (b) APTES/ITO-glass; (c) ZnS(MPA)/APTES/ITO-glass; (d) Ab-Mb/ZnS(MPA)/APTES/ITO-glass

The contact angle increases to  $73.52^\circ \pm 1^\circ$  (Fig. 4.3b) for the APTES modified ITO-glass due to the presence of hydrophobic alkyl chains of APTES molecules that decrease the surface energy by drastically reducing the hydroxyl groups of the bare ITO-glass on silanization. A contact angle of  $61.68^\circ \pm 2^\circ$  (Fig. 4.3c) was obtained for the ZnS(MPA) nanoparticles modified APTES/ITO-glass surface, where free carboxyl groups available on the ZnS(MPA) nanoparticles induce the hydrophilic character to the modified surface. However, the contact angle increased to  $85.15^\circ \pm 2^\circ$  (Fig. 4.3d) after the covalent immobilization of the protein antibody, Ab-Mb, on the surface of the

ZnS(MPA)/APTES/ITO-glass, due to the hydrophobic nature of the protein molecules, thereby indicating the formation of the bioelectrode (Ab-Mb/ZnS(MPA)/APTES/ITO-glass).

#### 4.3.2 Microstructural characterization

The surface topologies of the modified electrodes were imaged using AFM in non-contact mode (Fig. 4.4).

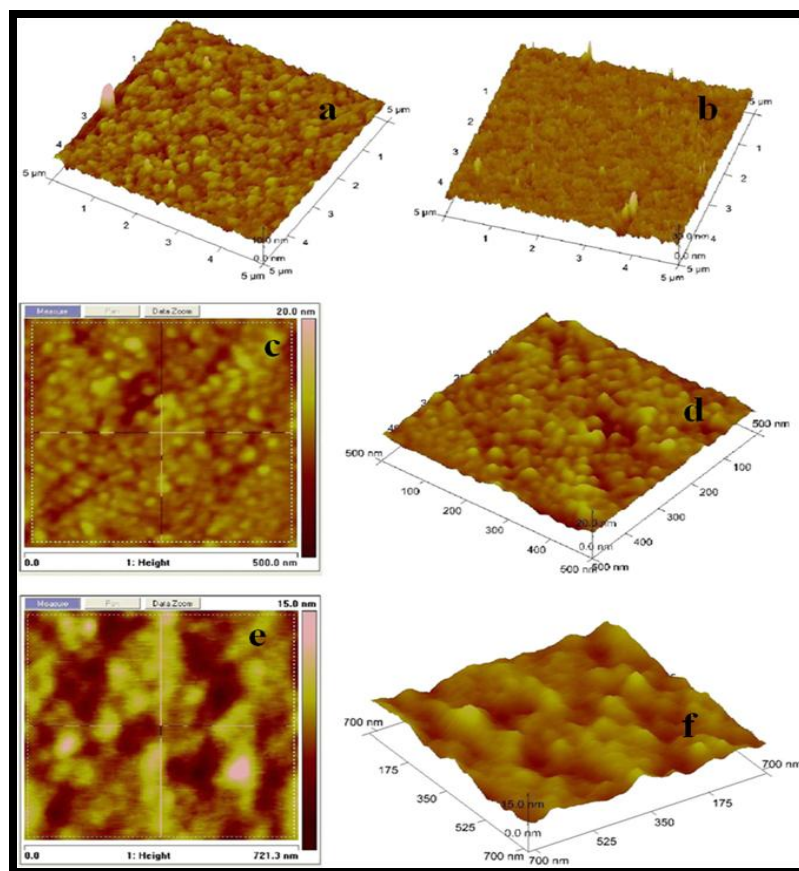


**Fig. 4.4:** (a) 3D AFM image of the APTES/ITO-glass; (b) 3D AFM image of the ZnS(MPA)/APTES/ITO-glass; (c) and (d) 2D and 3D AFM images of the magnified ZnS(MPA)/APTES/ITO-glass; (e) and (f) 2D and 3D AFM images of the Ab-Mb/ZnS(MPA)/APTES/ITO-glass.



The surface roughness parameter ( $R_a$ ) was used to characterize the surface in terms of irregularity and height distribution. The AFM image of APTES/ITO-glass surface (Fig. 4.4a) indicates a regular island-like structure with an average  $R_a$  value of 0.483 nm. This on surface modification with ZnS(MPA) nanoparticles exhibits a dense, grainy asymmetrical surface (Fig. 4.4b) with an increased  $R_a$  value of 1.72 nm. At a higher magnification, the 2D and 3D AFM images of the ZnS(MPA)/APTES/ITO-glass electrode (Fig. 4.4c and d) suggest the agglomeration of the grained size particles of the ZnS(MPA) at certain places on the electrode surface. However, the AFM images (Fig. 4.4 e and f) show a completely changed morphology upon protein Ab-Mb immobilization with a decreased  $R_a$  value of 1.46 nm, exhibiting a comparatively much bigger and globular feature of the protein nature [19] with smooth surface characteristic with respect to the ZnS(MPA)/APTES/ITO-glass.

#### *4.3.3 Electrochemical characterization of the bioelectrode*

Each step of surface modification of the ITO-glass plate and antibody immobilization was monitored by cyclic voltammetry using an  $[\text{Fe}(\text{CN})_6]^{3-/4-}$  mixture in a PBS solution of pH 7.4 containing 0.1 M KCl as a redox probe. Fig. 4.5 shows the CV spectra of both before and after each step of the surface modification of the electrode and subsequent protein, Ab-Mb immobilization leading to the formation of the Ab-Mb(BSA)/ZnS(MPA)/APTES/ITO-glass electrode.

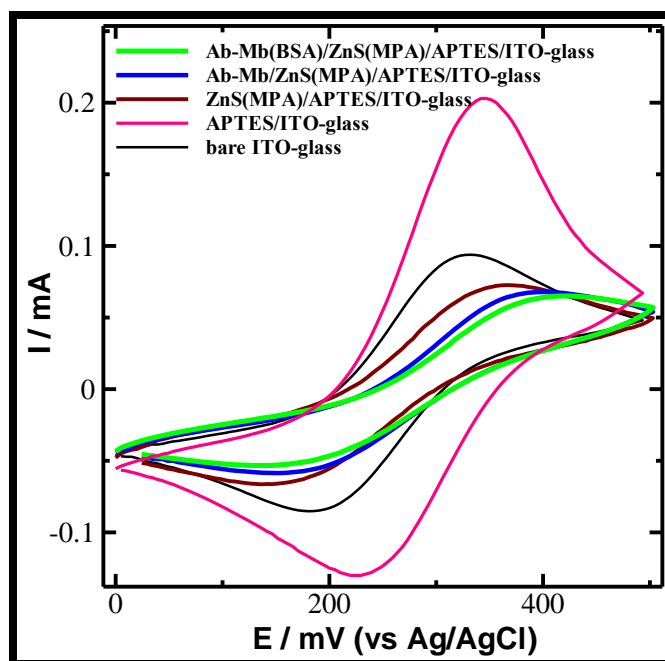


**Fig. 4.5:** CV of the bare ITO glass; APTES/ITO-glass; ZnS(MPA)/APTES/ITO-glass; Ab-Mb/ZnS(MPA)/APTES/ITO-glass and Ab-Mb(BSA)/ZnS(MPA)/APTES /ITO-glass in PBS (pH 7.4, 0.1 M KCl) containing 2 mM  $[\text{Fe}(\text{CN})_6]^{3-/4-}$ ; 3rd cycle of CV is shown.

In each CV only the 3rd cycle was considered as no major changes were seen in the subsequent cycles. A quasi-reversible CV with a peak-to-peak separation between the oxidation and reduction potentials ( $\Delta E_p$ ) of 122 mV was observed for the bare ITO-glass electrode. This after modification by SAM of APTES decreased to a  $\Delta E_p$  value of 98 mV and the cathodic and anodic peak currents were comparatively increased with respect to the bare ITO-glass electrode. These changes are attributed to an increased interfacial concentration of the anionic probes ( $[\text{Fe}(\text{CN})_6]^{3-/4-}$ ) due to its strong affinity towards the polycationic ( $\text{NH}_3^+$ ) layer of the amino groups of the APTES [20]. However, a contrary result of a decreased peak current and an increased peak potential (Table 4.1) were obtained in the case of the ZnS(MPA) modified APTES/ITO-glass electrode. This may

be due to the semiconducting behavior of ZnS(MPA), as well as the repulsive interaction between the  $\text{COO}^-$  groups of ZnS(MPA) and the anionic probe  $[\text{Fe}(\text{CN})_6]^{3-/4-}$  at the electrode surface interface. The CV peak current further decreases with the immobilization of the protein Ab-Mb on the surface of the ZnS(MPA)/APTES/ITO-glass electrode and also after the treatment with a blocking protein, BSA. This may be attributed to the formation of a protein antibody layer on the electrode, which acts as the electron communication and mass-transfer blocking layer, thereby hindering the access of redox probe towards the electrode surface significantly.

Electrochemical transformations occurring at the electrode/electrolyte interface can be modeled by extracting components of the electronic equivalent circuits that correspond to the experimental impedance spectra. The general Randles electronic equivalent circuit [21] is shown in the inset of Fig. 4.6a. The  $R_{\text{et}}$  values of the modified electrodes are listed in Table 4.1. The bare ITO-glass shows a  $R_{\text{et}}$  value of  $80.75 \Omega \text{ cm}^2$ , which sharply reduces to  $22.65 \Omega \text{ cm}^2$  for the APTES/ITO-glass indicating an easy electronic transport at the electrode surface interface. The increased  $R_{\text{et}}$  values of  $197.25 \Omega \text{ cm}^2$  and  $256.25 \Omega \text{ cm}^2$  for the ZnS(MPA)/APTES/ITO-glass and protein Ab-Mb immobilized Ab-Mb(BSA)/ZnS (MPA)/APTES/ITO glass, respectively, reflects the charge repulsive property of the carboxyl functional groups of ZnS(MPA) and the insulating nature of the protein molecules at the electrode surface. These results are complementary to cyclic voltammetry measurements, further confirming the fabrication of the bioelectrode. These changes in the electrochemical parameters are more

pronounced in the bode plot (Fig. 4.6b) and a phase angle of  $-53^\circ$  (close to  $-45^\circ$ ) obtained for the bioelectrode shows a diffusion-controlled process.

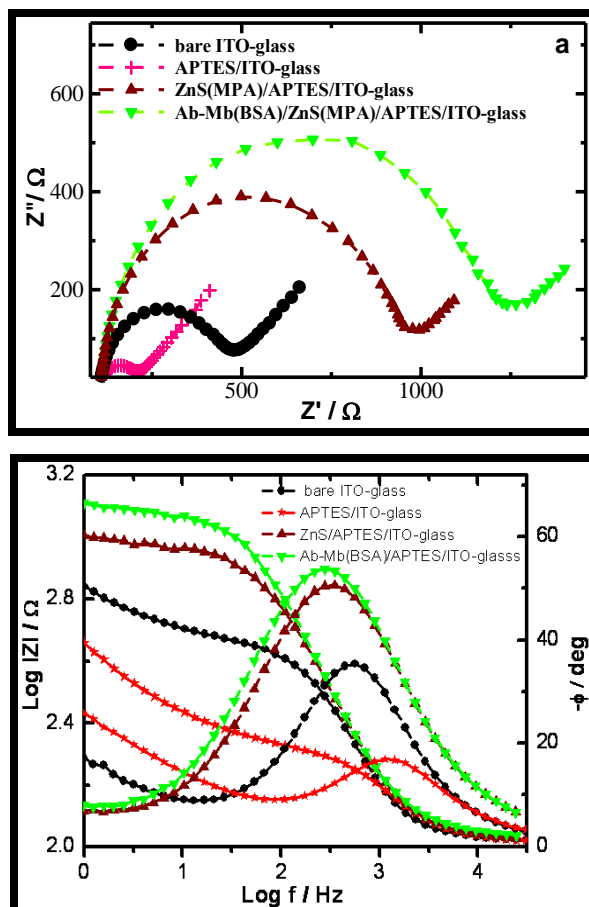


**Fig. 4.6:** (a) Nyquist plots obtained on the bare ITO-glass, APTES/ITO-glass, ZnS(MPA)/APTES/ITO-glass and Ab-Mb(BSA)/ZnS(MPA)/APTES/ITO-glass in PBS (pH 7.4) containing  $2 \text{ mM } [\text{Fe}(\text{CN})_6]^{3-/4-}$  (b) Corresponding Bode plots.

The bioelectrode was further characterized by analyzing the following important parameters:  $C_{dl}$ , the heterogeneous electron transfer rate constant ( $k^0$ ) and the time constant ( $\tau$ ) for the applied redox probe. These parameters not only allow us to follow the interfacial interactions of biomolecules, but they also help in the characterization of the structural features of the sensing interface and for explaining the mechanisms of

chemical processes occurring at the electrode/solution interfaces [22]. The corresponding  $k^0$  of the modified electrodes was calculated by using charge transfer kinetics [Eqn. 4.1]:

$$k^0 = RT/n^2F^2A R_{et} C \quad (4.1)$$

where  $R$  is the gas constant,  $T$  is the temperature,  $n$  is the electron transferring constant of the redox couple,  $F$  is Faraday constant,  $A$  is the area of the electrode, and  $C$  is the concentration of the redox couple in the bulk solution. The  $k^0$  value of the APTES modified ITO-glass electrode is approximately four times higher than that for bare ITO-glass, indicating a faster electron exchange between the redox probe and the electrode after the formation of the APTES SAM on the ITO-glass electrode. The  $k^0$  values on subsequent attachment of ZnS(MPA) on the APTES/ITO-glass and protein Ab-Mb immobilization on the ZnS(MPA)/APTES/ITO-glass shows a sluggish electron charge transfer rate constant resulting in the generation of low capacitance at the electrode surface (Table 4.1).

The time constant ( $\tau$ ) for the corresponding charge transfer process was calculated from the maximum frequency value,  $\omega_{max}$  ( $=2\pi f$ ), in which the semicircle draws a maximum in the imaginary axis by using Eqn. (4.2):

$$\tau = 1/\omega_{max} = R_{et}C_{dl} \quad (4.2)$$

The noticeable high value of time constant with low pseudo capacitance and sluggish electron transfer rate constant obtained for the protein immobilized Ab-Mb/ZnS(MPA)/APTES/ITO-glass electrode due to the slow diffusion of

$[\text{Fe}(\text{CN})_6]^{3-/4-}$  ions at the electrode protein layer/solution interface, further validates the formation of the Ab-Mb/ZnS(MPA)/APTES/ITO-glass bioelectrode.

**Table 4.1:** CV & EIS parameters at various stages of surface modifications of the electrode

Type of Electrodes	$\Delta E_p$ (mV)	$R_{et}$ ( $\Omega\text{cm}^2$ )	$C_{dl}$ ( $\mu\text{Fcm}^{-2}$ )	$k^0$ ( $\text{ms}^{-1}$ ) ( $\times 10^{-4}$ )	$\tau$ (s) ( $\times 10^{-4}$ )	$Z_w$ ( $\Omega\text{cm}^2$ ) ( $\times 10^{-3}$ )
Bare ITO-glass	122	80.75	6.80	6.57	5.49	1.27
APTES/ ITO	98	22.65	7.18	23.44	1.62	1.58
ZnS(MPA)/APTES/ ITO	234	197.25	7.10	2.69	14.00	1.23
Ab-Mb/ZnS(MPA)/APTES/ ITO	298	256.25	6.88	2.07	17.64	1.04

#### 4.3.4 Surface coverage and nature of the bioelectrode

The surface coverage ( $\theta$ ), defined as the number of adsorbed molecules on a surface divided by the number of molecules in a filled monolayer on that surface, for ZnS(MPA) nanoparticles on the APTES/ITO-glass was calculated by using Eqn. (4.3):

$$\theta = 1 - R_{et1} / R_{et2} \quad (4.3)$$

where  $\theta$  represents the fraction of occupied binding sites and  $R_{et1}$  and  $R_{et2}$  represent the surface specific charge transfer resistances of APTES/ITO-glass and ZnS(MPA)/APTES/ITO-glass, respectively. The value of  $\theta$  was found to be 0.88, indicating a more than 88% surface coverage of the APTES/ITO-glass electrode by ZnS(MPA) nanoparticles.

To determine the nature of the redox process various CVs of the Ab-Mb/ZnS(MPA)/APTES/ITO-glass bioelectrode was carried out at different scan rates ( $v = 25\text{--}100 \text{ mV s}^{-1}$ ) in a PBS (pH 7.4, 0.1 M KCl) solution containing 2 mM  $[\text{Fe}(\text{CN})_6]^{3-/4-}$  (Fig. 4.7). The inset of Fig. 4.7 shows the plots of the anodic ( $I_{\text{pa}}$ ) and cathodic peak currents ( $I_{\text{pc}}$ ) versus the square root of the scan rates ( $v^{1/2}$ ). The redox peak current showed a linear relationship with  $v^{1/2}$  which can be expressed by Eqn. (4.4):

$$I_{\text{pa}} (v^{1/2}) = b v^{1/2} + 23.62 \quad (4.4)$$

where slope  $b=2.55\pm 0.02$  having a correlation coefficient of 0.988, suggesting a diffusion controlled process occurring at the bioelectrode surface.

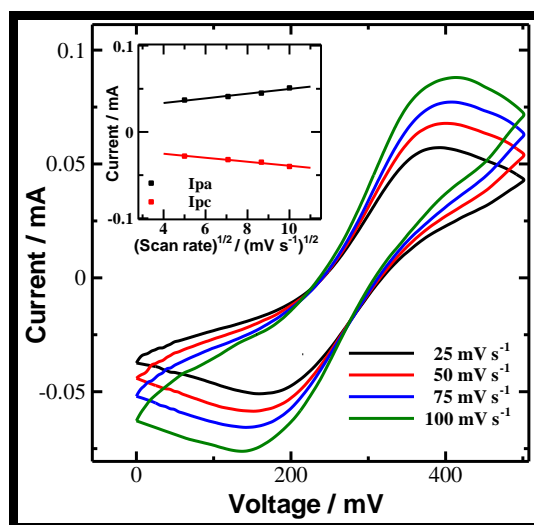


**Fig. 4.7:** CV of bioelectrode as a function of scan rate in PBS (pH 7.4) containing 2mM  $[\text{Fe}(\text{CN})_6]^{3-/4-}$ ; Inset: plot of redox peak current vs  $v^{1/2}$ .

#### 4.3.5 Electrochemical impedance response to protein antigen

Electrochemical impedance response studies of the bioelectrode to protein antigen, Ag-Mb, was carried out in a 0.1 M KCl solution containing 2 mM  $[\text{Fe}(\text{CN})_6]^{3-}/[\text{Fe}(\text{CN})_6]^{4-}$

(pH 7.4), at the scanning frequencies from 1.0 Hz to 10 kHz. The measurement was conducted in a sample solution containing no protein antigen, Ag-Mb, and the corresponding electron transfer resistance observed in a Nyquist plot was taken as a control sample response. Subsequently, electron-transfer resistances with other related EIS parameters were measured for the detection of antibody–antigen immunoreaction after the successive addition of the aliquots of different concentrations of protein antigen, Ag-Mb solution (Table 4. 2).

**Table 4.2:** EIS characteristic parameters of the bioelectrode upon immunoreaction

Concentration of Ag-Mb	$R_{et}$ ( $\Omega\text{cm}^2$ )	$C_{dl}$ ( $\mu\text{Fcm}^{-2}$ )	$k^0$ ( $\text{ms}^{-1}$ ) ( $\times 10^{-4}$ )	$\tau$ (s) ( $\times 10^{-4}$ )	$Z_w$ ( $\Omega\text{cm}^2$ ) ( $\times 10^{-3}$ )
Control	256.25	6.88	2.07	17.64	1.04
0.01 $\mu\text{g mL}^{-1}$	317.50	6.80	1.67	21.60	0.93
0.05 $\mu\text{g mL}^{-1}$	383.75	6.75	1.38	25.91	0.72
0.10 $\mu\text{g mL}^{-1}$	444.75	6.68	1.19	29.70	0.58
0.50 $\mu\text{g mL}^{-1}$	510.75	6.64	1.03	33.93	0.43
1.00 $\mu\text{g mL}^{-1}$	550.75	6.63	0.96	36.52	0.40

The Nyquist plots of impedance spectra for different concentrations of antigen, Ag-Mb, solution at the bioelectrode are shown in Fig. 4.8a. An increase in the diameter of the Nyquist circle was observed with increasing concentration of added antigen, Ag-Mb, indicating an antibody–antigen interaction, at the electrode surface. This increase in the electron transfer resistance is due to a kinetic barrier for the electron transfer, which perturbed the interfacial electron transfer considerably at the electrode surface. The



impedance modulus Bode plot of the bioelectrode (Fig. 4.8b) demonstrates three distinct regions corresponding to the three types of elements in the equivalent circuit.

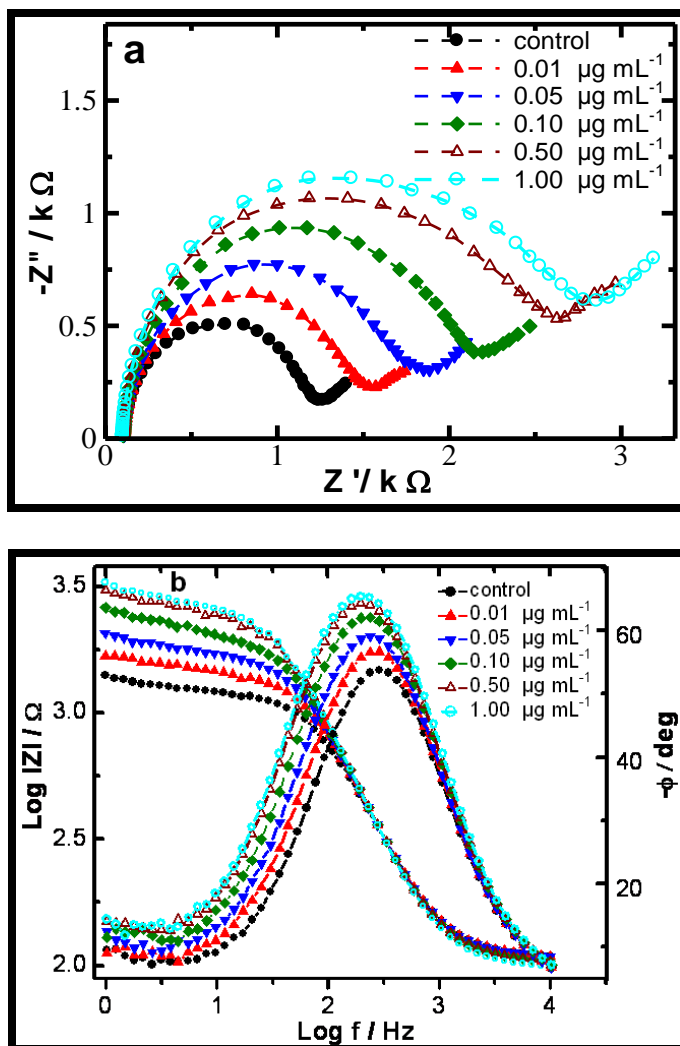


**Fig. 4.8:** (a) Nyquist plots obtained on bioelectrode for control and different concentration of Ag-Mb in PBS (pH 7.4); (b) Corresponding bode plots.

The double layer capacitance region is in the low frequency range from 50 Hz to 1 kHz, whereas the frequency region below 50 Hz and above 1 kHz corresponds to charge transfer resistance and solution resistance, respectively. It is interesting to note that in the

capacitance region of frequency, no significant change in  $C_{dl}$  values was observed on immunoreaction with different concentrations of protein antigen, Ag-Mb, showing a non capacitive behavior of the bioelectrode. However, at a frequency of less than 50 Hz impedance signal is dominated by the charge transfer resistance of the bioelectrode.

The Ab-Mb(BSA)/ZnS(MPA)/APTES/ITO-glass bioelectrode shows a well defined concentration dependence curve for the protein antigen, Ag-Mb. Fig. 4.9 shows a linear relationship between the change in specific electron charge transfer resistance ( $\Delta R_{et} = (R_{et})_{after\ immunoreaction} - (R_{et})_{control}$ ) and logarithmic value of Ag-Mb concentration in the range of  $10\text{ ng mL}^{-1}$  to  $1\text{ }\mu\text{g mL}^{-1}$  and is represented by Eqn. (4.5):

$$\Delta R_{et}(\log[\text{Ag-Mb}]) = b \log[\text{Ag-Mb}] + 293.22 \quad (4.5)$$

The  $R_{et}$  sensitivity (slope  $b$ ) of the bioelectrode from the calibration plot was found to be  $117.36\text{ }\Omega\text{ cm}^2/\text{decade}$  of the protein Ag-Mb concentration having a correlation coefficient of 0.994 ( $n=5$ ). Keeping in view, the physiological range of protein antigen Ag-Mb in the human body, the sensing behavior of the bioelectrode was studied only up to  $1\text{ }\mu\text{g mL}^{-1}$  antigen Ag-Mb concentration. However, the bioelectrode does not show any saturation even above  $1\text{ }\mu\text{g mL}^{-1}$  [Ag-Mb], providing a wider range of Mb detection at a low concentration region than the earlier reported sensors [15, 23, 24]. This is due to high loading of protein antibody molecules provided by the carboxyl functional groups surrounding the ZnS nanoparticles on the electrode surface, leading to increased immunoreaction with the target protein Ag-Mb. The stability of the Ab-Mb(BSA)/ZnS(MPA)/APTES/ITO-glass bioelectrode was also investigated and the results showed that, even after 10 continuous measurements, no measurable change in

the Nyquist plots could be observed, suggesting that the protein Ab-Mb was strongly bonded on the surface of the bioelectrode.

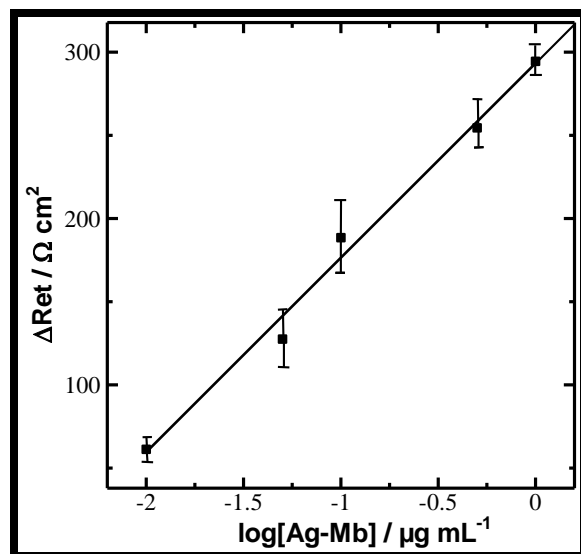


**Fig. 4.9:** Concentration dependent calibration curve of the bioelectrode; the error bars represent the standard deviation from three separate experiments.

#### 4.4 Conclusion

A comprehensive feature of a ZnS nanoparticles based bioelectrode, as a bioanalytical platform for immunosensor application has been described. In particular, carboxyl functionalized ZnS nanoparticles were covalently attached over the SAM of APTES on to the surface of the ITO-glass plate. These ZnS(MPA) nanoparticles showed good biocompatibility and also act as an effective conjugate to provide a sufficient amount of binding sites for the immobilization of protein Ab-Mb at the electrode surface for immunoreaction. High loading of protein Ab-Mb molecules at the bioelectrode surface due to higher surface area and conjugate binding sites of ZnS nanoparticles results to a

wider range of protein Ag-Mb detection from  $10 \text{ ng mL}^{-1}$  to  $1 \text{ }\mu\text{g mL}^{-1}$  in PBS. The EIS studies show a non capacitive behavior with a dominant electron charge transfer resistance characteristic of the bioelectrode surface after immunoreaction. This EIS characteristic of the bioelectrode surface may be found useful for future application in protein biomarker detection in a clinical sample after suitable optimization.

## 4.5 References

1. Y. An, X. Jiang, W. Bi, H. Chen, L. Jin, S. Zhang, C. Wang and W. Zhang, *Biosens. Bioelectron.* 32 (2012) 224.
2. X. Liu, Y. Zhang, J. Lei, Y. Xue, L. Cheng and H. Ju, *Anal. Chem.* 82 (2010) 7351.
3. K. Omidfar, H. Zarei, F. Gholizadeh and B. Larijani, *Anal. Biochem.* 421 (2012) 649.
4. N. Üzar, S. Okur and M.Ç. Arıkan, *Sens. Actuators A Phys.* 167 (2011) 188.
5. S.K. Mehta, Khushboo and A. Umar, *Talanta* 85 (2011) 2411.
6. S. Park, C. Jin, H.W. Kim and C. Lee, *J. Alloys Compd.* 509 (2011) 6262.
7. H. Ehrlich, T. Shcherba, M. Zhilenko and G. Lisichkin, *Mater. Lett.* 65 (2011) 107.
8. N. Chauhan, J. Narang and C.S. Pundir, *Biosens. Bioelectron.* 29 (2011) 82.
9. S. Raichlin, E. Sharon, R. Freeman, Y. Tzfati and I. Willner, *Biosens. Bioelectron.* 26 (2011) 4681.
10. S.K. Kailasa, K. Kiran and Hui-Fen Wu, *Anal. Chem.* 80 (2008) 9681.
11. E.G. Matveeva, Z. Gryczynski and J.R. Lakowicz, *J. Immunol. Methods* 302 (2005) 26.
12. M. Mohammed and M.P.Y. Desmulliez, *Lab on Chip* 11 (2011) 569.
13. E. Suprun, T. Bulko, A. Lisitsa, O. Gnedenko, A. Ivanov, V. Shumyantseva and A. Archakov, *Biosens. Bioelectron.* 25 (2010) 1694.
14. E.V. Suprun, A.L. Shilovskaya, A.V. Lisitsa, T.V. Bulko, V.V. Shumyantseva and A.I. Archakov, *Electroanalysis* 23 (2011) 1051.
15. S. Pakapongpan, R. Palangsantikul and W. Surareungchai, *Electrochim. Acta* 56 (2011) 6831.

16. M. Billah, H.C.W. Hays and P.A. Millner, *Microchim. Acta* 160 (2008) 447.
17. Rajesh, V. Sharma, V.K. Tanwar, S.K. Mishra and A.M. Biradar, *Thin Solid Films* 519 (2010) 1167.
18. S.K. Mishra, R. Pasricha, A.M. Biradar and Rajesh, *Appl. Phys. Lett.* 100 (2012) 053701.
19. L. Yang and Y. Li, *Biosens. Bioelectron.* 20 (2005) 1407.
20. J. Zhao, C.R. Bradbury, S. Huclova, I. Potapova, M. Carrara and D.J. Fermin, *J. Phys. Chem. B* 109 (2009) 22985.
21. G. Liua, J. Liu, T.P. Davis and J.J. Gooding, *Biosens. Bioelectron.* 26 (2011) 3660.
22. M. Gamero, F. Pariente, E. Lorenzo and C. Alonso, *Biosens. Bioelectron.* 25 (2010) 2038.
23. T.M. O'Regan, L.J. O'Riordan, M. Pravda, C.K. O'Sullivan and G.G. Guilbault, *Anal. Chim. Acta* 460 (2002) 141.
24. F. Darain, P. Yager, K.L. Gan and S.C. Tjin, *Biosens. Bioelectron.* 24 (2009) 1744.

## CHAPTER 5

---

### Protein functionalized Pt nanoparticles-silane composite based bioelectrode

---

*In this chapter myoglobin protein antibody was covalently immobilized with 3-Dimensional carboxyl functionalized Pt(MPA) nanoparticles deposited over an indium-tin-oxide coated glass plate via carbodiimide coupling reaction for the construction of a bioelectrode. This bioelectrode assembly was characterized by spectro/microscopic and electrochemical techniques. The Electrochemical impedance studies of the bioelectrode showed significant changes in charge transfer resistance ( $R_{et}$ ), predominantly at low ac frequency region of  $< 40$  Hz on immunoreaction with human cardiac myoglobin antigen (Ag-cMb) and exhibited a linear range of  $0.01 \mu\text{g mL}^{-1}$  to  $1 \mu\text{g mL}^{-1}$  Ag-cMb detection in phosphate buffer with a sensitivity of  $184.8 \Omega \text{ cm}^2$  per decade.*

## 5.1 Introduction

The recent advances in the field of nanotechnology have opened up research opportunities on materials with ultrafine nanostructures [1-4]. Recently, the amount of research on the biological applications of nanoparticles has increased with potential applications in the construction of electrochemical sensors and biosensors, where they function as “electron antennae” efficiently channeling electrons between the electrode and the electroactive species [5-6]. Platinum (Pt), one of the most researched noble metals, has extensive application in the field of electrochemical sensors as they can act as an effective matrix of biomolecules by taking advantage of their biocompatibility and huge surfaces of Pt nanoparticles [7]. Recent application of Pt nanoparticles includes the detection of low concentrations of DNA by employing a platinum nanoparticle–gold ultra microelectrode in a hydrazine oxidation reaction [8].

Masson et al developed a surface plasmon resonance (SPR) based sensor for Myoglobin [9]. This type of detection using SPR phenomenon is relatively easy and cheap to perform that also allows quantitative/kinetic measurement of molecular interactions but the main problem associated with SPR sensor is fouling ability, low affinity and specificity that affect sensitivity of biosensing transducers. Other type of optical biosensors used for Mb detection includes, such as developed by Darain et al [10] and Matveeva et al [11] that can perform enhanced Mb immunoassays but these are expensive and require dedicated personnel to perform the tests. Also, they require difficult labeling procedures that depend on indirect indicator based signal schemes. Matveeva et al have utilized silver island films (SIF) for developing a fluorescence based



immunoassay for the cardiac Mb. However, the main disadvantageous of this method is the non-homogeneous nature of SIFs, which results in significant deviations in assay readings and is therefore not suitable for the precise Mb detection [11].

In this chapter, considering the advantages of EIS method and the properties of metal Pt nanoparticles, we report a platform for the construction of a bioelectrode for the detection of cardiac biomarker, cMb, using functionalized Pt nanoparticles. The functionalized Pt nanoparticles are covalently anchored on the self assembled monolayer (SAM) of 3-aminopropyltriethoxy silane (APTES) over an indium-tin-oxide (ITO)-glass plate. Subsequently, the cardiac protein antibody, Ab-cMb, is covalently attached to the carboxyl functionalized Pt nanoparticle-modified APTES/ITO-glass plates using carbodiimide coupling reaction. This bioelectrode is systematically characterized by various microscopic techniques and its immunosensing characteristic towards the quantitative estimation of the cardiac biomarker antigen, Ag-cMb, in phosphate buffer saline (PBS; pH 7.4) is investigated by EIS technique using  $[\text{Fe}(\text{CN})_6]^{3-/4-}$  as a redox probe.

## **5.2 Experimental**

### *5.2.1 Reagents*

Monoclonal mouse anti-human cardiac myoglobin (Ab-cMb; Cat 4M23) and Myoglobin derived from human heart tissue (Ag-cMb; Cat 8M50) were procured from Hytest (Turku, Finland). Mouse immunoglobulin-G (Ag-IgG) (Cat IGP3) is obtained from GENEI, Bangalore, India. 3-Aminopropyl triethoxysilane (APTES) was purchased from

Merck chemicals (Germany). N-(3-dimethyl aminopropyl)-N'-ethyl carbodiimide hydrochloride (EDC) and N-hydroxy succinimide 98% (NHS), Hydrogen hexachloroplatinate hexahydrate ( $\text{H}_2\text{PtCl}_6 \cdot 6\text{H}_2\text{O}$ ), sodium borohydride ( $\text{NaBH}_4$ ) and 3-mercaptopropionic acid (MPA) were obtained from Sigma-Aldrich Corp. All other chemicals were of analytical grade and used without further purification.

### 5.2.2 Equipments

Contact angles were recorded on Drop Shape Analysis System; model DSA10MK2 from Krüss GmbH, Germany. XRD pattern were recorded using Bruker AXS Advance D8 powder X-ray diffractometer. High resolution transmission electron microscopy was performed on HRTEM model: Tecnai G2 F30 STWIN with field emission gun, operated at 300 kV. SEM images were obtained with a LEO 440 PC; UK based digital scanning electron micrograph with a mounted energy dispersive X-ray spectrometer (EDX). FTIR spectrum was taken on Perkin- Elmer, Spectrum BX II. AFM images were obtained on a Nanoscope 5, VEECO Instrument Ltd., USA. Cyclic voltammetry and EIS measurements have been done on a PGSTAT302N, AUTOLAB instrument from Eco Chemie, The Netherlands. The EIS experimental data were circuit fitted by GPES (General purpose electrochemical system version 4.9, Eco Chemie) software and values of EIS parameters were obtained.

### 5.2.3 Synthesis of functionalized Pt nanoparticles

3-mercaptopropionic acid capped Pt (MPA) nanoparticles were chemically synthesized using conventional sodium borohydride reduction method in aqueous solution as reported

earlier, with slight modification [12]. Briefly, a 100 mM stock solution of Pt salt was prepared by dissolving 1 g of  $\text{H}_2\text{PtCl}_6 \cdot 6\text{H}_2\text{O}$  in 19 mL deionized water. 1 mL of this stock solution was then subsequently reduced by adding drop wise  $\text{NaBH}_4$  solution (48 mg in 2 mL  $\text{H}_2\text{O}$ ) under constant stirring. The change in color of the solution from yellow to dark brown indicated the formation of the Pt nanoparticles. A solution of 46  $\mu\text{L}$  MPA in 10 mL  $\text{H}_2\text{O}$  was then immediately added to stabilize the above Pt colloidal solution and the final volume of the reaction mixture was kept at 50 mL. The reaction mixture was left for stirring for 2 h at room temperature. Thereafter, the colloidal solution was washed 2 to 3 times with ethanol and centrifuged at 20000 rpm, and vacuum dried for 12 h.

#### *5.2.4 Preparation of bioelectrode*

The ITO coated glass plates ( $10\Omega / \square$ ) were cleaned by sequential ultrasonic cleaning in extran, acetone, ethanol, isopropyl alcohol and DI for 10 min each and dried in vacuum. The cleaned ITO glass plates were then exposed to oxygen plasma for 5 min in a plasma chamber to increase the amount of hydroxyl groups present on the ITO-glass surface. After this, these ITO glass plates were immersed in 2% APTES solution prepared in ethanol for 1.5 h, under the ambient conditions, to form a SAM of APTES and then subsequently rinsed with ethanol in order to remove non-bonded APTES from the surface of the substrate and dried under  $\text{N}_2$  gas flow. The carboxyl groups present on the Pt(MPA) nanoparticles were first activated to prepare amine-reactive esters of carboxylate groups by adding 30 mM NHS and 150 mM EDC in 5 mL aqueous solution of  $0.1 \text{ mg mL}^{-1}$  Pt(MPA) nanoparticles. The APTES modified ITO glass plates were then immersed in the above solution mixture of activated functionalized Pt(MPA)

---

nanoparticles for 3 h, followed by washing with double distilled water and dried under  $N_2$  gas flow to obtain Pt (MPA-NHS)/APTES/ITO-glass. The cardiac myoglobin protein antibody (Ab-cMb) was immobilized onto the above said modified electrode by treating it with a phosphate buffer solution (PBS, pH 7.4) containing  $100 \mu\text{g mL}^{-1}$  Ab-cMb, for overnight period at  $4^\circ\text{C}$ , followed by washing with PBS and drying under  $N_2$  flow. The Ab-cMb immobilized electrode was then incubated in 1% BSA solution, for 30 min to block the nonspecific binding sites on the electrode surface, followed by washing with PBS to remove any physically adsorbed antibodies and dried under  $N_2$  flow. The schematic representation of the stepwise fabrication of the prototype assembly of Ab-cMb/Pt(MPA)/APTES/ITO-glass electrode is shown in Fig. 5.1.

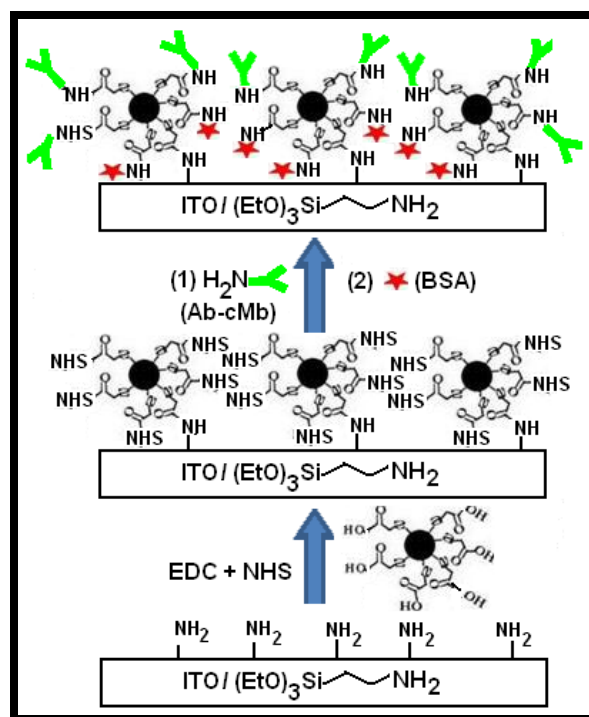


**Fig. 5.1:** Schematic representation of stepwise fabrication of the bioelectrode

## 5.3 Results and discussion

### 5.3.1 Contact angle measurement

In contact angle measurement water droplets were manually introduced onto the electrode surface with a micro syringe and the digital snapshots were taken of the droplets on the surface and analyzed with software provided by Kruss. Four replicates for each measurement at different steps of modifications was taken to establish statistical significance. The bare ITO-glass electrode with its surface hydroxyl groups shows hydrophilic behavior with a  $\theta$  value of  $40 \pm 1^\circ$  (Fig. 5.2a). The surface polarity alters after the modification of the ITO-glass electrode by hydrophobic alkyl chains of APTES molecules that decrease the surface energy by drastically reducing the hydroxyl groups of the bare ITO-glass on silanization and increases the value of  $\theta$  to  $78 \pm 1^\circ$  (Fig. 5.2b). The covalent attachment of Pt(MPA) nanoparticles on APTES/ITO-glass leads to the formation of a hydrophilic surface comprising of carboxyl groups which decreases the value of  $\theta$  to  $59 \pm 2^\circ$  (Fig. 5.2c). Further, after immobilization of the protein antibody the value of  $\theta$  increases significantly to  $91 \pm 1^\circ$  (Fig. 5.2d) due to the substitution of hydrophilic carboxyl groups by hydrophobic amino acid chains of protein antibody molecules, thereby indicating the attachment of Ab-cMb molecules over the Pt(MPA) modified electrode surface assembly.

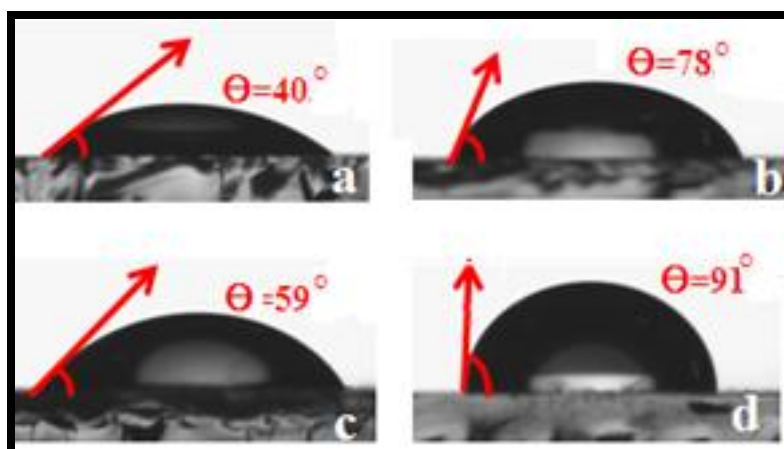


**Fig. 5.2:** Contact angle measurement images of (a) ITO coated glass plate; (b) APTES / ITO-glass; (c) Pt(MPA)/APTES/ITO-glass; and (d) Ab-cMb/Pt(MPA)/APTES /ITO-glass

### 5.3.2 Microstructural characterization

XRD has been used to examine the possible crystallinity of the Pt nanoparticles formed after sodium borohydride reduction. Fig. 5.3 shows the X-ray diffraction pattern of the functionalized Pt nanoparticles. The sample exhibits broad characteristic diffraction peaks of Pt with face center-cubic (f.c.c.) structure (JCPDS, card No. 4-802). The strongest diffraction peak were located at  $2\theta$  of  $39.46^\circ$  (111) with other two strong peaks at  $45.88^\circ$  (200) and  $67.32^\circ$  (220) respectively. The existence of broad intense peaks in the X-ray spectra indicates the presence of Pt nanoparticles with the nanocrystal dimensions. Since the breadth remains almost consistent for each peak, then certainly, the broadening is due to crystallite size. By using XRD peaks, the average size of Pt nanoparticles can be estimated by the width of the reflection according to the Debye–Scherrer equation (Eqn. 5.1):

$$D = 0.9\lambda/\beta \cos \theta \quad (5.1)$$

The average particle size of the Pt nanoparticles was calculated to be about 5.14 nm.

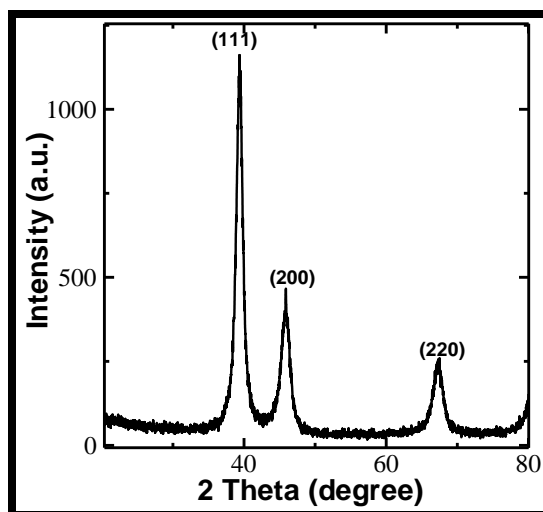


*Fig. 5.3: XRD Pattern of Pt nanoparticles*

HRTEM shows that the microstructure was uniform with individual particles revealing faceted growth having sharp edges with a nature of intermingling to each other (Fig. 5.4a). Four numbers of such nanoparticles are clearly marked as A to D in Fig. 5.4b. Since most of the instances, these particles are overlapped and abutting to each other, a set of moiré fringes are also discerned (region marked as dotted circle in Fig. 5.4b). It is important to mention that at atomic scale the individual particles are interpreted as nanocrystallites with stacking of atomic planes in particular crystallographic orientations. The interplanar spacings of three such planes as 0.23, 0.20 and 0.14 nm corresponding to hkl: 111, 200 and 220, respectively, of Pt-face centered cubic structure (space group:  $Fm\bar{3}m$ , and lattice parameter:  $a = 0.39$  nm, ref. JCPDS card no. 040802) are marked on the micrograph (Fig. 5.4b). The measurements carried out on Fig. 5.4a and b, further delineated that the size of these nanoparticles is on average between 4 nm to 5 nm (Fig.

5.4c), however in general these particles ranged between 1.5 nm to 8.5 nm on Gaussian graph.

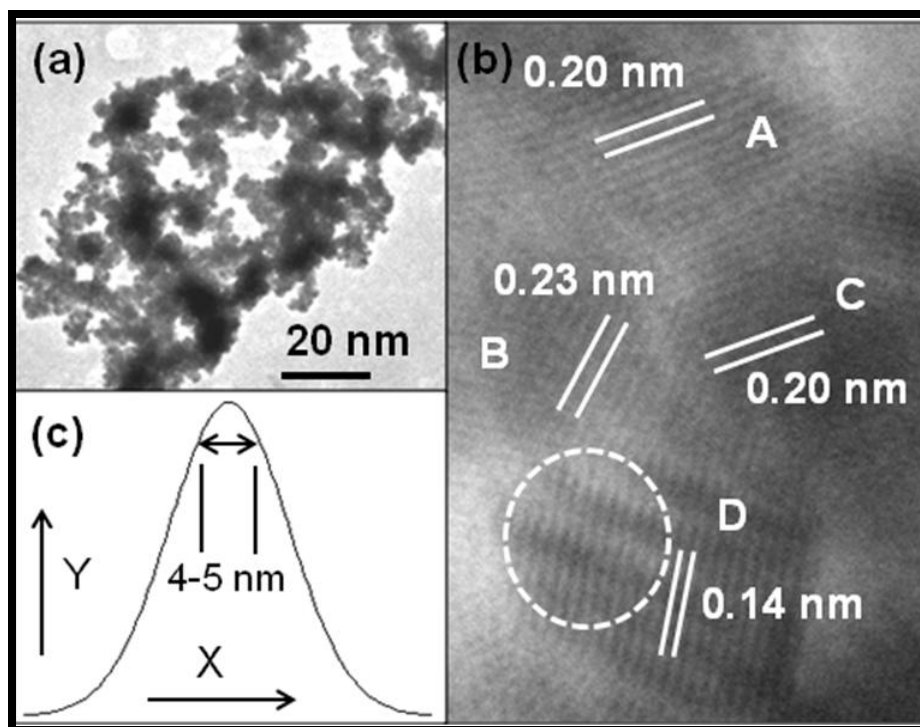


**Fig. 5.4:** HRTEM micrographs showing (a) distribution of nanoparticles (b) atomic scale images of different particles. (c) Gaussian size-distribution curve of the nanoparticles obtained from figs. (a) and (b). X-axis: 1.5 nm to 8.5 nm (size of particles) and Y-axis: 0 to 20 (no. of particles).

Fig. 5.5 shows the typical EDX pattern of Pt-NPs functionalized APTES modified ITO-glass with an inset showing the SEM image of the corresponding electrode area. The EDX spectra demonstrate the presence of Pt-NPs along with other elements of the corresponding silane and ITO-glass. SEM image shows metallic granular particles of Pt nanoparticles distributed over the modified electrode surface area.



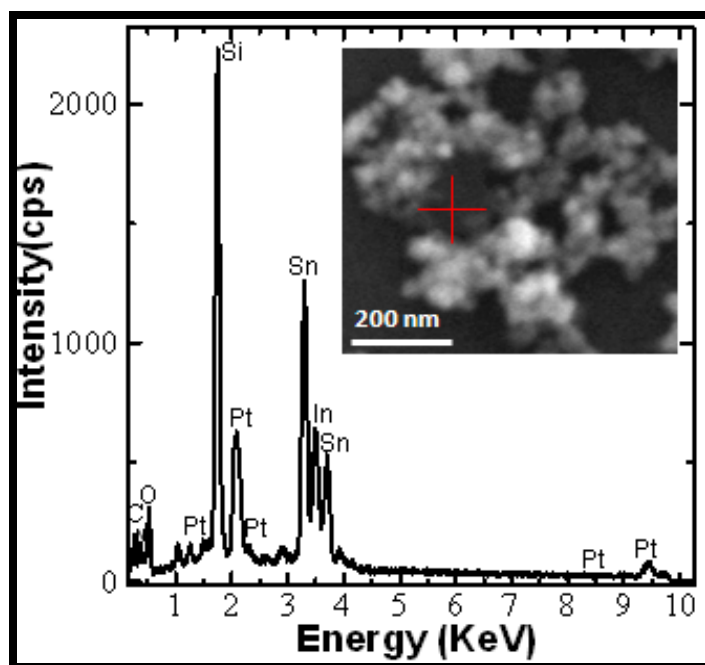


*Fig. 5.5: EDX spectra of Pt(MPA) nanoparticles on ITO-glass; Inset: corresponding SEM area at the magnification of 50 KX*

Figure 5.6 shows FTIR spectra of the (a) APTES/ITO (b) Pt (MPA)/APTES/ITO and (c) Ab-cMb/Pt(MPA)/APTES/ITO taken on attenuated total reflection mode. For APTES (Fig. 5.6a) the spectrum shows the Si-O-Si characteristic band at  $1055\text{ cm}^{-1}$  [13]. The characteristic peak observed at  $1750\text{ cm}^{-1}$  (Fig. 5.6b) is due to the C=O stretching vibrations and of the carboxylic groups of the MPA functionalized Pt nanoparticles. Further the peaks at  $2965\text{ cm}^{-1}$  and  $936\text{ cm}^{-1}$  refers to the -OH stretching and bending vibrations of the carboxylic acid group. After the immobilization of protein antibody Ab-cMb, additional peaks at  $3387\text{ cm}^{-1}$  and  $1612\text{ cm}^{-1}$  (Fig. 5.6c), representing the N-H stretching and bending vibrations [14] respectively was observed, which is indicative of the formation of amide bond by the Pt(MPA) nanoparticles with Ab-cMb molecules.

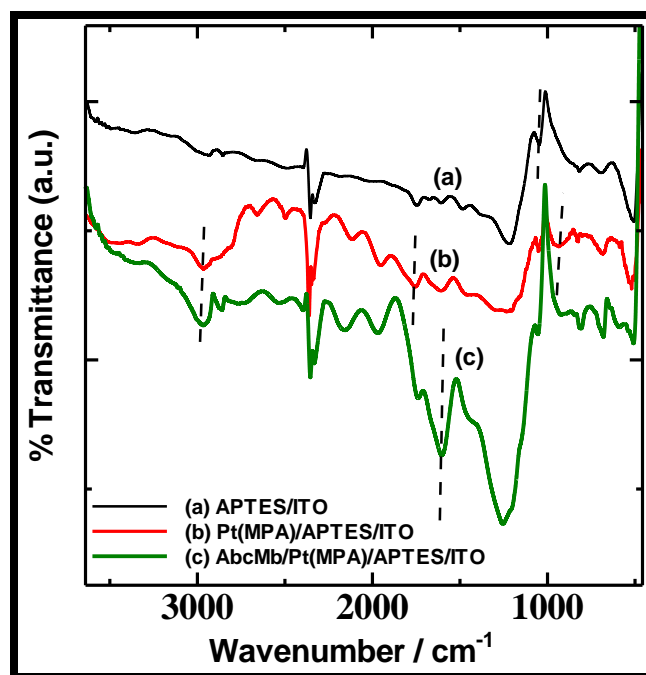


**Fig.5.6:** FTIR spectra of (a) APTES/ITO-glass (b) Pt(MPA)/APTES/ITO-glass and (c) AbcMb/Pt(MPA)/APTES/ITO-glass

The surface morphology of the each modified step involved in the fabrication of Pt(MPA) modified bioelectrode was characterized by using AFM images taken in a non contact mode. The surface roughness parameter ( $R_a$ ) and root mean square roughness ( $R_q$ ) are the two amplitude parameters that has been used to study the temporal changes occurred in the creation of a new surface, and spatial differences when studying the surface feature using different scales in terms of irregularity and height distribution. Fig. 5.7a shows the AFM image of the SAM of APTES on ITO-glass surface having a regular island-like structure with only a few surface aggregates. The corresponding  $R_a$  and  $R_q$  of APTES/ITO-glass surface are 0.886 nm and 1.08 nm respectively. The surface morphology changes to a dense and complete one with granular particles spreading all over it on modification with Pt(MPA) nanoparticles (Fig. 5.7b), showing an increased

values of both  $R_a$  and  $R_q$  to 1.56 nm and 1.95 nm, respectively. However, the AFM image (Fig. 5.7c) of the bioelectrode shows a completely changed morphology upon protein Ab-cMb immobilization with an appreciable increase in  $R_a$  value of 1.72 nm and  $R_q$  of 2.12 nm, exhibiting a comparatively much bigger and more globular feature characteristic to protein nature [15]. This significant increase in both the  $R_a$  and  $R_q$  values indicated the immobilization of the Ab-cMb molecules well over the surface of Pt-NPs modified electrode.

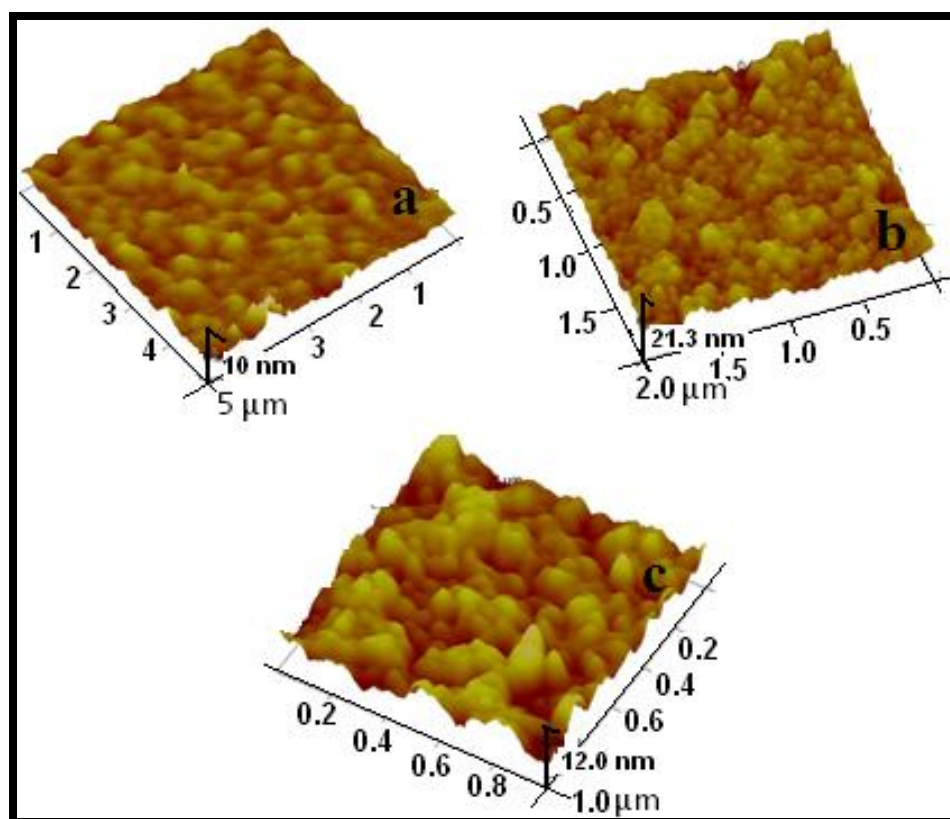


**Fig. 5.7:** AFM images of (a) APTES/ITO-glass (b) Pt(MPA)/ APTES/ITO-glass and (c) Ab-cMb/Pt(MPA)/APTES/ITO-glass

### 5.3.3 Electrochemical characterization of the bioelectrode

The impedance related to CPE is given by Eqn.5.2:

$$Z_{\text{CPE}}(\omega) = 1/Y_0(j\omega)^n \quad (5.2)$$

where  $Y_0$  is a constant,  $j$  is the imaginary number,  $\omega$  the angular frequency ( $\omega = 2\pi f$ , the frequency in Hz), and  $n$  is the CPE exponent. Since the value of  $n$  obtained for different modified electrodes is close to 1, CPE, in our case resembles a pseudo capacitor. Small value of  $\chi^2$  (Chi-square) of the order of  $10^{-4}$  so obtained suggest that the selected fitting circuit model could give appropriate results (table 5.1).

Fig. 5.8a shows the Nyquist plot of different modified electrodes with equivalent circuit shown in inset. The bare ITO-glass shows a  $R_{\text{et}}$  value of  $85.75 \Omega \text{ cm}^2$  (table 5.1) which sharply reduces to  $25.22 \Omega \text{ cm}^2$  for the APTES/ITO-glass indicating an easy electronic transport at the electrode surface interface. This reduction in the  $R_{\text{et}}$  value with a comparatively high  $Y_0$  value of  $4.82 \mu\text{F cm}^{-2}$  is attributed to an increased concentration of the anionic probe  $[\text{Fe}(\text{CN})_6]^{3-/4-}$  at the electrode/solution interface due to its strong affinity towards the polycationic layer, as the amino groups of the APTES get protonated ( $\text{NH}_3^+$ ) in aqueous solution. After the covalent attachment of the Pt(MPA) NPs to silane layer the  $R_{\text{et}}$  value increases sharply to  $107.0 \Omega \text{ cm}^2$  and  $Y_0$  decreases to  $3.07 \mu\text{F cm}^{-2}$  due to the charge repulsive behavior of the negatively charged carboxyl groups of Pt(MPA) NPs at pH 7.4 towards the anionic probe at the electrode/solution interface. To further establish the presence of carboxyl groups at the modified electrode surface, EIS study was performed on non-carboxyl functionalized Pt NPs (without MPA capping) modified APTES/ITO-glass electrode. As can be seen from the corresponding Nyquist plot

obtained, the decreased diameter of the semicircle with a sharp decrease in the corresponding  $R_{et}$  value to  $9.0 \Omega \text{ cm}^2$  indicates the unconstrained transfer of electrons from the probe towards the electrode surface. This extremely high relative signal change  $\Delta R_{et}$  (~1088 %) that has been observed at Pt(MPA)-NPs modified electrode with respect to Pt-NPs modified electrode constitutes great evidence for the high population of free carboxyl groups on the surface of Pt(MPA)/APTES/ITO-glass electrode. Further, covalent immobilization of cardiac myoglobin protein antibody on Pt(MPA)-NPs over the electrode surface and subsequent blocking of the non-specific binding sites by BSA significantly increases the  $R_{et}$  value to  $183.5 \Omega \text{ cm}^2$  and reduces the  $Y_0$  to  $2.44 \mu\text{F cm}^{-2}$  reflecting the insulating behavior of the protein molecule which inhibits both charge and mass transfer of the probe towards the electrode surface. A more clear description of the frequency-dependent behavior of different circuit elements of the fitted Randles' circuit is provided by the Bode plots as shown in Fig. 5.8b. Valuable information regarding certain kinetic phenomena occurring at the electrode/solution interface at different ranges of frequencies applied can be obtained from these plots. It is noticeable from the plot that at very low frequency region of  $<10 \text{ Hz}$ , a diffusive nature is obtained for APTES/ITO-glass electrode which on modification by Pt(MPA) nanoparticles is somewhat reduced and which finally disappears on immobilization of protein Ab-cMb on the modified electrode.

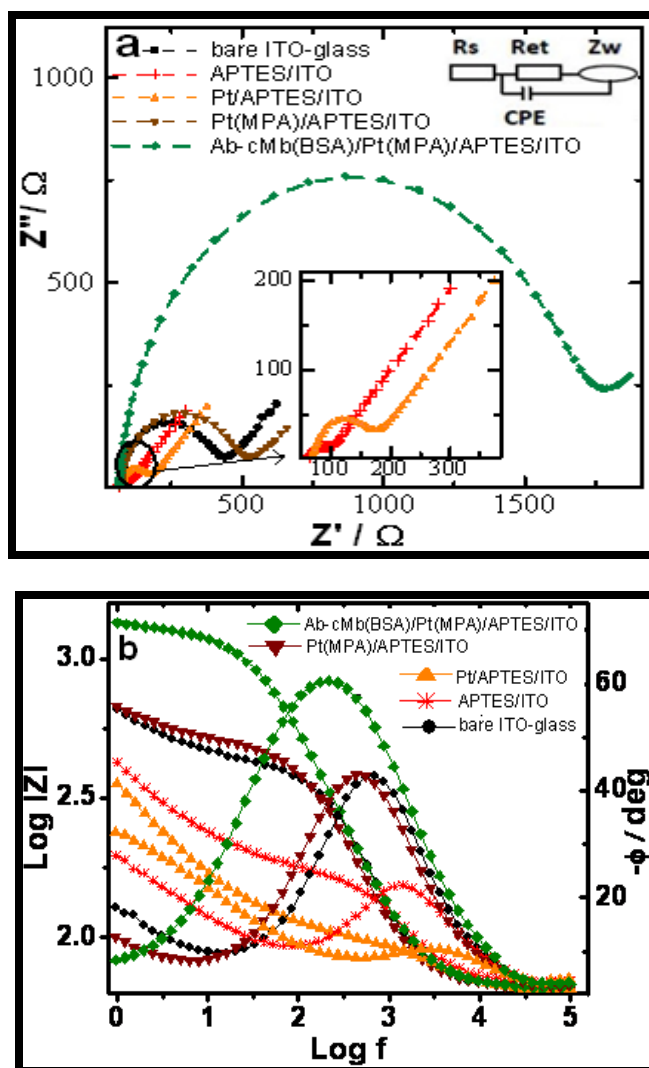


**Fig. 5.8:**(a) Nyquist plots obtained for bare ITO glass plate; APTES/ITO-glass; Pt(MPA)/APTES/ITO-glass; Pt/APTES/ITO-glass and Ab-cMb(BSA)/Pt(MPA)/APTES/ITO-glass in PBS containing 2mM  $[\text{Fe}(\text{CN})_6]^{3-/4-}$ ; (b) Corresponding bode plots

Davies and Compton proposed a term known as the diffusion layer thickness  $\delta$ , which helps in categorizing the type of diffusion occurring at the modified electrodes. The value of  $\delta$  can be obtained from the modified Einstein equation for the root mean square displacement of diffusing particles [16] as shown in Eqn. 5.3:

$$\delta = (2D\Delta E/\nu)^{1/2} \quad (5.3)$$

where D is diffusion coefficient of aqueous ferrocyanide ( $6.3 \times 10^{-6} \text{ cm}^2\text{s}^{-1}$ ),  $\Delta E$  is the potential width of the votammogram and  $\nu$  is the scan rate ( $0.05 \text{ Vs}^{-1}$ ). The  $\delta$  value obtained (table 5.1) for the bioelectrode shows a case 3 type behavior of the voltammetric response that corresponds to a spatially heterogeneous electrode. This phenomenon is associated with an overlap of adjacent diffusion layers resulting from the small size of the inert part of the electrode [16].

**Table 5.1:** EIS parameters at various stages of surface modification of the electrodes

Type of electrodes	$R_{et}$ ( $\Omega\text{cm}^2$ )	CPE $Y_0$ ( $\mu\text{Fcm}^{-2}$ )	n	$Z_w$ ( $\Omega\text{cm}^2$ ) ( $\times 10^{-4}$ )	$\chi^2$ ( $\times 10^{-4}$ )	$\delta$ ( $\mu\text{m}$ )
Bare ITO	85.7	2.76	0.93	3.45	1.88	55.44
APTES/ITO	25.2	4.82	0.87	3.42	1.13	49.69
Pt(MPA)/APTES/ ITO	107.0	3.07	0.88	3.67	1.99	61.68
Pt/ APTES/ ITO	9.0	13.19	0.77	3.22	1.38	47.09
Ab-cMb/Pt(MPA)/APTES/ ITO	183.5	2.44	0.96	3.90	2.30	72.74

### 5.3.4 Surface coverage and the nature of the bioelectrode

The value of the fractional coverage area ( $\theta$ ) of the functionalized Pt-NPs over the SAM of silane can be calculated from the impedance diagram using the Eqn. 5.4 [17]:

$$\theta = 1 - R_{et1} / R_{et2} \quad (5.4)$$

where  $R_{et1}$  and  $R_{et2}$  represents the surface specific charge transfer resistances of SAM modified APTES/ITO-glass and Pt(MPA)-NPS modified APTES/ITO-glass, respectively. The value of  $\theta$  was found to be 0.76, indicating a more than 76% surface coverage of the SAM modified electrode by Pt(MPA)-NPs.

The type of electrochemical mechanism occurring at the electrode/electrolyte interface of the Ab-cMb/Pt (MPA)/APTES/ITO-glass bioelectrode can be obtained from the relationship between the peak current and the scan rate. Fig. 5.9 shows the Cyclic Voltammogram (CV) of the resulting bioelectrode in 2mM  $[\text{Fe}(\text{CN})_6]^{3-/4-}$  at different scan rate from 25-125  $\text{mV s}^{-1}$  and a plot of the anodic ( $I_{pa}$ ) and cathodic peak currents ( $I_{pc}$ ) versus square root of the scan rates ( $v^{1/2}$ ) (inset of Fig. 5.9).

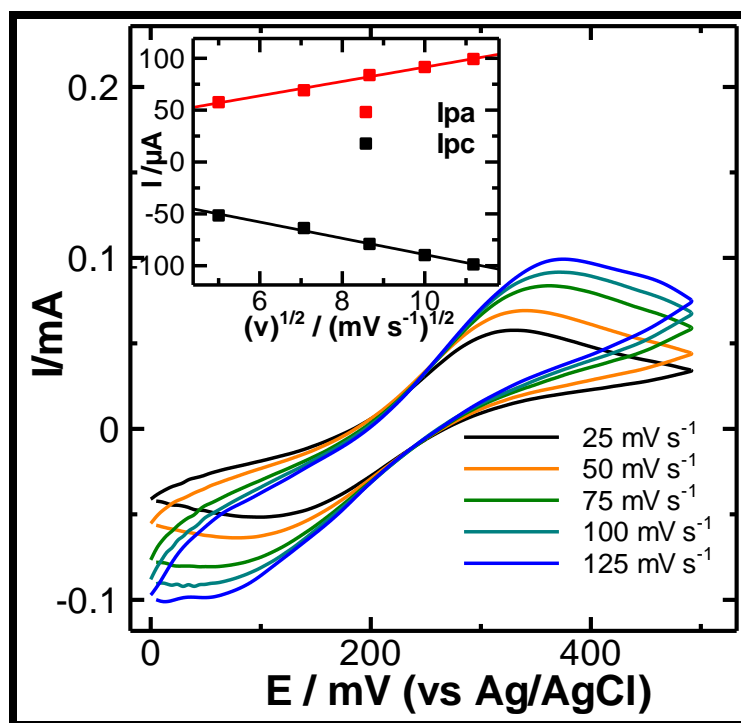


**Fig. 5.9:** CV of bioelectrode as a function of scan rate in PBS containing 2mM  $[\text{Fe}(\text{CN})_6]^{3-/4-}$ ; Inset: plot of redox peak current vs  $v^{1/2}$ .



A linear relationship with good correlation coefficients between the peak currents and the square root of scan rate was obtained suggesting a diffusion controlled process occurring at the bioelectrode/solution interface. The linear regression line so obtained between the anodic peak current  $I_{pa}$  and  $v^{1/2}$  can be expressed by the eqn. (5.5):

$$I_{pa} (v^{1/2}) = b v^{1/2} + 22.4 \quad (5.5)$$

where slope  $b = 6.90 \pm 0.01$ , having a correlation coefficient of 0.996.

### 5.3.5 Electrochemical impedance response to protein antigen

The specific immunoreaction of Ab-cMb to its complimentary target Ag-cMb at the electrode surface results in the formation of an antibody-antigen complex. This leads to an increase in  $R_{et}$  value due to the formation of kinetic barrier, which perturbs the interfacial electron transport, at the electrode surface. The sample solution without a target protein, Ag-cMb, has been taken as the control sample and the corresponding  $R_{et}$  value as the control sample response. Fig. 5.10a shows the Nyquist plots obtained after the subsequent addition of successive aliquots of different concentration of target protein antigen and the corresponding fitting values of  $R_{et}$  are given in table 5.2. The plot shows noticeable increment in the diameter of the Nyquist circles with increasing concentration of the added protein antigen Ag-cMb based on antigen-antibody interaction. A small but noticeable decrease in  $Y_0$  values was also observed with subsequent immunoreaction indicating a decrease in capacitive behavior of the bioelectrode with immunoreaction. The corresponding Bode frequency spectrum upon the above immunoreactions occurring at the electrode surface is shown in Fig 5.10b. In the high frequency region of  $>4$  kHz the total impedance  $\log |Z|$  remains unchanged with a phase angle ( $\phi$ ) of  $\sim 0^\circ$  indicative of

unchanged electrolyte solution resistance,  $R_s$ . In the intermediate frequency range i.e. from 4 kHz to 40 Hz almost a straight line curve was obtained with  $\phi$  value of  $> 55^\circ$  but  $< 90^\circ$  which is indicative of pseudo capacitance behavior of the bioelectrode in this frequency range. Negligible changes with the addition of target Ag-cMb in the sample solution were observed in this region which indicated that the proposed bioelectrode cannot function as a capacitive immunosensor. At low frequency region ( $< 40$  Hz), visible changes were observed in the impedance modulus lines upon immunoreactions with the increasing concentration of added target Ag-cMb. As this region is dominated by  $R_{et}$ , this has consolidated our choice of using changes in  $R_{et}$  as the main sensing element.

**Table 5.2:** EIS characteristic parameters upon immunoreactions with different concentrations of protein, Ag-cMb

Concentration of Ag-cMb	$R_{et}$ ( $\Omega\text{cm}^2$ )	CPE ( $Y_0$ ) ( $\mu\text{F cm}^{-2}$ )	n	$Z_w$ ( $\Omega\text{cm}^2$ ) ( $\times 10^{-4}$ )	$\chi^2$ ( $\times 10^{-4}$ )
Control	183.5	2.44	0.960	3.90	2.30
0.01 $\mu\text{g mL}^{-1}$	288.3	2.26	0.970	2.20	2.10
0.05 $\mu\text{g mL}^{-1}$	406.5	2.18	0.974	1.37	2.01
0.10 $\mu\text{g mL}^{-1}$	494.3	2.15	0.976	1.02	2.74
0.50 $\mu\text{g mL}^{-1}$	601.5	2.13	0.974	0.92	2.67
1.00 $\mu\text{g mL}^{-1}$	647.8	2.08	0.979	0.82	3.12

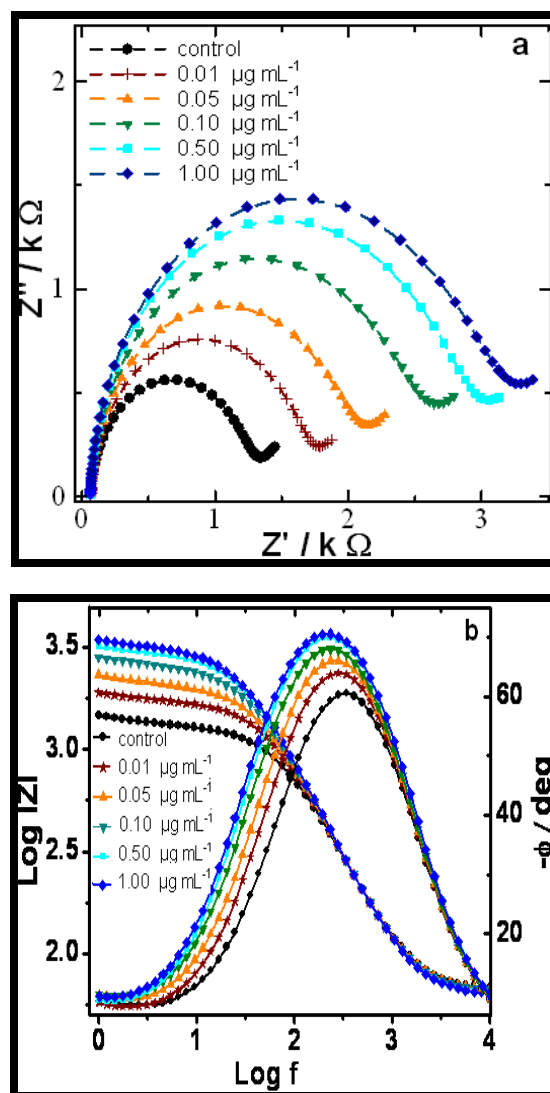


**Fig. 5.10:** (a) Faradaic impedance spectra of the Ab-cMb(BSA)/ Pt(MPA)/APTES/ITO-glass electrode before and after incubating with different concentration of Ag-cMb in PBS containing 2 mM  $[\text{Fe}(\text{CN})_6]^{3-/4-}$ , (b) Corresponding bode plots.

The sensitivity of the as prepared bioelectrode was obtained by plotting a graph (fig. 5.11) between the change in specific electron charge transfer resistance ( $\Delta R_{\text{et}} = (R_{\text{et}})_{\text{after immunoreaction}} - (R_{\text{et}})_{\text{control}}$ ) and logarithmic value of target Ag-cMb concentration in the range of 10  $\text{ng mL}^{-1}$  to 1  $\mu\text{g mL}^{-1}$ .

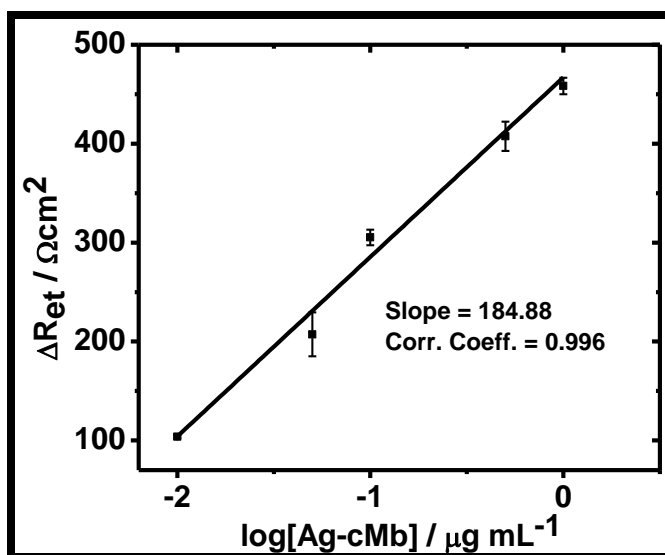


**Fig. 5.11:** Concentration dependent calibration curve of bioelectrode; the error bars represent the standard deviation from three separate experiments.

Eqn. 5.6 depicts the linear relationship so obtained with slope of the line as the sensitivity of the bioelectrode:

$$\Delta R_{et}(\log [\text{Ag-cMb}]) = b \log [\text{Ag-cMb}] + 473.74 \quad (5.6)$$

The  $R_{et}$  sensitivity (slope  $b$  of the calibration curve) of the bioelectrode was found to be  $184.8 \Omega \text{ cm}^2$  per decade of Ag-cMb with a correlation regression coefficient of 0.996 ( $n = 5$ ). The limit of detection was found out to be  $1.70 \text{ ng mL}^{-1}$  based on three times of signal-to noise ratio. This EIS experimental procedure requires about 12 minutes for complete assay including 3 minutes for the sample preparation without undergoing any pretreatment. These results show that this bioelectrode is better in terms of either physiological range of cMb detection with a minimum sample preparation time / experimental steps or sensitivity than the recently reported semiconductor/metal nanoparticle/carbon nanomaterials and polymer based bioelectrodes [11,18,24]. A

comparative analytical performance of some electrode system for Mb detection is given in Table 5.3.

**Table 5.3:** Analytical performance of some electrode systems for Mb detection

Electrochemical sensor type	Transduction platform	Linear range	Sensitivity/detection limit	References
Flow injection analysis with amperometry	MB-MWNTs/GCE	1.78 $\mu\text{g mL}^{-1}$ to 53.4 $\mu\text{g mL}^{-1}$	353.98 $\text{ngmL}^{-1}$	[24]
Impedimetric	SAM/Au electrode	$10^{-12}$ M– $10^{-6}$ M	15 $\text{ng mL}^{-1}$	[23]
Potentiometric	SAM of alkane thiol/ gold-coated silicon chip	-	1000 $\text{ng mL}^{-1}$	[22]
Square wave voltammetry	SPE/MeNP-DDAB/anti-cMb	10 $\text{ng mL}^{-1}$ to 400 $\text{ng mL}^{-1}$	5 $\text{ng mL}^{-1}$	[18]
Impedimetric	MUA-MPA/Au-wire	10 $\text{ng mL}^{-1}$ to 650 $\text{ng mL}^{-1}$	-	[20]
cyclic voltammetry	TiO <sub>2</sub> nanotubes/GCE	1 $\mu\text{g mL}^{-1}$ to 100 $\mu\text{g mL}^{-1}$	1000 $\text{ng mL}^{-1}$	[21]
Impedimetric	Pt(MPA)/APTES/ITO	10 $\text{ng mL}^{-1}$ to 1000 $\text{ng mL}^{-1}$	1.7 $\text{ng mL}^{-1}$	Present work

The high electroactive nature of the Pt nanoparticles makes this bioelectrode more sensitive to Mb detection than the recently reported ZnS nanoparticles based bioelectrode which exhibited a comparatively low sensitivity of 117.36  $\Omega \text{ cm}^2$  per decade [19]. The reproducibility of the bioelectrode was evaluated by measuring  $R_{\text{et}}$  response for each added concentration of the target Ag-cMb with three different bioelectrodes prepared

independently, under similar experimental conditions. The inter-assay variation coefficient was found to be within the range of 1.5 to 18 % at individual Ag-cMb concentration, indicating an acceptable precision and fabrication reproducibility. The stability of the bioelectrode was examined by repeatedly carrying out the impedance measurements on the bioelectrode for the same sample of target Ag-cMb under identical conditions. It has been observed that even after 5 repeated impedance measurements, no appreciable changes in the impedimetric response was observed revealing the bioelectrode retains its biocompatible property both in the solution and in open as well. A sustained  $R_{et}$  response was obtained with individual bioelectrode, stored at 4°C, towards a fixed Ag-cMb concentration for at least two month, indicating good shelf-life stability. The specificity of the bioelectrode towards the Ag-cMb was tested by carrying out the immunoreaction with non-specific mouse IgG, in the range of 10 ng mL<sup>-1</sup> to 10 µg mL<sup>-1</sup>, under identical conditions. No significant incremental changes were observed in the  $R_{et}$  values with the added aliquots of the non specific IgG with respect to the control sample. This may be attributed to either the non occurrence of antigen-antibody interaction or a weak non-specific interaction, if any, play insignificant role on evaluation of EIS spectra using this bioelectrode.

## 5.4 Conclusions

This work demonstrates a detail EIS characteristic of a bioelectrode based on functionalized Pt-NPs for the investigation of bioaffinity interaction towards the detection of prognostic cardiac marker, cMb. The functionalized Pt-NPs with large surface-to-volume ratio and free -COOH linkage groups remarkably improved the properties of the

---

bioelectrode in terms of stability and sensitivity. Both the microstructural and electrochemical characteristics of the bioelectrode have been extensively characterized by AFM, TEM, XRD, EDX, and EIS techniques. The dominance of  $R_{et}$  behavior in the low frequency region of the EIS spectra of the bioelectrode exhibited the biocompatible nature. The bioelectrode shows a small capacitance change with high resistive component of impedance exhibiting the most specific and sensitive relationship to the electron transfer rate and hence thereby provided a direct response to antibody-antigen interaction on immunoreaction. High protein loading with efficient covalent bonding to the Pt-NPs results in the construction of a bioelectrode showing a wider linear detection range with good sensitivity, biocompatibility and acceptable reproducibility. Also, the protocol devised here is simple, efficient and inexpensive that can be used as a model for establishing general methods for the detection and quantitative analysis of other protein marker assays, after optimization with blood serum, in the field of clinical diagnostics and molecular biology.

## 5.5 References

1. G. Hodes, *Adv. Mater.* 19 (2007) 639.
2. M. Adaris, L. Marzo, J. Pons, D. A. Blake and A. Merkoçi, *Biosens. Bioelectron.* 47 (2013) 190.
3. W. Wu, M. Wu, Z. Sun, G. Li, Y. Ma, X. Liu, X. Wang and X. Chen, *J. Alloys Compd.* 579 (2013)117.
4. Y. Chen, Y. Tang, S. Luo, C. Liu and Y. Li , *J. Alloys Compd.* 578 (2013) 242 .
5. X. Xu, X. Liu, Y. Li and Y. Ying, *Biosens. Bioelectron.* 47 (2013) 361.
6. Q. Kang, L. Yang and Q. Cai, *Bioelectrochemistry* 74 (2008) 62.
7. J. Wang, D. F. Thomas and A. Chen, *Anal. Chem.* 80 (2008) 997.
8. S. J. Kwon and A. J. Bard, *J. Am. Chem. Soc.* 134 (2012) 10777.
9. J.F. Masson, L. Obando, S. Beaudoin and K. Booksh, *Talanta* 62 (2004) 865.
10. F. Darain, P. Yager, K. L. Gan and S. C. Tjin, *Biosens. Bioelectron.* 24 (2009) 1744.
11. E. G. Matveeva, Z. Gryczynski and J. R. Lakowicz, *J Immunol Methods* 302 (2005) 26.
12. Y. Teow and S. Valiyaveetil, *Nanoscale* 2 (2010) 2607.
13. E. T. Vandenberg, L. Bertilsson, B. Liedberg, K. Uvdal, R. Erlandsson, H. Elwing and I. Lundstrom, *J. Colloid Interface Sci.*, 147 (1991)103.
14. A. Barth, *Biochim. Biophys. Acta*, 1767(2007) 1073.
15. L. Yang and Y. Li, *Biosens. Bioelectron.* 20 (2005)1407.
16. S.A. Mamuru and K.I. Ozoemena, *Electroanalysis* 22 (2010) 985.



17. V.Ganesh, S.K. Pal, S.Kumar and V. Lakshminarayanan, *J. Colloid Interface Sci.* 296 (2006) 195.
18. E.V. Suprun, A. L. Shilovskaya, A.V. Lisitsa, T.V. Bulko, V.V. Shumyantseva and A.I. Archakov, *Electroanalysis* 23 (2011)1051.
19. S. K. Mishra, D. Kumar, A. M. Biradar and Rajesh, *Bioelectrochemistry* 88 (2012) 118.
20. Rajesh, V. Sharma, V.K. Tanwar, S.K. Mishra and A.M. Biradar, *Thin Solid Films* 519 (2010) 1167.
21. S.S. Mandal, K. K. Narayan and A. J. Bhattacharyya, *J. Mater. Chem. B* 1(2013) 3051.
22. Y. Wang, Y. Zhou, J. Sokolov, B. Rigas, K. Levon and M. Rafailovich, *Biosens. Bioelectron.* 24 (2008)162.
23. M. Billah, H. C. W. Hays and P. A. Millner, *Microchim. Acta* 160 (2008) 447.
24. S. Pakapongpan, R. Palangsantikul and W.Surareungchai, *Electrochim. Acta*, 56 (2011) 683.

## CHAPTER 6

### **Protein Functionalized ZnS nanoparticles-Reduced graphene oxide composite based bioelectrode**

*In this chapter, a mercaptopropionic acid capped ZnS nanoparticles decorated reduced graphene oxide (RGO) hybrid based bioelectrode for the quantitative detection of human cardiac myoglobin (cMb) is reported. The ZnS nanoparticles were anchored over electrochemically reduced GO sheets through a cross linker, 1-pyrenemethylamine hydrochloride, by carbodiimide reaction and has been characterized by SEM, HRTEM and EDX spectroscopy. The HRTEM characterization of ZnS-RGO hybrid shows the uniform distribution of ultra-fine nano-particles of ZnS in nano-sheets of GO throughout the material. The protein antibody, Ab-cMb, was covalently linked to ZnS-RGO nanocomposite hybrid for the fabrication of the bioelectrode. A detail electrochemical immunosensing studies has been carried out on the bioelectrode towards the detection of target Ag-cMb. The optimal fitted equivalent circuit model that matches the impedance response has been studied to delineate the biocompatibility, sensitivity and selectivity of the bioelectrode. The bioelectrode exhibited a linear electrochemical impedance response to Ag-cMb in a range of  $10 \text{ ng mL}^{-1}$  to  $1 \text{ } \mu\text{g mL}^{-1}$  in PBS (pH 7.4) with a sensitivity of  $177.56 \text{ } \Omega \text{ cm}^2$  per decade. The combined synergistic effects of high surface to volume ratio of ZnS(MPA) nanoparticles and conducting RGO has provided a dominant charge transfer characteristic ( $R_{et}$ ) at lower frequency region of  $< 10 \text{ Hz}$  showing a good biocompatibility and enhanced impedance sensitivity towards target Ag-cMb.*

## 6.1 Introduction

Nanomaterials, including carbon-allotropes materials have received great attention due to their attractive properties and applications in many areas, including catalysis, sensing, electronics and photonics. Graphene, a one atom thick planar sheet of  $sp^2$  bonded carbon atoms with a dense honeycomb crystal structure [1] and unique physicochemical properties including high surface area, excellent electrical conductivity, strong mechanical strength, biocompatibility, ease of functionalization and mass production makes it a popular research subject for electro-chemical applications including sensors [2-4], electric devices [5] transistors [6], and fuel cells [7] to name only a few. Graphene is considered to be more advantageous when compared to other multidimensional carbon allotropes, such as carbon nanotubes, due to the fact that graphene does not contain metal impurities that dominate and foul the electrochemical behavior of the transducer [8]. Graphene oxide (GO), a highly oxidized form of graphene containing groups such as carboxylic groups at the edges and phenol, hydroxyl and epoxy groups on the basal planes has emerged as a well known precursor for graphene [9]. GO is electrically insulating material due to its randomly allocated nonconductive  $sp^3$  carbon sites and disrupted  $sp^2$  bonding networks. Recently, Hayami et al. [10] explained the mechanism of proton conduction in GO citing the proton propagation of the adsorbed water film via hydrogen-bonding networks of the hydrophilic sites present in GO as  $-O-$ ,  $-OH$ , and  $-COOH$  functional groups. They observed that the conductivity of GO is 2-3 orders of

magnitude greater than that of bulk graphite oxide. The findings specify the possible applications of GO-based perfect two-dimensional proton-conductive materials in fuel cells, sensors, and so on. Among the different methods reported for reduction of GO sheets, the electrochemical reduction method is found to be a promising route for preparing reduced graphene oxide (RGO) modified electrode surface because it is simple, fast, inexpensive and more efficient than other methods such as chemical and thermal reduction, with no additional element such as N incorporated into the obtained RGO film [11]. Recent applications of RGO includes its use as a kind of novel electrochemical sensing material in biological systems, such as detection of DNA [4], protein and pathogen [12], design of cell/bacterial nanodevice [13] and drug delivery carrier [14].

To obtain enhanced mechanical, thermal and electrochemical properties, RGO surface has been functionalized with different materials such as polymers, inorganic metal/semiconducting nano materials and biomaterials [15-17]. The ability to retain the native structure of RGO while enabling the bioactivity of the functionalizing moiety through a surface confined process, as well as effective direct electron transfer reaction properties, mean that RGO is a suitable material for construction of electrochemical substrates. Wang et al recently prepared a glucose oxidase biosensor based on graphene and CdS nanoparticles [18]. For “green chemistry”, ZnS is very suitable as a good substitute of CdS due to its nontoxicity to the human body and low cost. Jian Du et al have done a comparison study of the electrochemical and photo electrochemical behaviors of three biosensors, based on the use of Au, CdS, and ZnS nanoparticles–

glucose oxidase (GOD) system and they found that biosensors based on ZnS NPs are more sensitive and much less toxic to human and environment than that of CdS NPs [19]. Recent application of ZnS in the field of biosensor includes the formation of single-walled carbon nanotubes based chemiresistive label-free DNA sensor [20]. The purpose of using water-soluble ZnS nanoparticles coated with carboxyl capping agents is that it can permit greater affinity to bind or interact with bio-target molecules and the biocompatible nature of the ZnS-RGO nanocomposite film can provide a favorable microenvironment to retain the activities of the immobilized proteins.

This chapter demonstrates a facile strategy to synthesize ZnS-RGO nanocomposite consisting of 3-mercaptopropionic acid (MPA) capped ZnS nanoparticles, ZnS(MPA), anchored on RGO sheets through a linker and deposited on to the silane modified ITO glass plate for the fabrication of a bioelectrode. In this work, we have utilized the large surface ZnS (MPA) nanoparticles, where the surrounding carboxyl functional groups provided high loading of protein antibody, Ab-cMb, molecules through strong carbodiimide linkage. The composition, morphology and the microstructure of the as-obtained ZnS(MPA)-RGO nanocomposite were characterized using various instrumental techniques such as SEM, HRTEM,EDX and electrochemical techniques. The impedimetric sensing performance of the bioelectrode with ZnS-RGO nanocomposite towards the quantitative detection of target protein antigen, Ag-cMb, in phosphate buffer solution (PBS; pH 7.4) was studied and compared with that of native RGO sheets without ZnS nanoparticles, to highlight the contribution of the ZnS nanoparticles in the overall enhanced immunosensing performance.

## 6.2 Experimental

### 6.2.1 Reagents

Ab-cMb (Cat4M2 MAb 4E2) & Ag-cMb (Cat 8M50) were obtained from Hytest (Turku, Finland). Mouse immunoglobulin-G (Ag-IgG) (Cat IGP3) was obtained from GENEI, Bangalore, India. 3-Aminopropyltriethoxysilane (APTES) was purchased from Merck chemicals (Germany). N-(3-dimethylaminopropyl)-N'-ethyl carbodiimide hydrochloride (EDC) and N-hydroxy succinimide 98% (NHS), zinc nitrate hexahydrate ( $\text{Zn}(\text{NO}_3)_2 \cdot 6\text{H}_2\text{O}$ ), sodium sulfide nonahydrate ( $\text{Na}_2\text{S} \cdot 9\text{H}_2\text{O}$ ), 1-pyrenemethylamine hydrochloride (PyMe-NH<sub>2</sub>), 1-pyrene butanoic acid succinimidyl ester (PyBtNHS) and 3-mercapto propionic acid (MPA) were obtained from Sigma-Aldrich Corp. All other chemicals were of analytical grade and used without further purification.

### 6.2.2 Equipments

Contact angles were recorded on Drop Shape Analysis System; model DSA10MK2 from Krüss GmbH, Germany. HRTEM was done using FEI model: Tecnai G2 F30 and JEOL model: JEM 2100F. SEM images were obtained with a LEO 440 PC; UK based digital scanning electron micrograph. Cyclic voltammetry and EIS measurements were done on a PGSTAT302N, AUTOLAB instrument from Eco Chemie, The Netherlands.

### 6.2.3 Fabrication of the bioelectrode

The ITO coated glass plates ( $10\Omega / \square$ ) were cleaned by sequential ultrasonic cleaning in extran, acetone, ethanol, isopropyl alcohol and DI for 10 min each and dried in vacuum.

Then, the cleaned ITO glass plates were exposed to oxygen plasma for 5 minutes in a plasma chamber. The ITO glass plates were immersed in 2% APTES solution prepared in ethanol for 1.5 h, under the ambient conditions, to form a Self assembled monolayer (SAM) of APTES. These glass plates were then rinsed with ethanol in order to remove non-bonded APTES from the surface of the substrate and dried under N<sub>2</sub> gas flow. The APTES modified ITO glass plates were then immersed in the GO solution (0.3 mg mL<sup>-1</sup>) for a period of 1 h followed by washing with distilled water and dried under N<sub>2</sub> to form the GO/APTES/ITO-glass electrodes. Negatively charged GO flakes were deposited on the positively charged amino modified APTES/ITO-glass plates due to electrostatic interactions and were not removed even after repeated washing. The GO/APTES/ITO-glass electrodes were then electrochemically reduced by cyclic voltammetry (CV) in 0.5 M KCl solution saturated with N<sub>2</sub> gas from 0.7 to -1.1V for 3 CV cycles, at a scan rate of 50 mVs<sup>-1</sup> (Fig. 6.1) to reduced graphene oxide (RGO).

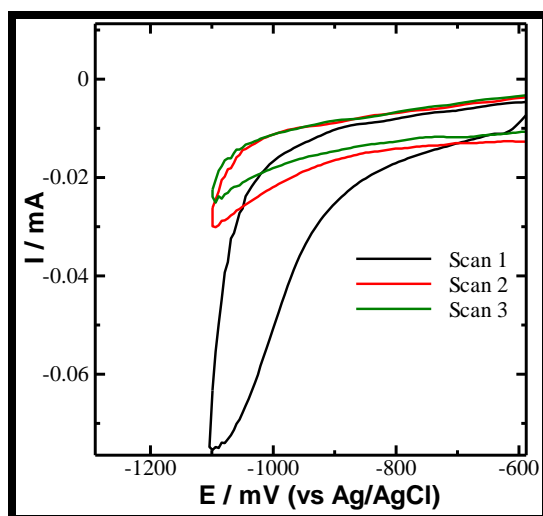
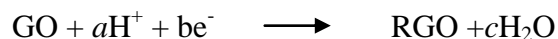


**Fig. 6.1:** Electrochemical reduction of GO/APTES/ITO-glass surface in a deaerated solution of 0.5 M KCl, at a scan rate of 50 mV s<sup>-1</sup>.

The large reduction current at  $-1.1\text{V}$  corresponds to the reduction of the surface oxygen groups only and not water since the reduction of water to hydrogen occurs at more negative potential (e.g.,  $-1.5\text{V}$ ) as shown in the scheme.



However, this reduction peak at  $-1.1\text{V}$  disappeared in the next two consequent scans and is therefore irreversible, indicating the reduction of surface oxygenated species in the first cycle only with the formation of RGO. The remaining two CV cycles correspond to the electrochemical behavior of the resulting RGO/APTES/ITO.

The RGO/APTES/ITO-glass electrodes were then immersed in  $6\text{mM}$  solution of PyMe-NH<sub>2</sub> in DMF, for 2 h, at room temperature, thereafter washed extensively with DMF and dried under N<sub>2</sub> gas flow. The ZnS(MPA) nanoparticles were synthesized in aqueous solution, at room temperature, by method as reported earlier [20]. PyMe-NH<sub>2</sub> functionalized RGO/APTES/ITO-glass electrodes were treated with  $1\text{ mg mL}^{-1}$  aqueous solution of ZnS(MPA) nanoparticles containing  $0.1\text{M}$  EDC and  $0.05\text{M}$  NHS for 2 h and was rinsed thoroughly with double distilled water to obtain the ZnS(MPA) functionalized RGO/APTES/ITO-glass electrodes. Ab-cMb was then covalently immobilized on ZnS(MPA)-RGO/APTES/ITO-glass electrodes by immersing them in PBS buffer (pH 7.4) containing  $100\text{ }\mu\text{g mL}^{-1}$  Ab-cMb, for an overnight period at  $4^\circ\text{C}$ , followed by washing with PBS and drying with N<sub>2</sub> flow. The protein antibody immobilized electrodes were further immersed in  $1\%$  BSA (W/V) solution to block the nonspecific binding sites and the remaining unbound free carboxyl groups as well, followed by washing with PBS to remove any physically adsorbed antibodies and finally



dried under  $N_2$  flow and stored at  $4^\circ C$ . Ab-cMb was covalently immobilized directly over the RGO sheets through PyBtNHS without undergoing any functionalization with ZnS nanoparticles to fabricate Ab-cMb/ RGO/APTES/ITO-glass for comparative study. The stepwise construction of the prototype assembly is represented in Fig. 6.2.

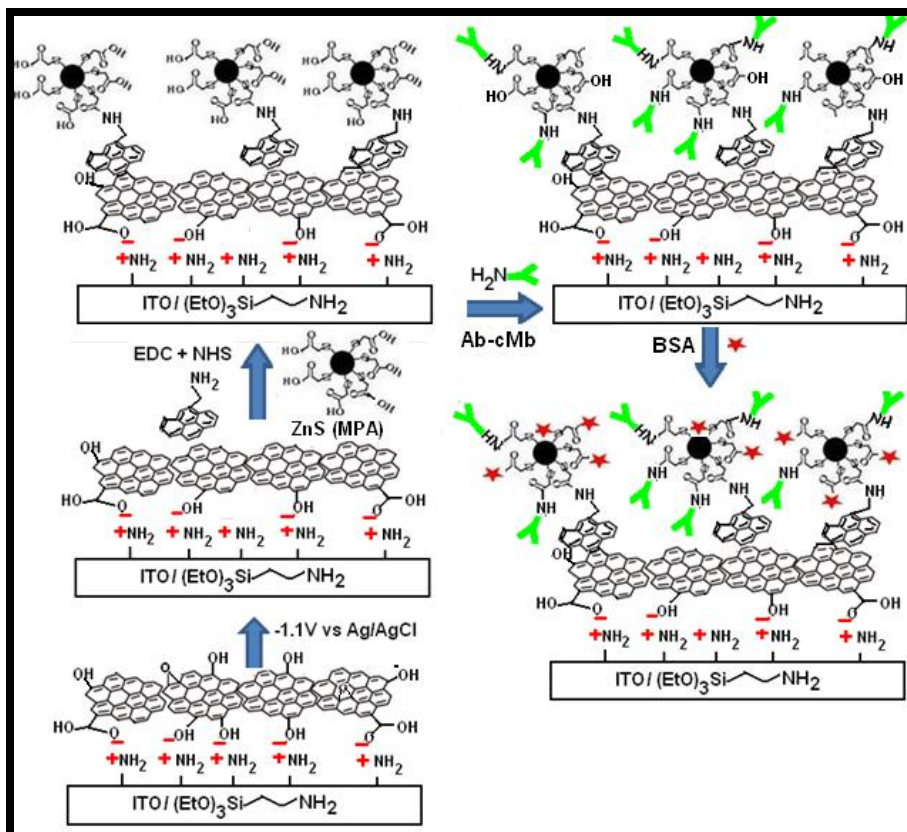


*Fig. 6.2: Schematic representation of the stepwise fabrication of the bioelectrode*

## 6.3 Results and Discussions

### 6.3.1 Contact angle measurement

Contact angle measurements were repeated with four drops of water as test liquid probe, at different regions of the modified surface and are shown in Fig. 6.3.



**Fig. 6.3:** Contact angle measurement images of (a) ITO coated glass plate; (b) APTES/ITO-glass; (c)GO/APTES/ITO-glass; (d) RGO/APTES/ITO-glass; (e) ZnS(MPA)-RGO/APTES/ITO-glass; (f) Ab-cMb/ZnS(MPA)-RGO/APTES /ITO-glass

The obtained contact angle value for bare ITO-glass was found to be  $40.15^{\circ} \pm 2^{\circ}$  (Fig. 6.3a) analogous to a hydrophilic surface with hydroxyl groups present on it. A significant increase in contact angle,  $73.42^{\circ} \pm 2^{\circ}$  (Fig. 6.3b) for the APTES modified ITO-glass was observed due to the presence of hydrophobic alkyl chains of APTES molecules. The drastic reduction of the hydroxyl groups on ITO-glass upon silanization by APTES molecules results in the decrease of the surface free energy of the APTES/ITO-glass plate with respect to bare ITO-glass (the polar component more than the dispersive component) leading to an increase in the contact angle. The hydrophobic behavior altered to hydrophilic one after the casing of the APTES/ITO-glass surface with GO containing hydrophilic groups like  $-\text{OH}$  and  $-\text{COOH}$ , reduces the contact angle to  $59.11^{\circ} \pm 1^{\circ}$  (Fig. 6.3c). After electrochemical reduction of the hydrophilic groups of GO/APTES/ITO-glass the contact angle again increased to  $78.70^{\circ} \pm 2^{\circ}$  (Fig. 6.3d). Further, after modification with ZnS(MPA), the contact angle of ZnS(MPA)-RGO/

APTES/ITO-glass slightly decreased to  $65.25^{\circ} \pm 1^{\circ}$  (Fig. 6.3e) due to the introduction of hydrophilic free carboxyl groups available on ZnS (MPA) nanoparticles. However, upon immobilization of hydrophobic protein antibody, Ab-cMb, molecules on ZnS(MPA)-RGO/APTES/ITO-glass the contact angle significantly increased to  $97.24^{\circ} \pm 1^{\circ}$  (Fig. 6.3f) indicating the formation of the bioelectrode.

### 6.3.2 Microstructural characterization

Figure 6.4 shows the SEM images RGO/APTES/ITO-glass and ZnS(MPA)-RGO/APTES/ITO-glass. The isolated flakes of GO as observed in Fig. 6.4a of SEM image demonstrates that many RGO sheets have been uniformly dispersed throughout the structure without aggregation. In contrast, the SEM of ZnS-RGO (Fig. 6.4b) shows a dense particulate feature covering the entire RGO sheets indicating a strong interaction between ZnS (MPA) nanoparticles and RGO flakes spreading well all over the electrode.

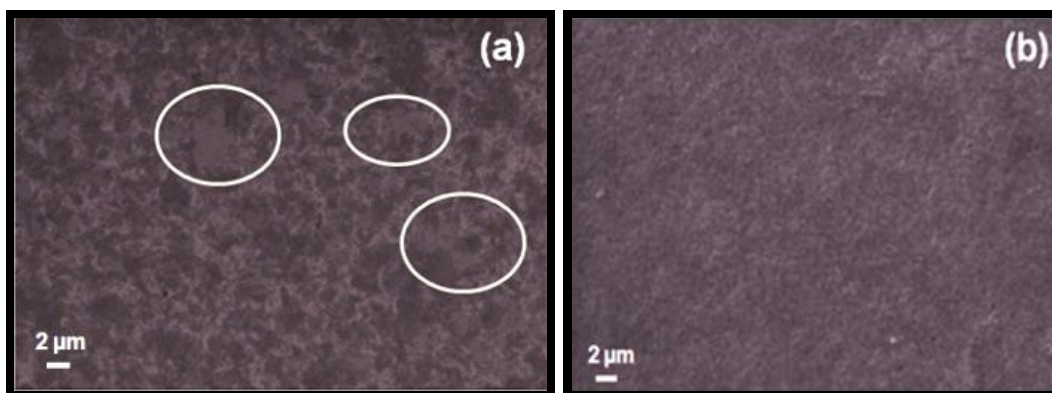


**Fig. 6.4:** SEM images of (a) RGO/APTES/ITO-glass at the magnification of 5 KX and (b) ZnS(MPA)-RGO/APTES/ITO-glass at the magnification of 20 KX.

High resolution transmission electron microscopy (HRTEM), using FEI model: Tecnai G2 F30 STWIN and JEOL model: JEM 2100F, was performed on two samples,

viz. GO and nano-particles of ZnS attached on GO. In general the microstructure of GO was noted as ultra-thin rolled layers of GO in an aggregate. The nano-sheets of GO are overlapping to each other with distinct boundaries. Two such distinct nano-sheets of GO are marked as I and II and their contours are separated with white dotted lines (Fig. 6.5a). An atomic scale image of such nano-sheets reveals a hexagonal honeycomb-like structure of a typical graphene with fringe spacing of about 0.34 nm (inset A in Fig. 6.5a). Another inset B in Fig. 6.5a shows a corresponding selected area electron diffraction pattern (SAEDP) elucidating the spots in hexagonal array with an obvious *c*-axis orientation of GO nano-sheet. A plane with 110 miller indices (*hkl*) of hexagonal crystal structure in reciprocal space is marked on SAEDP. In a composite microstructure of ZnS nano-particles with GO nano-sheets depicts that the ZnS nano-particles are distributed uniformly in the matrix of GO (Fig. 6.5b). Multiple sheets of GO co-existing with ZnS particles is clearly visible in the micrograph. A corresponding SAEDP of nano-composite of GO and ZnS exhibits the presence of prominent diffraction spots of GO (inset in Fig. 6.5b) as similar to that of Fig. 6.5a, along with faint spots (*hkl*:111 with inter-planar, *d*-spacing of 0.31 nm) of cubic zinc-blende type structure (reference: JCPDS card no. 80-0020, lattice constant:  $a = 0.5345$  nm) as marked in inset of Fig. 6.5b. Atomic scale high resolution image recorded from the coexisting GO and ZnS shows the presence of nano-particles of ZnS and fringes of GO. Fig 6.5c reveals such a nano-particle of ZnS of about 6 nm in size with well oriented atomic planes with inter-planar spacing of 0.31 nm with a partial overlap with GO with fringe spacing of 0.34 nm. In this micrograph, a nano-particle of ZnS with inter-planar spacing of 0.27 nm (*hkl*:

200), is also indicated. It is clear from the atomic scale images that the individual nanoparticles of ZnS are normally single crystals with stacking of well oriented atomic planes.

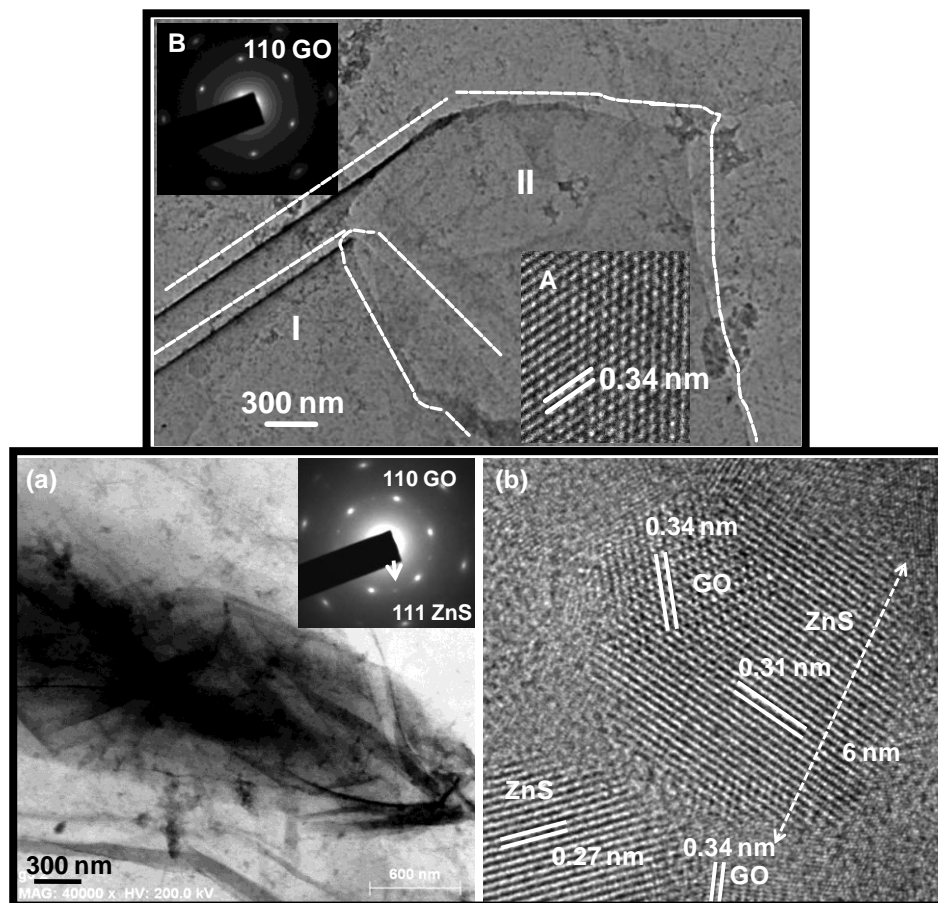


**Fig. 6.5:** (a) HRTEM image showing the nano-sheets of GO. Insets: (A) atomic scale image of GO and (B) corresponding selected area electron diffraction pattern; (b) Composite of nano-sheets of GO with nano-particles of ZnS. Inset: corresponding selected area electron diffraction pattern from GO and ZnS and (c) atomic scale image revealing inter-planar spacing of both GO and ZnS.

To study the chemical homogeneity ZnS in the matrix of GO nano-sheets, spectroscopy (EDX attached with TEM) was performed (Fig. 6.6).



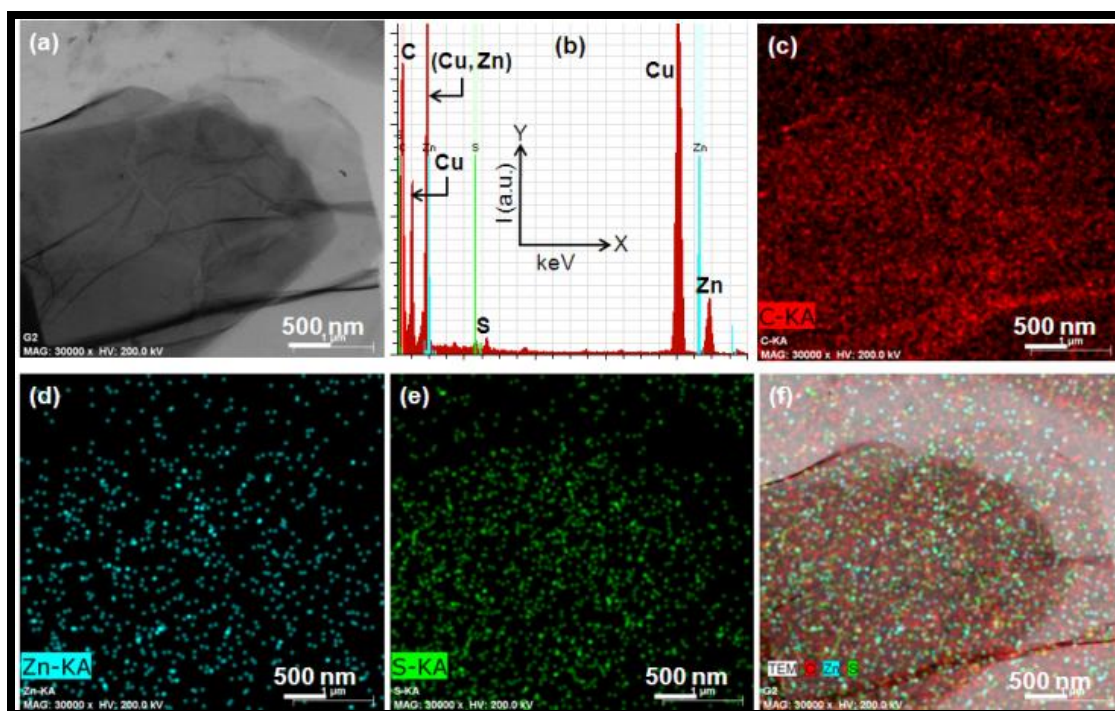


**Fig. 6.6:** HR-TEM image and corresponding EDX chemical measurements; showing (a) composite microstructure of nano-sheets of GO with nano-particles of ZnS, (b) corresponding EDX spectrum with X-axis: 0 to 10 keV and Y-axis: Intensity in arbitrary unit, (c) elemental map of C, (d) elemental map of Zn, (e) elemental map of S and (f) overlapped elemental maps of C, Zn and S.

Fig. 6.6a is a bright field micrograph of nano-composite of GO with ZnS. The EDX spectrum exhibits the presence of the peaks corresponding to energy levels of C (0.277 keV;  $K\alpha$ ), Zn (1.011 keV;  $L\alpha$  and 8.631 keV;  $K\alpha$ ), S (2.30 keV;  $K\alpha$ ) and Cu (0.929 keV;  $L\alpha$  and 8.0431 keV;  $K\alpha$ ), as displayed in Fig. 6.6b. The presence of Cu in the spectrum is due to the 200-mesh size Cu-TEM grids used in microscopy experiments. The EDX spectrum was further utilized to interpret the image–spectrum and therefore the different elemental maps (C, Zn, S) corresponding to the bright field micrograph has

been performed and displayed as in Fig. 6.6 c, d, e. Moreover an overlapped elemental map encompassing all three elements (C, Zn, S) have also been plotted (Fig. 6.6f). It is evident from these chemical maps of different elements that the distribution of ultra-fine nano-particles of ZnS in nano-sheets of GO is uniform throughout the material. In general the electron microscopy observations have delineated that the nano-sheets of GO and ultrafine nano-particles of ZnS is integrated uniformly throughout the microstructure of these nano-composite.

### 6.3.3 Electrochemical characterization of bioelectrode

EIS combines the analysis of both the resistive and capacitive properties of materials, based on the perturbation of a system at equilibrium by a small amplitude sinusoidal excitation signal. The impedance of CPE can be expressed by (Eqn. 6.1):

$$Z_{CPE}(\omega) = Y_0^{-1} (j\omega)^{-n} \quad (6.1)$$

where  $Y_0$  is a constant,  $j$  is the imaginary number,  $\omega$  the angular frequency ( $\omega = 2\pi f$ , in Hz) and  $n$  is the CPE exponent. As shown in Table 6.1, the value of 'n' for different modified electrodes is close to 1, indicated the presence of minimal defects in the modified layer on the electrode surface and that CPE in this case resembled closely to a capacitor. In the modified fitting equivalent circuit, the parallel elements (CPE and  $Z_w + R_{et}$ ) were introduced since the total current through the working interface was the sum of respective contributions from the Faradaic process and the double layer charging. The two components of the equivalent circuit,  $R_s$  and  $Z_w$  are not affected significantly by modifications on the electrode surface while the remaining two  $C_{dl}$  and  $R_{et}$  are controlled

by the surface modification of the electrode. In our case, a negligible change in  $R_s$  was observed during the modification process so it has been ignored. At the same time, as can also be seen in table 6.1, the changes in  $R_{et}$  values were much larger than those in other impedance components. Thus, changes in  $R_{et}$  value was taken as a suitable signal for sensing the interfacial properties of the prepared bioelectrode during all the surface modification steps and for immunoreaction as well. The total impedance ( $Z$ ), which is current-voltage ratio, can be represented by Eqn. 6.2 as a sum of in-phase ( $Z'$ ) and out-of-phase ( $Z''$ ) impedances:

$$Z(\omega) = Z'(\omega) + i Z''(\omega) \quad (6.2)$$

Figure 6.7a represents the Nyquist diagram of the electrodes prepared at various stages of surface modifications. The simulated values of the equivalent circuit elements are summarized in table 6.1. The Chi-squared function ( $\chi^2$ ) provides a good indication of the quality of the fit. Generally, the  $\chi^2$  statistic should be less than  $10^{-6}$  if the data are said to fit within the noise level of the measurement. Therefore, a value of  $10^{-5} \sim 10^{-4}$  indicates a reasonable good fit. Small values of  $\chi^2$  (Chi-square) of the order of  $10^{-4}$ , as obtained in our case (table 6.1) suggested that the chosen selected fitting circuit model is the most appropriate one. It is to be noted that the  $R_{et}$  value of  $99.8 \Omega \text{ cm}^2$  for APTES/ITO-glass electrode is much lower than that of a bare ITO-glass electrode ( $R_{et} = 184.8 \Omega \text{ cm}^2$ ) indicating an easy electronic transport at the electrode solution interface after the formation of SAM of APTES. After the modification of the APTES/ITO-glass electrode surface by GO the  $R_{et}$  value increased sharply to  $416.3 \Omega \text{ cm}^2$  and  $Y_0$  value decreases to  $3.75 \mu\text{F cm}^{-2}$ . This may be attributed to mainly two reasons first, GO is less electrically



conducting due to the oxidized surface and secondly, the negatively charged carboxyl ( $\text{COO}^-$ ) and hydroxyl ( $\text{OH}^-$ ) functional groups present on the surface generates the repulsive force to the negatively charged  $[\text{Fe}(\text{CN})_6]^{3-/4-}$  probe. The reduction of the most of these functional groups from the GO/APTES/ITO-glass electrode surface after electrochemical reduction provided a drop off in  $R_{\text{et}}$  value to  $139 \Omega \text{ cm}^2$  and increase in  $Y_0$  value to  $5.24 \mu\text{F cm}^{-2}$ . The incorporation of ZnS(MPA) nanoparticles on the RGO/APTES/ITO-glass electrode exhibited an increased  $R_{\text{et}}$  value of  $578.5 \Omega \text{ cm}^2$  and decrease in  $Y_0$  to  $4.48 \mu\text{Fcm}^{-2}$  due to the combined effect of semiconducting behavior of ZnS(MPA) as well as the repulsive interaction between the  $\text{COO}^-$  groups of ZnS (MPA) and the anionic probe  $[\text{Fe}(\text{CN})_6]^{3-/4-}$  at the electrode/solution interface. After the immobilization of protein antibody, Ab-cMb, on the surface of the ZnS(MPA)-RGO/APTES/ITO-glass electrode and on subsequent treatment with a blocking protein, bovine serum albumin (BSA), the  $R_{\text{et}}$  further increased to  $699 \Omega \text{ cm}^2$  and a slight decrease in  $Y_0$  value to  $4.20 \mu\text{Fcm}^{-2}$ . This may be attributed to the formation of a protein antibody layer on the electrode, which acts as the electron communication and mass-transfer blocking layer, thereby hindering the access of redox probe towards the electrode surface. The behavior of different circuit elements of the fitted Randles' circuit with the change in frequency is more pronounced with Bode plot (Fig. 6.7b). The Bode plot has some distinct advantages over the Nyquist plot. Since frequency appears as one of the axes, it's easy to understand from the plot how the impedance depends on the frequency and hence can provide information about certain kinetic phenomena occurring at the electrode/solution interface at different range of applied frequencies.

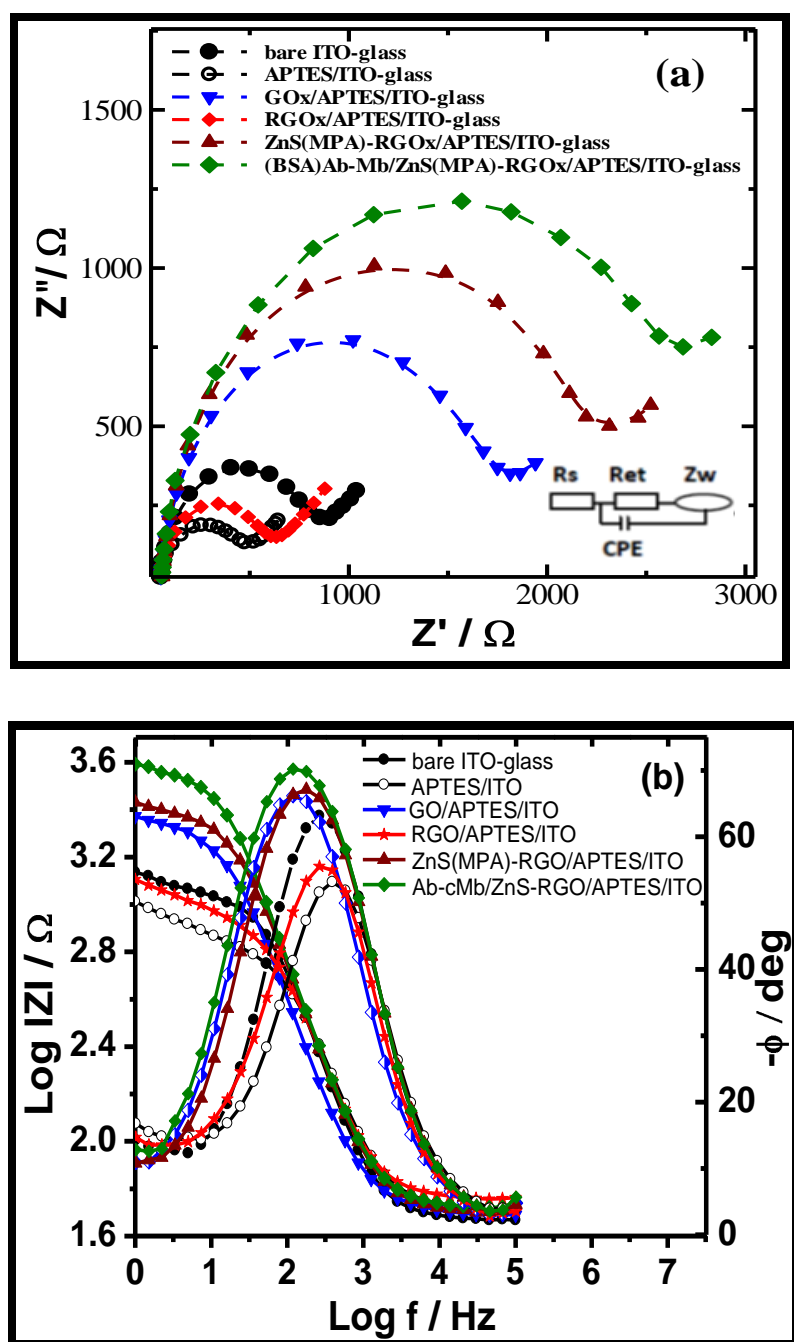


**Fig. 6.7:** (a) Nyquist plots obtained for bare ITO glass; APTES/ITO; GO/APTES/ITO; RGO/APTES/ITO; ZnS(MPA)-RGO/APTES/ITO; and Ab-cMb(BSA)/ZnS(MPA)-RGO/APTES/ITO in PBS containing 2 mM  $[\text{Fe}(\text{CN})_6]^{3-/4-}$ , (b) Corresponding bode plots

At very high frequency ranging from 10 kHz to 100 kHz, the only impedance is the ohmic resistance of the electrolyte solution ( $R_s$ ) for which negligible changes were observed at different stages of surface modification indicated that the  $R_s$  is independent of frequency. As the frequency drops, the contribution of capacitive element CPE becomes significant and so in the intermediate range of frequency i.e. from 50 Hz to 10 kHz almost a straight line curve is obtained which is indicative of capacitance behavior. Finally, in the low frequency region (<50 Hz) the impedance corresponding to CPE becomes very high so the only current that flows is through  $R_{et}$  and  $Z_w$ . It is in this low frequency region that we observed prominent changes in impedance with each steps of surface modification of the ITO-glass electrode leading to the formation of the bioelectrode. As can be seen from the Fig. 6.7b the  $R_{et}$  behavior of the bioelectrode has been shifted towards lower frequency region which is an indicative of good biocompatible nature of the bioelectrode.

The heterogeneous electron transfer rate constant ( $k^0$ ) values of  $[\text{Fe}(\text{CN})_6]^{3-/4-}$  redox couple for the unmodified bare ITO-glass electrode and after surface modifications were determined by using  $R_{et}$  values obtained from their corresponding impedance plots. The corresponding  $k^0$  values of the modified electrodes were calculated by using charge transfer kinetics (Eqn. 6.3):

$$k^0 = RT/n^2F^2A R_{et} C \quad (6.3)$$

where  $R$  is the gas constant,  $T$  is the temperature,  $n$  is the electron transferring constant of the redox couple,  $F$  is Faraday constant,  $A$  is the area of electrode ( $0.25 \text{ cm}^2$ ), and  $C$  is

the concentration of the redox couple in the bulk solution. Table 6.1 show the corresponding  $k^0$  values obtained at different stages of modification of the bare ITO electrode using Eqn. 6.3. Notable amongst it is the almost three fold increase in the  $k^0$  value after the electrochemical reduction of the GO/APTES/ITO-glass electrode indicating a faster electron transport at the RGO/APTES/ITO-glass electrode /solution interface. The significant decrease in  $k^0$  values after modification of the RGO/APTES/ITO-glass electrode with ZnS nanoparticles and on further subsequent protein immobilization is due to the sluggish electron transport resulting from the repulsive forces of the negatively charged functional groups and insulating behavior of the protein molecules, respectively at the electrode/solution interface.

According to Davies and Compton, the diffusion layer thickness,  $\delta$ , which helps in categorizing the type of diffusion occurring at the electrodes, can be obtained from the modifying Einstein equation for the root mean square displacement of diffusing particles [21]:

$$\delta = (2D\Delta E/\nu)^{1/2} \quad (6.4)$$

where  $D$  is diffusion coefficient of aqueous ferrocyanide ( $6.3 \times 10^{-6} \text{ cm}^2 \text{ s}^{-1}$ ),  $\Delta E$  is the potential width of the voltammogram and  $\nu$  is the scan rate ( $0.05 \text{ Vs}^{-1}$ ). The corresponding  $\delta$  values for each step of surface modification are given in table 6.1. From the  $\delta$  values (table 6.1), it has been observed these corresponds to the case 3 behavior of the voltammetric responses at spatially heterogeneous electrodes, which is associated

with an overlap of adjacent diffusion layers resulting from the small size of the inert part of the electrode [21].

**Table 6.1:** CV and EIS characteristics parameters at various stages of electrode fabrication

Type of electrodes	$\Delta E_p$ (mV)	$R_{et}$ ( $\Omega\text{cm}^2$ )	CPE		$k^0$ ( $\text{m s}^{-1}$ ) ( $\times 10^{-4}$ )	$Z_w$ ( $\Omega\text{cm}^2$ ) ( $\times 10^{-4}$ )	$\chi^2$ ( $\times 10^{-4}$ )	$\delta$ ( $\mu\text{m}$ )
			$Y_0$ ( $\mu\text{Fcm}^{-2}$ )	$n$				
Bare ITO	180	184.8	3.65	0.956	2.87	8.71	1.20	67.35
APTES/ITO	157	99.8	4.79	0.905	5.32	9.05	1.32	62.89
GO/APTES/ ITO	318	416.3	3.75	0.934	1.27	1.25	1.10	89.51
RGO/APTES/ ITO	182	139	5.24	0.906	3.82	8.61	1.41	67.72
ZnS(MPA)- RGO/APTES /ITO	327	578.5	4.48	0.925	0.91	8.77	1.70	90.77
Ab-cMb/ ZnS(MPA)- RGO/ APTES/ITO	347	699.3	4.20	0.932	0.83	7.06	1.95	93.51

The nature of the redox process occurring at the electrode /electrolyte interface and the surface protein concentration of the Ab-cMb/ZnS(MPA)-RGO/APTES/ITO-glass bioelectrode was determined by taking various CV of the bioelectrode at different scan rates in PBS (pH 7.4, 0.1M KCl) solution containing 2 mM  $[\text{Fe}(\text{CN})_6]^{3-/4-}$  (Fig. 6.8). Inset of the Fig. 6.8 shows the plot of the anodic ( $I_{pa}$ ) and cathodic peak currents

( $I_{pc}$ ) versus square root of the scan rates ( $v^{1/2}$ ). Both the  $I_{pa}$  and  $I_{pc}$  currents are proportional to the  $v^{1/2}$ , suggesting a diffusion controlled process at the electrode surface.

The linear relationship between the redox peak current  $I_{pa}$  and  $v^{1/2}$  which can be expressed by the Eqn. (6.5),

$$I_{pa}(v^{1/2}) = b v^{1/2} + 14.16 \quad (6.5)$$

where slope  $b = 8.04 \pm 0.02$  having a correlation coefficient of 0.996.

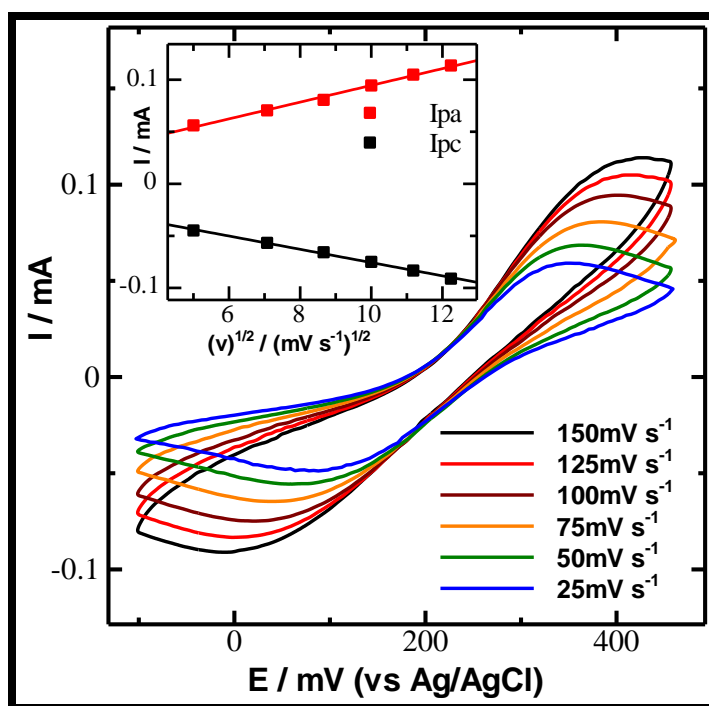


**Fig. 6.8:** CV of bioelectrode as a function of scan rate in PBS (pH 7.4, 0.1M KCl) containing 2mM  $[Fe(CN)_6]^{3-/4-}$ ; Inset: plot of redox peak current vs  $v^{1/2}$ .

#### 6.3.4 Electrochemical impedance response to protein antigen

The Electrochemical impedance response of the fabricated Ab-cMb(BSA)/ZnS(MPA)-RGO/ APTES/ITO-glass bioelectrode for the detection of the target protein antigen, Ag-

cMb, was carried out in PBS (pH 7.4), containing 0.1 M KCl and 2 mM  $[\text{Fe}(\text{CN})_6]^{3-/4-}$  as redox probe, at scanning frequencies from 1 Hz to 100 kHz. The intersheet hopping mechanism of the electrical charge occurring within the stacked layers of the RGO imparts a greater sensitivity in  $R_{\text{et}}$  value in the EIS sensing system [22] wherein the charge transfer mechanism is governed by the antibody-antigen interaction. The EIS response of the bioelectrode corresponding to the addition of different concentration of Ag-cMb is shown in Fig. 6.9, wherein a response for a sample solution containing no target Ag-cMb was considered as control sample response. It was found that after each successive addition of the aliquots of different concentration of target Ag-cMb the  $R_{\text{et}}$  value changes (table 6.2) considerably with a change in the diameter of the semicircle portion in the Nyquist plot (Fig. 6.9a). The increase in  $R_{\text{et}}$  value can be explained on the basis of resulting immunoreaction at the bioelectrode which takes place between antibody-antigen interactions after every successive addition of Ag-cMb. When antigens bind to the surface-immobilized antibodies, the access of the redox couple is hindered to a higher degree than in the absence of antigens. As the Faradaic reaction of a redox couple becomes increasingly hindered, the electron transfer resistance increases and the capacitance decreases, accordingly. It is known that the antigen-antibody complex acts as layer, disturbing ion diffusion and changing electrical capacitance. Both factors significantly affect electrochemical impedance of electrodes during formation of antigen-antibody complex. A more clear description of the electrochemical system's frequency-dependent behavior is provided by using frequency ( $f$ ) dependent Bode impedance ( $Z$ ) and phase ( $\phi$ ) curves, shown in Fig. 6.9b.

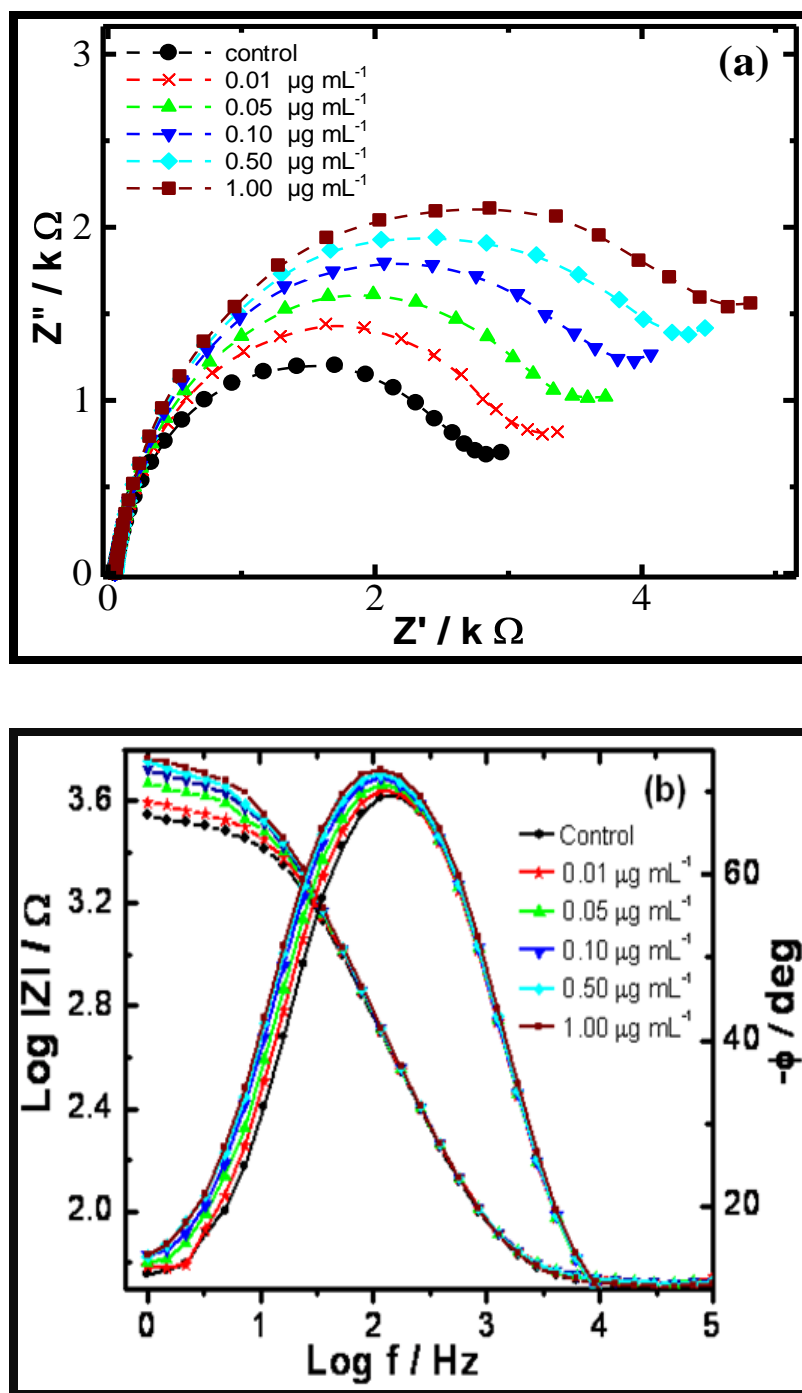


**Fig. 6.9:** (a) Faradaic impedance spectra of the bioelectrode before and after incubation with different concentration of Ag-Mb in PBS (pH 7.4) with 0.1 M KCl solution containing 2 mM  $[\text{Fe}(\text{CN})_6]^{3-/4-}$ , (b) Corresponding bode plots.



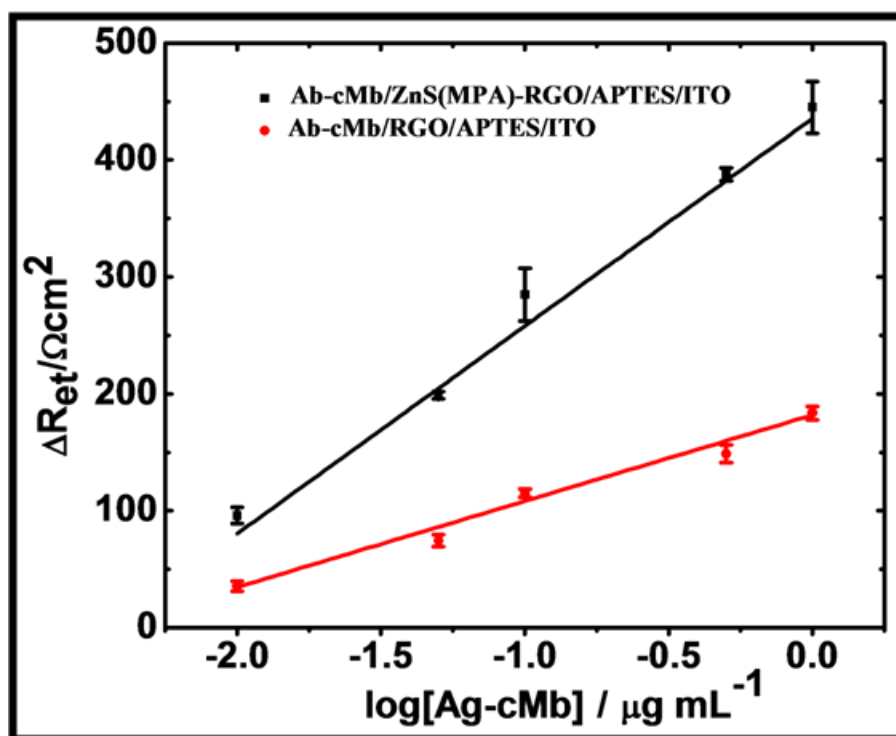
The frequency region from 10 kHz and above where phase angle ( $\phi$ ) is nearly zero is representative of solution resistance ( $R_s$ ). In the intermediate range of frequency from 10 Hz to 10 KHz a straight line with phase angle greater than  $70^\circ$  but less than  $90^\circ$  was obtained, indicating a pseudo capacitive nature of the circuit element. At the lower end of the frequency region ( $<10\text{Hz}$ ), the phase angle was found to approaching zero but was not completely zero due to the presence of both  $R_{et}$  and  $Z_w$ . It is important to note here that insignificant changes observed in the capacitive region of the bode plot on immunoreaction indicated a noncapacitive behavior of the bioelectrode. As can be seen from the plot that the maximum changes in the impedance were observed on immunoreaction at the frequency less than 10 Hz which is the region mainly dominated by  $R_{et}$ , we took  $R_{et}$  as the main sensing element in the impedance measurement of the immunoreaction.

Fig. 6.10 shows a linear relationship between the change in specific electron charge transfer resistance ( $\Delta R_{et} = (R_{et})_{\text{after immunoreaction}} - (R_{et})_{\text{control}}$ ) and logarithmic value of Ag-Mb concentration in the range of 10 ng to  $1 \mu\text{g mL}^{-1}$  and is represented by the Eqn. 6.6:

$$\Delta R_{et}(\log [\text{Ag-Mb}]) = b \log[\text{Ag-Mb}] + 435.5 \quad (6.6)$$

The bioelectrode shows  $R_{et}$  sensitivity (slope  $b$  of the calibration curve) of  $177.56 \Omega \text{ cm}^2$  per decade of Ag-cMb having a correlation coefficient 0.989 ( $n = 5$ ). Though no saturation in the impedance response was observed even beyond  $1 \mu\text{g mL}^{-1}$  of Ag-cMb, the experimental data was concluded only up to this concentration keeping in view the

physiological range of Ag-cMb in human body. This also highlighted the good biocompatibility feature of the constructed bioelectrode.



**Fig. 6.10:** Concentration dependent calibration curve for Ab-cMb/ZnS(MPA)-RGO/APTES/ITO and Ab-cMb(BSA)/RGO/APTES/ITO bioelectrode; error bars represent the standard deviation from three separate experiments.

The selectivity of the bioelectrode towards the Ag-cMb was also tested by carrying out the immunoreaction with non specific protein antigen, Ag-IgG, in a range of 10 ng to 1  $\mu\text{g mL}^{-1}$  under identical conditions. However, no considerable changes in the Ret was observed with the added aliquots of the increasing concentration of IgG with respect to the control sample without IgG, showing almost no antibody-antigen interaction at the electrode surface, thereby indicated the selectivity of the bioelectrode

only towards the specific target Ag-cMb. In order to compare the performance of the ZnS/RGO composite materials over the RGO, a control immunoreaction experiment was carried out with a bare RGO bioelectrode.

**Table 6.2:** EIS characteristics parameters of the bioelectrode on immunoreaction with different concentration of target Ag-cMb

Concentration of Ag-cMb	$R_{et}$ ( $\Omega\text{cm}^2$ )	CPE ( $Y_0$ ) ( $\mu\text{Fcm}^{-2}$ )	n	$k^0$ ( $\text{ms}^{-1}$ ) ( $\times 10^{-4}$ )	$Z_w$ ( $\Omega\text{cm}^2$ ) ( $\times 10^{-4}$ )	$\chi^2$ ( $\times 10^{-4}$ )
Control	699	4.20	0.932	0.75	7.06	1.95
0.01 $\mu\text{g mL}^{-1}$	800	4.10	0.933	0.66	6.58	1.95
0.05 $\mu\text{g mL}^{-1}$	900	4.08	0.931	0.59	5.27	1.94
0.10 $\mu\text{g mL}^{-1}$	1010	4.04	0.934	0.52	4.65	2.21
0.50 $\mu\text{g mL}^{-1}$	1093	4.02	0.933	0.48	4.59	2.32
1.00 $\mu\text{g mL}^{-1}$	1170	3.90	0.936	0.45	4.29	2.49

The results (Fig. 6.10) indicate that the sensitivity of the ZnS(MPA)/RGO modified bioelectrode towards Ag-cMb is about 2.5 fold higher than of the bare RGO bioelectrode ( $73.61 \Omega \text{ cm}^2$  per decade). This sensitivity was found to be higher than that of the recently reported bioelectrodes for Ag-cMb detection [23-25]. This shows that the reduced graphene oxide act as better matrix for the semiconductor/metal nanohybrid based immunosensors than the earlier reported matrices including conducting polymers [26, 27] because of the uniform distribution of colloidal nanoparticles and coherent ionic diffusion. The stability of the bioelectrode was also investigated by repeatedly carrying

out the impedimetric response measurements on the bioelectrode for the same sample of Ag-cMb under identical conditions. With the appearance of no significant changes in the  $R_{et}$  values even after the 10 repeated impedance measurements, it could be concluded that the ZnS-RGO nanocomposite matrix has a good biocompatible property both in the solution and in open as well.

## 6.4 Conclusion

We have demonstrated the fabrication of electrochemically reduced graphene oxide-ZnS nanoparticles (ZnS-RGO) hybrid deposited on to the surface of indium-tin-oxide glass plate for the construction of a bioelectrode. The effectiveness of the ZnS-RGO for the immobilization of protein antibody, Ab-cMb, in native configuration has been delineated with the impedimetric response of the bioelectrode towards the detection of target protein antigen, Ag-cMb in PBS (pH 7.4). The bioelectrode provided a linear range of impedimetric detection of Ag-cMb from  $10 \text{ ng mL}^{-1}$  to  $1 \text{ } \mu\text{g mL}^{-1}$  with a sensitivity of  $177.56 \text{ } \Omega \text{ cm}^2$  per decade. The ZnS-RGO hybrid modified electrode exhibited an enhanced sensitivity of about 2.5 fold higher than that of the bare RGO modified bioelectrode, indicating a strong antibody-antigen interaction at the hybrid surface. The combined synergistic effects of high surface to volume ratio of ZnS(MPA) nanoparticles with high protein loading and conducting RGO lead to the construction of a selective, highly sensitive and biocompatible electrode for Ag-cMb detection. This platform of ZnS-RGO hybrid could be adapted to immobilize other biomolecules for various biosensing applications.

## 6.5 References

1. M.J. Allen, V.C. Tung and R.B. Kaner, *Chem. Rev.* 110 (2010) 132.
2. X.C. Dong, W. Huang and P. Chen, *Nanoscale Res Lett.* 6 (2011) 60
3. Z.Y. Yin, X. Huang, J. Zhang, S.X. Wu, P. Chen, G. Lu, P. Chen, Q.C. Zhang, Q.Y. Yan and H. Zhang, *Nanoscale* 4 (2012) 293.
4. Z. Wang, J. Zhang, P. Chen, X. Zhou, Y. Yang, S. Wu, L. Niu, Y. Han, L. Wang, P. Chen, F. Boey, Q. Zhang, B. Liedberg and H. Zhang, *Biosens Bioelectron* 26 (2011) 3881.
5. B. Li, X. Cao, H.G. Ong, J.W. Cheah, X. Zhou, Z. Yin, H. Li, J. Wang, F. Boey, W. Huang and H. Zhang, *Adv Mater* 22 (2010) 3058.
6. Q. He, S. Wu, S. Gao, X. Cao, Z. Yin, H. Li, P. Chen and H. Zhang, *ACS Nano* 5(2011) 5038.
7. Y. Shao, S. Zhang, C. Wang, Z. Nie, J. Liu, Y. Wang and Y. Lin, *J. Power Sources* 195 (2010) 4600.
8. M. Pumera, A. Ambrosi, A. Bonanni, E.L.K Chng and H.L. Poh, *TRAC-Trend Anal. Chem.* 29 (2010) 954.
9. S. Park and R.S. Ruoff, *Nat. Nanotech.* 4 (2009) 217.
10. M. R. Karim, K. Hatakeyama, T. Matsui, H. Takehira, T. Taniguchi, M. Koinuma, Y. Matsumoto, T. Akutagawa, T. Nakamura, S. Noro, T. Yamada, H. Kitagawa and S. Hayami, *J. Am. Chem. Soc.* 135 (2013) 8097.
11. Z. Wang, S. Wu, J. Zhang, P. Chen, G. Yang, X. Zhou, Q. Zhang, Q. Yan and H. Zhang, *Nanoscale Res. Lett.* 7 (2012) 161.

12. H. Chang, L. Tang, Y. Wang, J. Jiang and J. Li, *Anal. Chem.* 82 (2010) 2341.
13. L. Feng, Y. Chen, J. Ren and X. Qu, *Biomaterials* 32 (2011) 2930.
14. X. Sun, Z. Liu, K. Welsher, J. T. Robinson, A. Goodwin, S. Zaric and H. Dai, *Nano Res.* 1 (2008) 203.
15. J.M. Lee, Y.B. Pyun, J. Yi, J.W. Choung and W.I. Park, *J. Phys. Chem. C* 113 (2009) 19134.
16. W.Zou, J. Zhu, Y. Sun and X. Wang, *Mater. Chem. Phys.* 125 (2011) 617.
17. J. Shia, H. Zhang, A. Snyder, M. Wang, J. Xie, D. M. Porterfield and L. A. Stanciu, *Biosens. Bioelectron.* 38 (2012) 314.
18. K. Wang, Q. Liu, Q. Guan, J. Wu, H. Li and J. Yan, *Biosens. Bioelectron.* 26 (2011) 2252.
19. J. Du, X. Yu and J. Di, *Biosens. Bioelectron.* 37 (2012) 88.
20. Rajesh, B. K. Das, S. Srinives and A. Mulchandani, *Appl. Phys. Lett.* 98 (2011) 013701.
21. S.A. Mamuru and K. I. Ozoemena, *Electroanalysis*, 22 (2010) 985.
22. K. S. Kim, Y. M. Um, J. Jang, W. Choe and P. J. Yoo, *ACS Appl. Mater. Interfaces* 5 (2013) 3591.
23. N. Puri, S. K. Mishra, A. Niazi, A. M. Biradar and Rajesh, *Synth. Met.* 169 (2013) 18.
24. F. Darain, P. Yager, K.L. Gan and S.C. Tjin, *Biosens. Bioelectron.* 24 (2009) 1744.
25. T.M. O'Regan, L. J. O'Riordan, M. Pravda, C.K. O'Sullivan and G. G. Guilbault, *Anal. Chim. Acta*, 460 (2002) 141.

26. E. G. Matveeva, Z. Gryczynski and J. R. Lakowicz, *J. Immunol. Methods* 302 (2005) 26.
27. S.K. Mishra, R. Pasricha, A.M. Biradar and Rajesh, *Appl.Phys. Lett.* 100 (2012) 053701.

## CHAPTER 7

---

### CONCLUSIONS AND FUTURE PERSPECTIVE

---

---

The research work presented in this thesis has described the synthesis and characterization of functionalized semiconducting and metal nanoparticles and their organic/inorganic nanocomposites, as biocompatible materials, for biosensing applications. The thesis described the comprehensive and comparative electrochemical studies on biocompatible zinc sulfide and platinum nanoparticles both individually as well as in the nanocomposite forms with organic conducting polymer and inorganic graphene, for biosensing applications. More particularly, it described the electrochemical activity and electrochemical impedance performance of the ZnS /Pt NP and their nanocomposite based bioelectrode towards the quantitative detection of cardiac biomarkers e.g.  $\alpha$ CRP and cMb, as impedimetric immunosensor.

The thesis work started with the preparation of mercaptopropionic acid capped ZnS nanoparticles (ZnS(MPA)-NPs) and its nanocomposite with a conducting polymer, polypyrrole (PPy), with a controlled film thickness, over an ITO-glass electrode, using a simple and direct one step electrochemical polymerization method. The electrochemical deposition method provided a homogeneous distribution of ultrafine ZnS(MPA)-NPs within the uniform and adherent PPy film with high degree of geometrical conformity and controllable film thickness. The free pendant carboxyl groups of the MPA capped ZnS(MPA)-NPs intercalated within the polymer film were utilized for the site specific immobilization of protein antibody, Ab- $\alpha$ CRP, using carbodiimide coupling reaction, for



the construction of a bioelectrode. The rationale behind using ZnS(MPA)NPs-PPy nanocomposite film was that the long chain of PPy in the polymer composite acts as a spacer between the biomolecules and the transducer, wherein the site-specific immobilization by the biocompatible ZnS(MPA)-NPs helps in preserving the native protein conformation and reducing the steric hindrance for better probe orientation and accessibility of the biomolecules to the analyte. The effect of the film thickness on  $R_{et}$  sensitivity of the bioelectrode towards the quantitative detection of protein antigen, Ag- $\alpha$ CRP, was analyzed by comparing the impedance sensing spectra of two different charge densities ( $250 \text{ mC cm}^{-2}$  and  $1000 \text{ mC cm}^{-2}$ ) injected nanocomposite film based bioelectrode. It was concluded that the ZnS(MPA)NPs-PPy nanocomposite film prepared at injected charge density of  $250 \text{ mC cm}^{-2}$  provided a sensitivity of  $28.47 \Omega \text{ cm}^2$  per decade of [Ag- $\alpha$ CRP] which is double the sensitivity of  $13.47 \Omega \text{ cm}^2$  per decade obtained with the film prepared at injected charge density of  $1000 \text{ mC cm}^{-2}$ .

Though, the protocol discussed in chapter 2 for the fabrication of a bioelectrode based on ZnS(MPA)NPs-PPy nanocomposite film is good in terms of its ease of preparation with cost effective and biocompatible features but the sensitivity of the bioelectrode so obtained was quite low. To further understand the structural, electrochemical activity and impedance behavior of the polymer composite based bioelectrode, PPy nanocomposite film was prepared with carboxyl functionalized Pt metal nanoparticles (Pt(MPA) NP). Due to high electroactive characteristic of Pt NP, their nanocomposite with  $\pi$ -conjugated PPy exhibited high analytical sensitivity, wherein they functioned as conductive pathway for electron transfer, improving the

electrochemical reaction at the electrode surface. The site-specific and efficient biomolecular immobilization of the electroactive Pt-NPs together with the conducting polymer matrix helped in enhancing the impedance response sensitivity of the bioelectrode towards the detection of target protein antigen, Ag- $\alpha$ CRP. The  $R_{et}$  sensitivity of Pt(MPA)NPs-PPy based bioelectrode was found to be ~4 times higher than the ZnS(MPA)NPs-PPy based bioelectrode .

Furthermore, to overcome the limitation of aggregation encountered in the case of polymer nanocomposite film and to further increase the surface coverage of the electrode by the nanoparticles, SAM of APTES was chosen as a basal matrix, which provided a highly ordered unimolecular matrix, for the uniform covalent attachment of nanostructured materials over its surface. Chapter 4, described comprehensive structural and electrochemical studies on ZnS(MPA) nanoparticles on APTES modified ITO-glass electrode, wherein ZnS(MPA) nanoparticles were covalently attached to the SAM of APTES. This ZnS(MPA) nanoparticles-silane modified ITO-glass electrode has been used, as a bioanalytical platform, for immunosensor application. The ZnS(MPA) NP showed good biocompatibility and acts as an effective bioconjugate to provide a sufficient amount of binding sites for the immobilization of cardiac protein myoglobin, Ab-cMb at the electrode surface for immunoreaction. A detailed study on the electrochemical impedance spectroscopy (EIS) behavior of the ZnS(MPA) nanoparticles-silane/ITO-glass electrode and its immunosensing application with the optimal fitted equivalent circuit model has been depicted in chapter 4.

Next, in chapter 5, we analyze the effects of using a more electroactive matrix of Pt(MPA) nanoparticles-silane on the biosensing performance of the corresponding bioelectrode towards the detection of prognostic cardiac marker, cMb. The highly electroactive functionalized Pt(MPA)-silane surface with a large number of free -COOH linkage groups remarkably improved the properties of the bioelectrode in terms of stability and sensitivity. Both the microstructural and electrochemical characteristics of the biofunctionalized Pt(MPA)-silane/ITO-glass electrode was studied by Atomic force microscopy (AFM), transmission electron microscopy (TEM), X-ray diffraction (XRD), Energy-dispersive X-ray spectroscopy (EDX), and EIS techniques. The Pt(MPA)-silane /ITO-glass bioelectrode showed significant changes in  $R_{et}$  on immunoreaction with cardiac antigen Ag-cMb and exhibited a sensitivity of  $184.8 \Omega \text{ cm}^2$  per decade of Ag-cMb concentration which is higher than that of a  $R_{et}$  sensitivity obtained with a ZnS(MPA) nanoparticles-silane matrix (i.e.  $117.36 \Omega \text{ cm}^2$  per decade of Ag-cMb concentration).

Chapter 6 highlighted a facile strategy to fabricate a bioelectrode based on ZnS(MPA) nanoparticles decorated reduced graphene oxide (RGO) hybrid over a silane modified ITO-glass electrode. The ZnS(MPA)-RGO hybrid demonstrated unique physicochemical properties, which include high surface area, strong mechanical strength, biocompatibility, ease of fabrication and enhanced electrochemical properties. The composition, morphology and the microstructure of the ZnS(MPA)-RGO hybrid were characterized using various instrumental techniques such as SEM, HRTEM, EDX and electrochemical techniques. The HRTEM characterization of ZnS-RGO hybrid showed

the uniform distribution of ultra-fine nanoparticles of ZnS in nano-sheets of RGO throughout the hybrid material. The effectiveness of the ZnS-RGO hybrid for the immobilization of protein antibody, Ab-cMb, in native configuration has been delineated with the impedimetric response of the bioelectrode towards the detection of target protein antigen, Ag-cMb. The combined synergistic effects of high surface to volume ratio of ZnS(MPA) nanoparticles and conducting RGO support with high accessible surface area lead to the construction of a selective, highly sensitive and biocompatible electrode for Ag-cMb detection. The ZnS-RGO hybrid modified electrode exhibited an enhanced sensitivity of about 2.5 fold higher than that of the bare RGO modified bioelectrode, indicating a strong antibody-antigen interaction at the hybrid surface. It was concluded that the reduced graphene oxide acts as a better matrix, for the semiconductor/metal nano-hybrid based immunosensors than the above described matrices including conducting polymer PPy because of uniform distribution of the nanoparticles and coherent ionic diffusion.

In conclusion, the thesis depicted the synthesis and characterization of the functionalized Zn and Pt NP and their organic/inorganic nanocomposites with their electrochemical utility in the quantitative detection of the cardiac markers. In addition, the academic aims of this research, set out in the beginning of this research work have been addressed. The results presented in the thesis suggest that these nanoparticles based nanocomposites and nanohybrids can have a wide spread applicability in the field of biomedical diagnosis.

## **Future perspective**

The present thesis is an attempt to utilize the characteristic properties of various nanomaterials in order to improve the dynamic detection range, sensitivity and specificity of the bioelectrode. However, it opens up new directions for further research, some of which are listed below:

- Though cardiac biomarkers have been successfully used for the detection of AMI, there still is considerable ambiguity surrounding the use of cardiac biomarkers, as no single biomarker fulfils all the criteria of an ‘ideal’ cardiac biomarker. Therefore, multiple marker detection strategy needs to be adapted using a combination of established and new cardiac markers, which can help in making correct clinical decisions.
- The concept of using various nanomaterials and their nanocomposites can be used for the development of highly sensitive devices for early diagnosis and point-of-care applications.
- Future innovation in the biosensor technology can be directed towards increasing the sensitivity and reduction in sample size to nano levels by the miniaturization of electronic transducers for portability and patterning arrays and use of microfluidics for multiple cardiac biomarker detection.

## **List of Publications**

1. “Microstructural and electrochemical impedance characterization of bio-functionalized ultrafine ZnS nanocrystals-reduced graphene oxide hybrid for immunosensor-applications.”  
**Sujeet K Mishra**, Avanish K Srivastava, Devendra Kumar, Ashok M Biradar and Rajesh .  
*Nanoscale (RSC)* 5(2013) 10494.
2. “Electrochemical impedance spectroscopy characterization of mercaptopropionic acid capped ZnS nanocrystal based bioelectrode for the detection of the cardiac biomarker—myoglobin.”  
**Sujeet K Mishra**, Devendra Kumar, Ashok M Biradar and Rajesh.  
*Bioelectrochemistry (Elsevier Press)* 88 (2012) 118.
3. “ZnS-nanocrystals/polypyrrole nanocomposite film based immunosensor”  
**Sujeet K Mishra**, Renu Pasricha, Ashok M Biradar and Rajesh.  
*Applied Physics Letters* 100 (2012) 053701.
4. “Bio-functionalized Pt nanoparticles based electrochemical impedance immunosensor for human cardiac myoglobin.”  
**Sujeet K Mishra**, Avanish K Srivastava, Devendra Kumar and Rajesh.  
*RSC Advances* 4 (2014) 21267.
5. “Protein functionalized Pt nanoparticles-conducting polymer nanocomposite film: Characterization and immunosensor application”  
**Sujeet K Mishra**, Avanish K Srivastava, Devendra Kumar, Ashok Mulchandani and Rajesh.  
*Polymer* (2014) Accepted. <http://dx.doi.org/10.1016/j.polymer.2014.05>.

### **Publications not included in this thesis**

1. “Biofunctionalized Gold Nanoparticle-Conducting Polymer Nanocomposite Based bioelectrode for CRP detection”  
**Sujeet K Mishra**, Vikash Sharma, Devendra Kumar and Rajesh  
*Appl Biochem Biotechnol* (2014) DOI: 10.1007/s12010-014-0984-1.
2. “Microstructural and Potential Dependence Studies of Urease-Immobilized Gold Nanoparticle–Polypyrrole Composite Film for Urea Detection”  
Nidhi Puri, **Sujeet K Mishra**, Mariam J Laskar, Avanish K Srivastava and Rajesh  
*Appl Biochem Biotechnol* 172(2014) 1055-69.
3. “Structural and impedance spectroscopic studies on biofunctionalized poly (pyrrole-co-pyrrolepropylyc acid) film”  
Nidhi Puri, **Sujeet K Mishra**, Asad Niazi, Ashok M Biradar and Rajesh  
*Synthetic Metals* 169 (2013) 18– 24.
4. “Synthesis and electrochemical characterization of myoglobin-antibody protein immobilized self-assembled gold nanoparticles on ITO-glass plate”  
Rajesh, Vikash Sharma, **Sujeet K Mishra** and Ashok M Biradar  
*Materials Chemistry and Physics (Elsevier Press)*, 132 (2012) 22– 28.
5. “Electrochemical impedance immunosensor for the detection of cardiac biomarker Myoglobin (Mb) in aqueous solution”  
Rajesh, Vikash Sharma, VK Tanwar, **SK Mishra** and AM Biradar  
*Thin Solid Films (Elsevier Press)*, 519 (2010) 1167–1170.
6. “An amperometric uric acid biosensor based on gold nanoparticles modified 3-amino propyl triethoxysilane/indium tin-oxide electrode”  
T Ahuja, VK Tanwar, **SK Mishra**, D Kumar, AM Biradar and Rajesh  
*Journal of Nanoscience and Nanotechnology* 11 (2011)1–10.

**Papers presented in National/International conferences:**

1. Presented a poster titled “Mercaptopropionic acid capped ultrafine Pt nanoparticles/polypyrrole nanocomposite film based immunosensor” in **International Conference on Advanced Functional Materials (ICAFM-2014)**, organised by CSIR-NIIST, 19-21 February 2014 at Thiruvananthapuram.
2. Presented a poster titled “Microstructural/electrochemical characterization and application of carboxyl functionalized gold nanoparticles-conducting polymer nanocomposite based bioelectrode” in **India-Japan Workshop on Biomolecular Electronics and Organic Nanotechnology For Environment Preservation (IJWBME 2013)**, December 13-15, DTU, Delhi, India
3. Oral presentation on ‘Conducting gold nanoparticles-polypyrrole nanocomposite film based potentiometric urea’ in **International Conference on Emerging Technologies-Micro to Nano (ETMN-2013)**. Organized jointly by:BITS, Pilani, INDIA and CSIR-CEERI, Pilani, INDIA 23-24 February 2013. Published in “**Proceedings of International Conference on Emerging Technologies - Micro to Nano 2013 Goa, India**”. Page 95-96
4. Presented a poster titled ” Fabrication of Immunosensor Based on ZnS-reduced graphene Nanocomposite” in NPL, on the occasion of **National Science Day**, 28<sup>th</sup> Feb 2013.
5. Presented a poster titled “Carboxyl functionalized gold nano particles doped polypyrrole film based immunosensor for the detection of C-reactive protein” in **Healthcare India 2012** organized by APA international congress on advances in human healthcare systems 20-23 Feb 2012, New Delhi, India.
6. Presented a poster titled “Self Assembled Monolayer Modified Au Electrode for the Detection of Cardiac Biomarker Myoglobin (Mb)” in **Indo-Japan Workshop on Biomolecular Electronics & Organic Nanotechnology for Environment Preservation**, 17-20 Dec 2009, NPL, Delhi, India.



## Curriculum Vitae

### Personal Information

Name : Sujeet Kumar Mishra  
Address : S-221/118 A first floor,  
khyala, Vishnu Garden, New Delhi-  
18  
Contact No. : +91-9540775358  
E-mail : [sujeetmishra5@yahoo.com](mailto:sujeetmishra5@yahoo.com)  
Father's Name : Sri Ashok Kumar Mishra  
Mother's Name : Smt. Sindhu Mishra  
Date of Birth : March 5, 1985  
Nationality : Indian  
Language Known : Hindi, English  
Sex / Marital Status : Male / Unmarried

### Educational Qualifications:

Degree	Board/University	Year	Percentage	Division
Ph. D. (Chemistry)	Delhi Technological University, New Delhi and CSIR-National Physical Laboratory	August 2009	Thesis submitted 2014	-
M.Sc. (Chemistry)	Delhi University	2009	64%	1 <sup>st</sup>
B. Sc.	Delhi University	2007	84.96%	1 <sup>st</sup>
Higher Secondary	CBSE	2002	75.66%	1 <sup>st</sup>
High School	CBSE	2000	83.66%	1 <sup>st</sup>

### Professional Career:

- Qualified CSIR NET-JRF in 2009.
- Junior Research Fellow, CSIR-NPL (August 2009-August 2011)
- Senior Research Fellow, CSIR-NPL (August 2011-in progress)

### Research Interest:

Sensors/Biosensors; synthesis and characterization of various nanomaterials and nanocomposites; electrochemical applications of these nanomaterials in detection and quantification of various novel biomarkers.

### Research Publications:

Published - 12, Papers presented in conferences – 6